BEHAVIOR OF ALLOY 617 AT 650°C IN LOW OXYGEN PRESSURE ENVIRONMENTS

by

FANNY MAS

Submitted to the Department of Materials Science and Engineering
in Partial Fulfillment of the Requirements for the Degree of

Master of Science in Materials Science and Engineering

at the

Massachusetts Institute of Technology

September 2010

Signature of Author FA

Department of Materials Science and Engineering
July 29, 2010

Certified by

Ronald G. Ballinger
Professor of Nuclear Engineering and Materials Science and Engineering
Thesis Supervisor

Accepted by

Christine Ortiz
Chair, Departmental Committee on Graduate Students

BEHAVIOR OF ALLOY 617 AT 650°C IN LOW OXYGEN PRESSURE ENVIRONMENTS

by

FANNY MAS

Submitted to the Department of Materials Science and Engineering
On July 29th, 2010 in Partial Fulfillment of the
Requirements for the Degree of Master of Science
In Materials Science and Engineering

ABSTRACT

The behavior of alloy 617 at 650°C in low oxygen partial pressure environments has been studied under static loading. Of particular interest was the crack growth rate in these conditions. For that, tests were conducted at a constant stress intensity factor of 49.45 MPa$\sqrt{m}$ (45 ksi$\sqrt{inch}$) using a direct current potential drop measurement system to determine crack length. High purity argon gas allowed establishing an oxygen partial pressure as low as 10^{-22} atm and premixed oxygen/argon gases were used to vary the oxygen potential. To go deeper into the understanding of the phenomena involved, a creep test (constant load of 1.21×10^4 N in argon environment) and a corrosion experiment (50 ppm oxygen in argon for 500 hours without any load) were also added.

The crack growth tests led to a particularly unexpected result: whatever the oxygen potential, the crack growth rate increased with time and the plot for the crack length versus time displayed a recurrent parabolic shape without any change in the environment. No unique crack growth rate could be defined in a given environment and the influence of the environment on the crack growth rate was not clearly visible. Multiple features were found to surround the main crack: secondary cracks parallel to the principal one, intergranular cracking ahead of the crack tip, wedge cracks at grain boundaries and aggregates of Cr-rich carbides near the lips of the crack. Moreover no extensive oxide scale was formed on the surface of the sample exposed to the corrosive environment (50 ppm oxygen in argon) for 500 hours. The non-constant crack growth rates, together with the observed cracking features, were attributed to the competition between creep deformation and mechanical fracture, likely environmentally enhanced. An exponential law was found to fit the data for the crack growth rate as a function of time for a K of 49.45 MPa$\sqrt{m}$ (45 ksi$\sqrt{inch}$). The effects of the environment were overcome by mechanical and thermal processes leading to damage accumulation and so, a reaction of alloy 617 to the external stress and temperature highly dependent on time. This behavior was compared with the one of alloys Haynes 230 and Incoloy 908 in the same conditions.

TABLE OF CONTENTS

LIST OF FIGURES

LIST OF TABLES

ACKNOWLEDGEMENTS

I would like to thank all of those who were supportive and provided encouragement through my time at MIT, especially my dear friends and family.

1. INTRODUCTION

The increase in the world's energy demand requires the development of new energy sources. Nowadays nuclear energy represents 16% of the world's energy supply and this proportion will certainly tend to grow in the future. In the constant battle to increase efficiency, safety margins and lower cost, a new breed of nuclear reactors, Generation IV, is being developed. This ensemble of nuclear reactor technologies that could be built by 2030, have the promise of significant improvements in economics, safety, reliability and sustainability over the currently operating reactor technologies. In 2002, six different concepts were selected by a group of countries who joined together to form the Generation IV International Forum. Among these designs is the Very-High-Temperature Reactor (VHTR), a graphite-moderated, helium-cooled reactor with a once-through uranium fuel cycle. The goal of this gas-cooled reactor is to produce helium at temperatures as high as 950°C and pressures up to 7 MPa for a design life of 60 years. In some configurations approximately 90% of the VHTR heat will be used to generate electricity and 10% to produce hydrogen. Helium circulation allows removing the heat generated in the reactor core to the power conversion unit or the hydrogen-production plant. The Intermediate Heat Exchanger (IHX) is the component in which the heat from the primary circuit helium is transferred to the secondary, thus keeping the secondary circuit free of radioactive contamination. A schematic of the reactor is provided in Figure 1 and enables to localize the IHX.

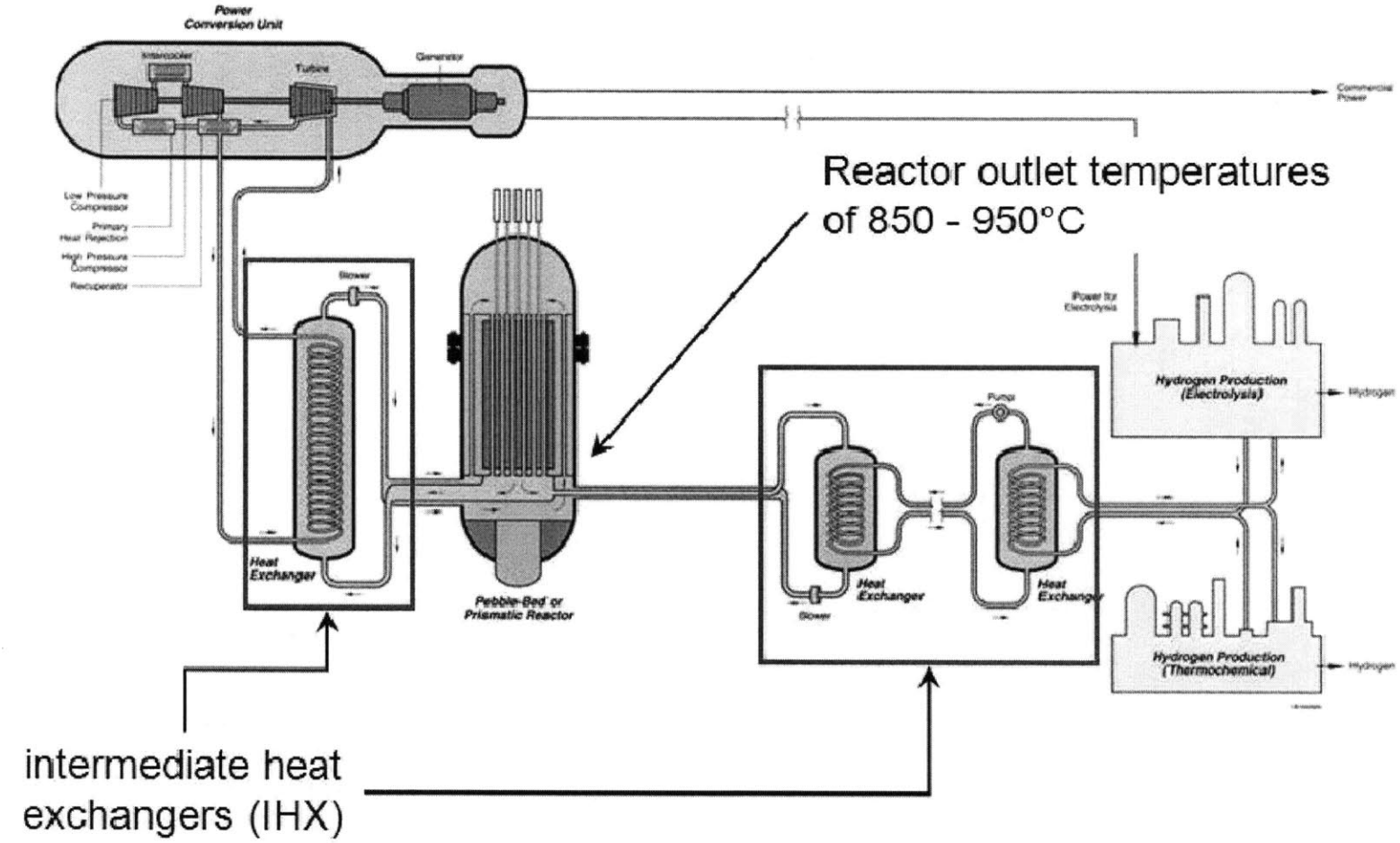

Figure 1. Schematic showing the organization of the VHTR including a power generation unit and a hydrogen production plant

Nickel base superalloys, especially the precipitation hardening superalloys, have been widely used in many high-temperature applications because of high-temperature strength, oxidation resistance, creep resistance, and phase stability. However they are not suitable for the case of VHTR because the operating temperatures are so high that the precipitates responsible for the high strength of the material are no longer stable. On the other hand, the solid solution hardening superalloys that rely on lattice distortion due to alloying elements or MC type carbide precipitation for their strength can maintain considerable strength at higher temperature and so are considered as suitable for the VHTR applications. Among these superalloys, Inconel 617 and Haynes 230 are the two main candidates for the IHX. Both have attractive properties for high temperature applications. Alloy 617 is often considered for use in aircraft and land-based gas turbines, chemical manufacturing components, metallurgical processing facilities and power generation structures. Compared with 617, alloy 230 is considered relatively new and serves similar applications as a competitor material of alloy 617. For both of them, the high nickel and chromium contents provide high resistance to a variety of reducing and oxidizing environments. The aluminum, in conjunction with chromium, offers oxidation resistance at high temperatures. These materials have to exhibit good resistance towards corrosion as it is expected that the VHTR's cooling gas be polluted by air ingresses during abnormal/accident conditions, internal leakages or the degassing of adsorbed species out of the large amount of graphite used. Typical impurities are H_2, H_2O, CH_4, CO, N_2 and CO_2 in the microbar range, which can react with the metallic components. Depending on their relative concentrations and on the helium temperature, the interaction of these impurities with metallic materials may or may not lead to internal and surface oxidation and may cause alloy carburization or decarburization. However, it should be noted that both alloy 617 and 230 were developed for oxidizing conditions. At very low oxygen partial pressures it may be possible to destabilize the protective oxide film and promote internal oxidation. Under these conditions the environment may significantly affect crack growth. Additionally, under carburizing conditions alloy 230, containing large amounts of carbide forming elements (W for example) may selectively form carbides which may also degrade properties.

For a material to be qualified, a significant amount of data must be acquired; various mechanical behavior models must be developed; strengthening mechanisms must be well understood; metallurgical evolution and stability must be accurately predicted and most importantly, the material must be approved by American Society of Mechanical Engineers

Boiler and Pressure Vessel Code (ASME B&PV Code) for nuclear applications at elevated temperatures. A draft code case for alloy 617 was submitted in the late 1980s, but it was concluded that there was insufficient information on creep-fatigue behavior and high temperature weldment fatigue to allow code qualification. Additionally, since the IHX must operate over a wide temperature range (500-950°C) it is possible that environmental effects may be present at lower temperatures, below the creep range. This present work concentrates on alloy 617 as it appears closest to gaining code approval and alloy 230 will only be used for the needs of comparison. The work focuses on the 650°C temperature range. This temperature is located in the "grey" area for these materials where both creep and time-independent processes can contribute to the overall behavior.

The initial goal of this project was to pursue the work done by Julian Benz for his Master's thesis about the effects of oxygen potential on high temperature crack growth in alloy 617 [21]. His study was essentially concentrated on crack propagation under fatigue conditions at different frequencies, R-ratios and levels of stress intensity factor range ΔK as a function of oxygen partial pressure. Static loading was also investigated which showed a decrease in the crack growth rate when the oxygen partial pressure was increased (from 2 x 10^{-7} to 10^{-3} atm) at an applied K of 49.45 MPa$\sqrt{m}$ (45 ksi$\sqrt{}$inch). As neither a definitive conclusion nor a complete understanding of the processes involved could be reached, further experiments were needed to explore this unexpected tendency. Some of the uncertainty in the previous results may have been due to the high value of K employed. In some cases, the previous results may have been influenced by deviations from ASTM requirements regarding plastic zone size. This work aims at further investigating the synergistic effects of sustained load, environment and temperature in the case of alloy 617. The environment of interest is characterized by a low oxygen partial pressure whereas both alloy 617 and 230 were initially designed to operate in a highly oxidizing environment where the formation of protective chromium (or aluminum) oxide based films predominate. At very low potentials, where the protective film may not be stable, these materials are not optimized and may be susceptible to embrittlement by oxygen transport along grain boundaries and/or to the effects of decarburization. For VHTR, the development effort has been largely focused on investigating the behavior of alloy 617 at the maximum expected operating temperature where creep is expected to dominate. However the full operating temperature range covers 450 to 950°C. At the lower end of this range, cracks may initiate and propagate if substantial stresses are maintained at the crack tip. For this study a temperature of 650°C has been chosen as it

corresponds to an intermediate and crucial domain where creep and mechanical (time independent) crack growth may interact and produce unexpected effects.

The objectives of this study are stated as follow:

- Measure the crack growth rate in alloy 617 at 650°C in low oxygen potential environments under stress intensity factors expected to exist in the NGNP heat exchanger systems (K = 49.45 or 38.5 MPa$\sqrt{m}$). The higher K was chosen to overlap with previous conditions studied by Benz and the lower K was chosen as a mean of comparison to investigate the effects of the stress intensity factor level.

- Identify the effects of environment, especially the oxygen partial pressure, on the crack propagation rate and the crack morphology (crack path, mode of failure, cracking features).

- Compare the behavior of alloy 617 to the one of alloys 230 and 908 in the same conditions and identify the processes responsible for the differences. Alloy 908 is known to be highly susceptible to oxygen embrittlement at 650°C and intermediate oxygen partial pressures (>0.1 ppm).

- Investigate the corrosion behavior of the above alloys at 650°C and relate it to the crack growth characteristics in the different environments.

- Determine the mechanisms (environmental influence, creep deformation, brittle fracture) operating in the conditions of interest and responsible for the crack propagation in alloy 617.

2. BACKGROUND

The following literature review is focused on various aspects of nickel-base superalloys' behavior relevant for high temperature applications. Oxidation, crack growth and creep transformations will be investigated in order to help understand the mechanisms potentially involved in alloy 617 under static loading at 650°C and low oxygen partial pressures. As the effects of many different factors are entangled in the final observed behavior, it is important to study them first separately to underline the role played by each of them.

2.1 High temperature oxidation of Ni-base superalloys

This first part will be dedicated to the oxidation behavior of Ni-base superalloys, especially 617 and 230 in the absence of any load, the main parameters being the oxygen partial pressure and the temperature.

2.1.1 Solid-solution strengthened nickel-chromium base alloys

Most nickel superalloys are based upon the nickel-chromium system with the chromium content being the major factor governing oxide formation and oxidation rate. A detailed investigation of the oxidation behavior of simple Ni-Cr alloys has been performed by Giggins and Pettit [1] and the chromium content necessary to grow a sufficiently protective Cr_2O_3 scale on nickel-base superalloys lies between 20 and 30%. However it is usually chosen around 20% in order to prevent the formation of topologically close-packed (TPC) phases that occur at high chromium levels and cause brittleness and reduction in strength and ductility. The advantages of Cr_2O_3 as a protective oxide layer are the rapid initial growth, the ability to develop a tight protective oxide layer, the spallation resistance in cyclic oxidation and the capability of regrowth of the protective oxide in the event of scale rupture [2]. However at temperatures above 1000°C, Cr_2O_3 is known to transform into the volatile species CrO_3 and the rupture of the protective scale leads to rapid oxidation of the metal matrix depleted in chromium.

Even though chromium plays the major role in oxidation resistance, the other solid-solution hardening and carbide forming elements cannot be completely neglected. Although they are mostly added to provide strength, they can also influence the oxidation processes. For

example, the beneficial effect of aluminum to improve corrosion resistance in nickel chromium alloys has been demonstrated [3]. In Figure 2, at a given temperature, as the aluminum content is increased, the oxidation rate is shown to decrease and then reach a minimum value. This is due to the formation of volatilization resistant Al_2O_3. But high aluminum content can also have detrimental effect, as it is the case of alloy 693 (wt% Al = 3.36) in air at 1000°C [4]. The growth of aluminum oxide along grain boundaries is found to block the diffusion of chromium from the bulk to the surface and hinder the build-up of a sufficiently protective Cr_2O_3 layer. This leads to the diffusion of nitrogen into the bulk and the formation of aluminum nitride and so no protective Al_2O_3 layer can grow.

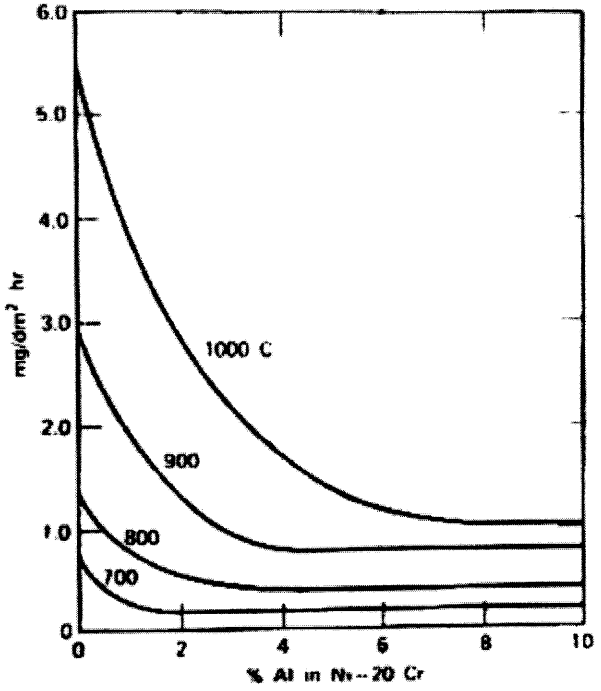

Figure 2. Effect of aluminum content on the air oxidation rate of Ni-20Cr alloys [3]

2.1.2 Precipitate strengthened nickel-chromium base alloys

When added in certain proportions, aluminum and titanium precipitate high volume fractions of the FCC ordered intermetallic $Ni_3(Al,Ti)$ phase named γ'. This coherently precipitated phase greatly increases strength and improves high-temperature oxidation resistance [3]. In several superalloys, niobium is also present and the body-centered tetragonal Ni_3Nb precipitate named γ''can develop [3]. The final protective oxide scale that forms is a

consequence of several complex and sometimes competitive reactions which are a function of alloy chemistry, environment composition, time and temperature of exposure.

Despite this complexity, it is the chromium-aluminum ratio that plays a critical role and the oxidation processes can be seen as the oxidation of a simple Ni-Cr-Al alloy. During a transient period before steady state, a thin surface film consisting of the spinel $Ni(Cr,Al)_2O_4$ and NiO is first formed. Oxygen diffusion into the bulk leads to the precipitation of Cr_2O_3 and Al_2O_3 particles. Then, depending on the composition, three mechanisms have been proposed by Giggins and Pettit [5]. In Group I alloys, the fraction of aluminum and chromium precipitated is too low to get a dense film and so we observe internal oxidation of Al and Cr and growth of a dense NiO layer above the spinel. In both groups II and III, a high fraction of Al_2O_3 and Cr_2O_3 are precipitated and a continuous layer can grow below the surface. In Group II, the Al content is so low that Al suffers internal oxidation and the film consists of Cr_2O_3. In Group III, the Al content is sufficiently high to develop a dense Al_2O_3 scale near the surface. Figure 3 gives a schematic of these three possibilities and the oxidation map of Ni-Cr-Al at 1000°C. According to their Cr and Al content and neglecting all other major elements (Co and Mo in 617; W in 230), Inconel 617 and Haynes 230 can be classified as Group II alloys in this oxidation map.

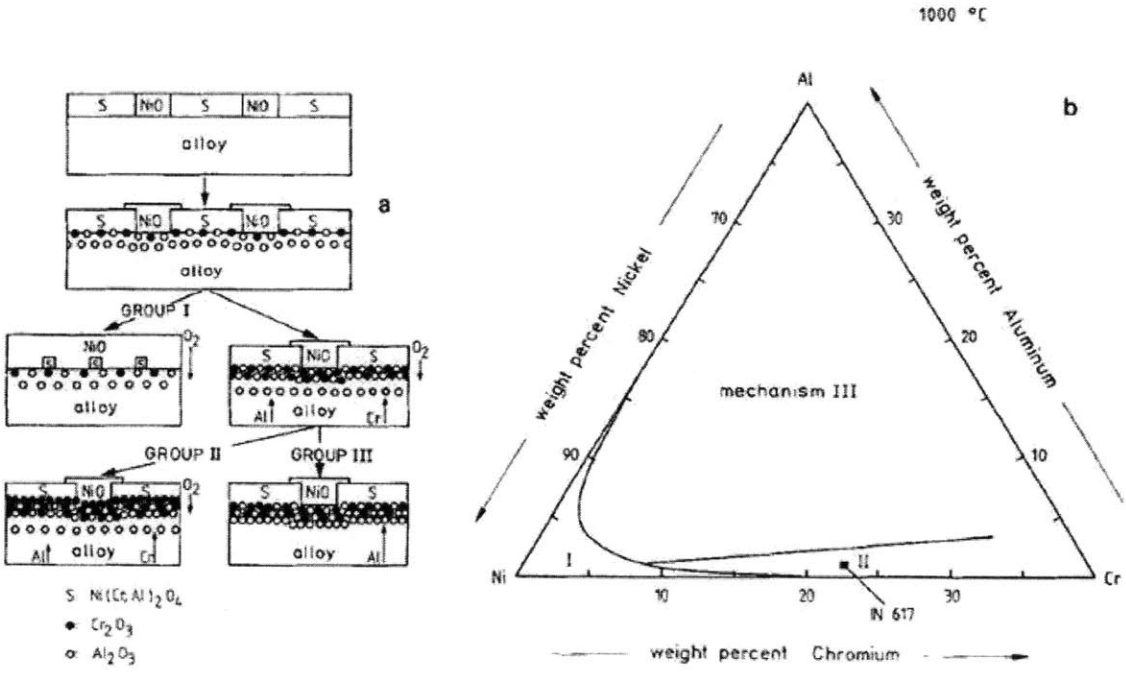

Figure 3. The oxidation of Ni-Cr-Al alloys after Gigging and Pettit [5]. (a) The three different mechanisms. (b) The oxidation map at 1000°C.

2.1.3 Oxidation experiments on Inconel 617

Since alloy 617 is normally used for very high temperatures applications, most of the studies have been conducted in the range of 900 to 1100°C in both air and helium environments [6,7]. As predicted by the previous model, the steady state corresponds to the formation of a homogeneous layer of Cr_2O_3 with internal oxidation of Al_2O_3 in the form of elongated and deep particles growing preferentially at the grain boundaries. The two most important additional components, Mo and Co, show no effect at all on the steady state oxidation. Contrary to alloy 713LC (Al = 5.8 wt%; Cr = 11.8 wt%), the weight gain and structure of the oxide layer in alloy 617 are found to be identical in air and low oxygen partial pressure environment (10^{-16} to 10^{-19} bars) at 900°C despite the huge difference in oxygen content [6, 7]. However, as the temperature or time of exposure is increased the surface oxide becomes unstable and non-continuous in both environments. As a consequence of the spallation and evaporation of surface oxides, Ni and Co from the matrix are exposed and oxidized in air.

All these phenomena (growth of the surface layer, internal oxidation) are enhanced when a load is applied because of enhanced diffusion of oxygen along the grain boundaries [7]. Figure 4 shows the volatilization of CrO_3 from Cr_2O_3 layer which leads to a rugged oxide/metal substrate after long-term oxidation at 1100°C [8].

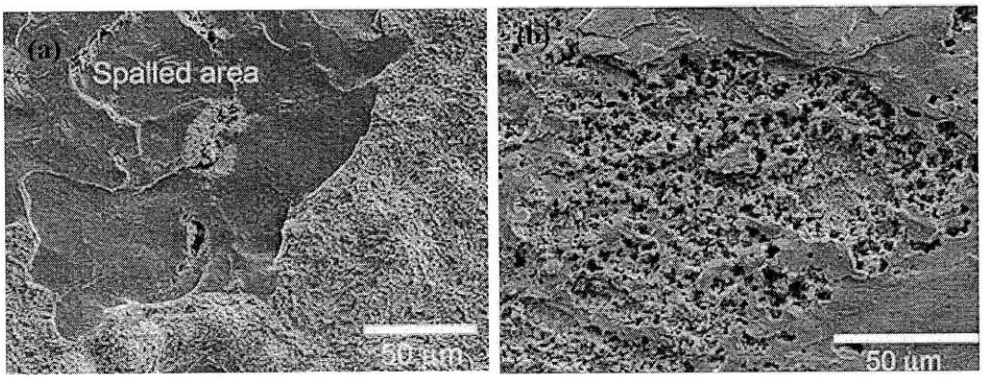

Figure 4. SEM photo showing the spallation of the outer Cr_2O_3 layer at 1100°C after (a) 24h. (b) 200h.

More complete studies in air at 900°C [8, 9] have displayed the formation of a triple oxide layer formed by NiO on the outermost surface, some $NiCr_2O_4$ pockets below and Cr_2O_3 inside. At 1100°C, an outer TiO_2 scale is formed but most of it is spalled due to the difference in thermal expansion coefficient with Cr_2O_3. This results in the exposure of Cr_2O_3 to an oxidizing environment and volatilization becomes significant:

$$Cr_2O_3\ (s) + \frac{3}{2}\ O_2 = 2\ CrO_3\ (g)$$

This reaction limits the temperature at which the alloy can be efficiently used.

As Haynes 230 is the principal competitor for high-temperature applications, it is essential to consider its behavior in terms of corrosion and compare its performances with that of 617. Experiments in air at 900°C [8, 10] show that a double oxide layer is formed with the outer part being the spinel $MnCr_2O_4$ and the inner one Cr_2O_3. This tendency for manganese to concentrate in the outer zone of the scale is explained by its diffusion coefficient being several hundred times larger than that of chromium itself in Cr_2O_3 at 900°C [8]. As for 617, the oxidation kinetics in helium environments are similar to those in air. However the oxidation of alloy 230 is less severe than that of Inconel 617. In fact, the presence of the protective $MnCr_2O_4$ scale instead of NiO in 617 prevents oxygen from penetrating into the Cr_2O_3 layer and consequently decreases the growth rate of the Cr_2O_3 layer. At higher temperatures (above 1000°C) spallation and volatilization also occur but with a smaller rate than in 617 [8].

2.1.4 Effects of impurities in helium coolant

In the primary circuit of high-temperature gas-cooled reactors, helium, used as the cooling gas for the transfer of heat, contains impurities such as CO, CO_2, H_2, CH_4 and H_2O in the microbar range. These impurities are the cause of corrosion phenomena, including oxidation, carburization and decarburization that are highly dependent on temperature and gas composition. The existence of a critical temperature Ta has been demonstrated in several studies [11, 12]. Above Ta, the oxide layer is partly reduced and carbon monoxide is produced by the following reaction: $Cr_2O_3 + 3C\ (s) = 3CO + 2Cr$.

This reaction leads to severe destruction of the carbide microstructure and therefore limits the applicability of the material. The critical temperature significantly depends on the carbon

monoxide partial pressure in helium but surprisingly exhibit almost the same dependence in alloys 617 and 230. This temperature ranges from about 883 to 972°C when the partial pressure of carbon monoxide changes from 0.18 to 5.8 MPa for alloy 617 [12]. This reaction called the "microclimate reaction" [13] is made possible by the reduction of chromium oxide by hydrogen and the attack of carbides by water with formation of carbon monoxide. P_{CO} and P_{H2O} are found to be the two parameters that have to be accurately control to avoid this deleterious reaction.

Although this present work will be focused on the effects of low oxygen partial pressure on the behavior of alloy 617 at 650°C, it is necessary to be aware that the situation of the Intermediate Heat Exchangers is much more complex as it covers a large range of temperature (450°C to 1000°C) and is governed by diverse environmental parameters which all have a particular influence.

2.2 Crack growth in oxygen-containing environments

At high temperature, the effect of the environment can be so high that high-strength superalloys may fail due to enhanced environmental attack. This section will be limited to the influence of oxygen on crack propagation in nickel base superalloys, especially Inconel 617.

2.2.1 Crack propagation under cyclic loading

The theme of environmental sensitivity at elevated temperatures in superalloys has been taken up by Coffins et al. among many others [14]. Comparative fatigue behaviors clearly showed lives of orders of magnitude less in air than in vacuum. Significant effects of temperature and cycling frequency were found in air but not in vacuum. Crack propagation was transgranular for all the vacuum tests and intergranular or mixed, depending on the frequency, for the high temperature air tests. Figure 5 shows the effect of test temperature at a constant frequency. The fatigue life of IN706 is plotted from room temperature conditions to 800°C for both vacuum and air environments. A pronounced minimum in life is observed in air at around 700°C, which leads to an increase by more than one order of magnitude for the lifetime in vacuum in comparison to air at this temperature.

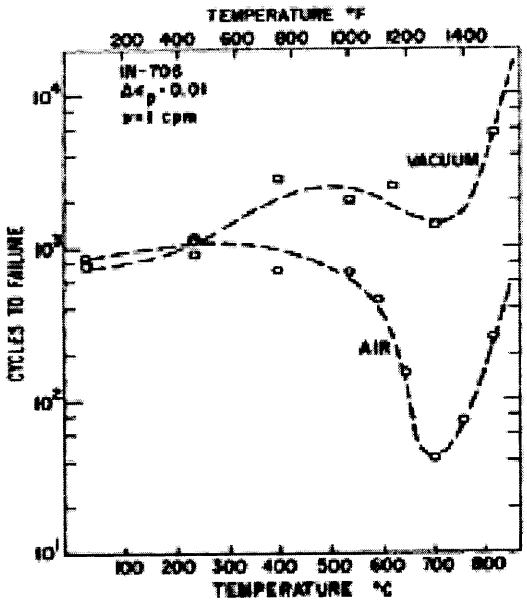

Figure 5. Fatigue life of IN706 as a function of temperature under air and vacuum conditions [15]

Many studies have reported enhanced crack growth rates at elevated temperature, which have been attributed to the presence of oxygen in tests conducted in air. Molins et al. [16] have conducted fatigue tests on alloy 718 at a constant ΔK value under varying oxygen partial pressures and their results clearly demonstrate a critical partial pressure p* (between 10^{-3} and 10^{-2} mbar for 718) at which the crack growth rate changes significantly:

- $P(O_2) < p^*$: crack growth rate low and independent of the oxygen partial pressure
- $P(O_2) > p^*$ but not too high: narrow domain in which the crack propagation rate increases with the pressure
- $P(O_2) > p^*$ but at higher pressures: an upper plateau is reached; the crack growth rate is independent of the pressure

A transition pressure has also been found in alloy 718 by Andrieu et al. [17] and in Ni-Cr alloys [18] and appears to be a function of the chemical composition of the material, especially of the chromium content. The higher the weight content of chromium in the matrix, the higher is the transition pressure. It could result from an oxide formation transition from chromium oxide at low $P(O_2)$ to nickel oxide at higher $P(O_2)$. The absence of environmental embritllement at low pressure has been related to the passivity of chromium oxide, whereas the formation of porous NiO at high pressures may account for oxygen ingress until the solubility limit of oxygen in the matrix is reached (plateau during the third stage) [17].

Service experience of components involves low cyclic loading frequencies, often with long hold times at maximum load and temperature. Whereas high-frequency crack growth is well described by fracture mechanics with the crack length being a function only of the number of stress cycles, at low frequencies, the crack length is a function of both cycle count and time. In the extreme case of low frequency, the crack length (growth rate) may be fully dependent on time and essentially independent of cycle count. These effects have been observed in many superalloys [19]. These results lead to the classification of crack growth processes in two categories: cycle- or time-dependent. High temperatures and low frequencies favor time-dependent processes (creep and/or environmental effects) and low temperatures and high frequencies favor the cycle-dependent process (fatigue). Many service conditions fall in the range of intermediate temperatures and frequencies where a combination of cycle and time-dependent phenomena take place. In this regime, the crack growth is the result of the complex interactions between fatigue, creep and environmental damage [20]. Concerning alloy 617 few studies have been conducted and the main results from Benz [21] and Hsu [22] are displayed on Figure 6. Both of them find an increase in crack growth rate when the frequency is decreased. In air, for R ratios (Load Ratio, Pmin/Pmax) of 0.6 and 0.05, the time-dependence appears at frequency lower than 0.5 Hz [22] whereas in low oxygen pressure environments, processes are always found to be time-dependent [21]. At low frequency (0.1 Hz) the effect of the environment is clearly visible with a sharp increase in crack growth rate when the oxygen partial pressure is changed from 50 ppm to 1000 ppm. However, at higher frequency (2Hz), the difference in crack growth rate is slight, suggesting that environmental factors may be overtaken by mechanical and/or microstructural effects. Lower frequencies probably allow more time for oxygen transport to the crack tip or for the kinetics of the NiO/Cr_2O_3 system to assert itself.

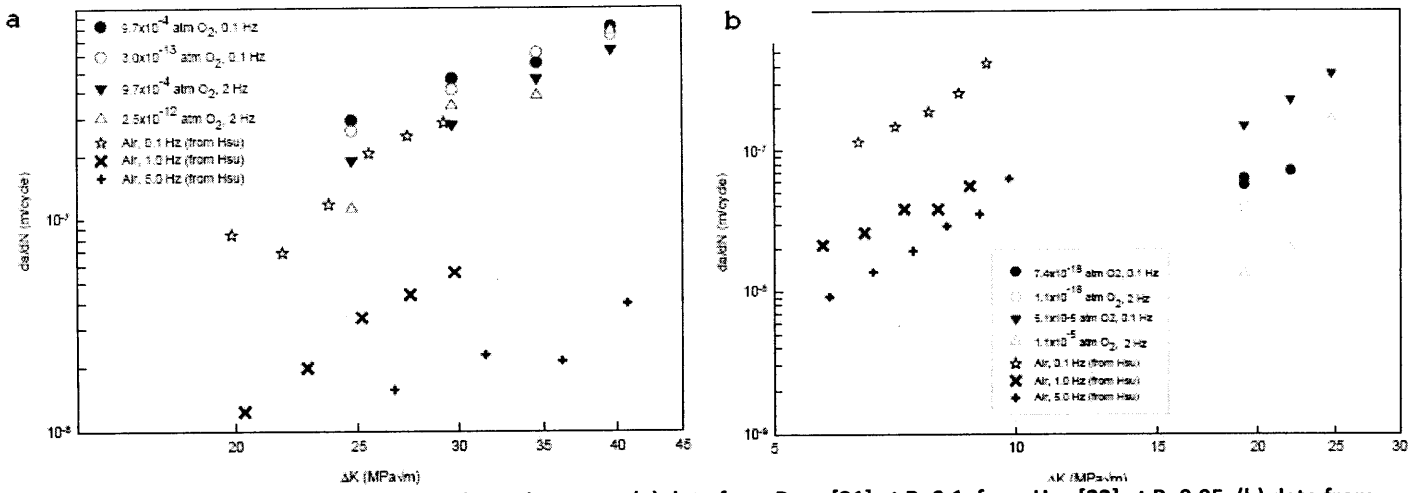

Figure 6. Crack growth rate vs. stress intensity range. (a) data from Benz [21] at R=0.1, from Hsu [22] at R=0.05. (b) data from Benz at R=0.5, from Hsu at R=0.6.

2.2.2 Sustained load crack propagation

Under static loading (frequency equal to zero and R ratio equal to 1) where creep deformation is present, the crack growth rate will be the result of two competitive processes: environmental damage and creep. Various behaviors have been observed depending of the alloy being considered. For example, the crack growth rate for IN718 is around 100 times slower in helium than in air but is reduced at 760°C relative to 650°C due to an increased plasticity and a reduction in yield stress [23]. Most recent studies on IN718 have reported a precipitous reduction in crack growth rate when the oxygen pressure decreases below 10^{-1} Pa [24].

However, this environmental susceptibility is not seen in all nickel base alloys and the influence of the environment varies with the material. This is underlined by Sadananda and Shahinian [25] which define two classes of materials. In one hand are those who exhibit a brittle mode of fracture with a main crack which grows continuously at a rate highly sensitive to the air environment. This is the case for alloy 718 and Inconel X-750 at 650°C. On the other hand, some alloys exhibit a ductile mode of crack growth consisting of nucleation of microcracks ahead of the main crack and joining of the main crack with the most favorably oriented microcracks. This behavior is the one of alloy Udimet 700: the environmental effect is small at all temperatures and creep-related processes dominate. Later, Sadananda and Shahinian have extended their previous study to a large number of alloys (600, 625, X-750, Hastelloy X, PE-16, 800, HS-25) over the temperature range 540 to 870°C in air [26]. Inconel 600 and Hastelloy X did not show any observable crack growth but instead exhibited

continuous deformation leading to crack tip blunting and stress relaxation. All the other alloys were characterized by a critical range of temperature where cracks propagate at a rate which is highly dependent on the alloy and its sensibility to oxygen in air. No correlation of crack growth rates with yield stress of the alloys has been found. Moreover very strong effects of microstructure on sustained load cracking have been reported for both IN718 and IN706 [19]. Special heat treatments including controlled cooling have been able to provide a reduction in crack growth rate by two orders of magnitude by controlling the alloy's chemistry and microstructure.

Concerning alloy 617, very few data exist on the influence of the environment on static loading crack growth and more studies are necessary to determine which process among creep or environmental damage dominates at different temperatures and oxygen partial pressures. Benz observed a particularly surprising trend [21]: by testing at constant K in varying oxygen partial pressure environments, the crack growth rate was found to increase when $P(O_2)$ is decreased in the range of pressures 10^{-3} to 2. 10^{-7} atm. These results clearly differ from those found in fatigue experiments at low R [21]. The crack propagation mode shifts from transgranular to intergranular when the loading mode is changed from cyclic to static with branching and grain boundary cracking away from the crack tip.

2.2.3 Potential mechanisms for oxygen enhanced crack growth

When exploring the literature for the processes responsible for the enhanced crack growth described in the two previous parts, it is clear that many different mechanisms have been proposed but no common agreement has been reached. The first studies on pure nickel recognized that oxygen did not cause embrittlement in the elemental form and that an oxidation reaction was necessary [19]. In their study on cast Udimet 500 subjected to high-temperature, low-cycle fatigue [27], McMahon and Coffin proposed a mechanism starting with intergranular oxidation assumed to occur on boundaries where high stress concentrations existed. In this mechanism, called Oxide Embrittlement or Stress Accelerated Grain Boundary Oxidation (SAGBO), the determining step is the extensive formation of the brittle oxide film along the grain boundary. The authors observed the formation of ridges at selected grain boundaries that were found to be wedge-shaped oxide intrusions, along which a crack could easily propagate. Therefore they proposed that oxide penetration along grain boundaries precedes actual crack formation. Moreover small cracks are sometimes found ahead of the main crack and may act as oxygen sinks and reservoirs for subsequent internal oxidation.

Because they are regions of high defect concentration, grain boundaries provide a rapid diffusion path. They are also regions rich in the strongly oxidizable elements such as aluminum, chromium and carbides. Furthermore a grain boundary can act as a site of stress concentration for externally applied loading. All these reasons lead to a preferential crack growth in the intergranular mode.

The previous mechanism is in contrast to that proposed by Bricknell and Woodford in their embrittlement experiment on superalloy 903 [28]. From their findings, they suggested that the boundary is first embrittled by intergranular oxygen diffusion which then causes the boundary to fail in tension. The boundaries that have been directly exposed to the oxidizing environment oxidize only after fracture. The process repeats itself as oxygen is able to diffuse further down the grain boundary and the next segment of the embrittled grain boundary fractures ahead of the crack tip. This mechanism is validated, they claim, by SEM observations of intergranular fracture still occurring in specimens for whom the external oxidation layer has been removed. Although oxygen in the environment is unequivocally recognized as the damaging species, the question still remains whether the enhanced crack growth rates are due to intergranular oxidation or direct oxygen embrittlement. Figure 7 is a schematic showing the differences between these two mechanisms:

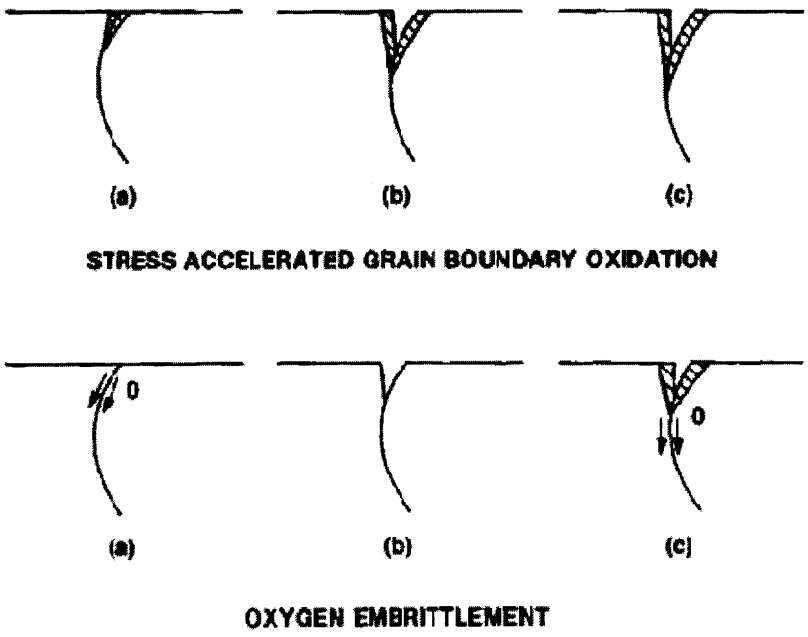

Figure 7. Microstructural phenomena susceptible to occur at the crack tip

In a recent review paper by Woodford [19], the author concisely summarizes the four processes which appear to promote intergranular oxygen embrittlement:

- **Gas bubble formation (CO and CO_2):** An example is shown in Figure 8 where the use of mass spectroscopy has allowed attributing the voids at the grain boundaries to gas bubbles and most likely carbon dioxide, possibly with some carbon monoxide.
- **Release of sulphur:** Oxidation of grain boundary sulphides releases sulphur, which, contrary to oxygen, does embrittle in the elemental form.
- **Precipitation of oxides:** In the absence of carbon or sulphides in nickel, internal oxidation of trace impurities can also occur.
- **Solute segregation:** In this case, the diffusion of oxygen might affect the cohesive strength of grain boundaries.

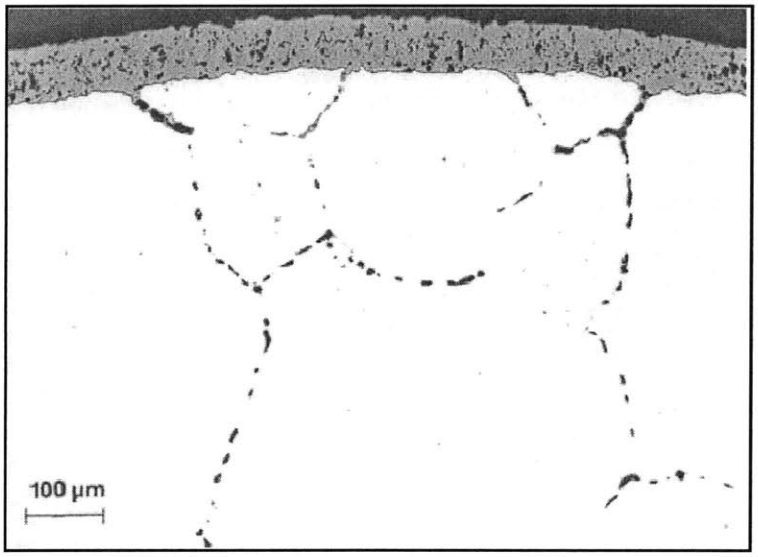

Figure 8. External oxide and internal voids formed in Ni270 after air exposure at 1000°C for 200h [19]

Various investigations have been conducted ahead of crack tips formed in nickel-base superalloys using high resolution SEM, TEM and Auger spectroscopy. Andrieu and Molins et al. [29] proposed that oxidation in IN718 occurs in two stages starting with spinel oxide formation and subsequently chromium oxide formation at the oxide-metal interface. In their TEM studies, the inner layer at the metal-oxide interface was identified as Cr_2O_3 while the outer layer was identified as a spinel oxide $Ni(FeCr)_2O_4$. Delay in forming the passive chromium oxide could allow deeper oxygen ingress and increase in crack growth rates. A recent study conducted in an oxygen pressure of 1 atm at 973°C on nickel base superalloys

and using XPS elemental analysis [30] has been able to detect preferential oxidation of Al, Ti and Nb in Ni_3Al, Ni_3Ti and Ni_3Nb precipitates and Nb-rich carbides over distances of 100 μm ahead of the crack tip. However, in Benz's investigation [21] by mean of Auger nanoprobe (lateral resolution of 10 nm up to 0.1% in composition), no indication of oxide formation or long-range intergranular oxygen transport ahead of cracks grown in a 10^{-3} atm oxygen environment has been found. The diffusion of oxygen, if happening, may extend only on the order of nanometer scale ahead of the crack tip which would not have been detected. The discontinuous change in cracking rate observed by Pfaendtner and McMahon [24] when the oxygen pressure was reduced to extremely low values (10^{-6} atm) has been explained by a shift from diffusion-controlled decohesion to delivery-controlled decohesion. They contend that when the rate of oxygen delivery from the surface is very slow, the embrittling element is carried away from the tip towards the point of maximum stress, before it can cause decohesion at the tip. This phenomenon occurring at very low pressures leads to the blunting of the tip and a discontinuous cracking starting at some distance from the tip.

Furthermore it has been pointed out that oxygen could cause a chemical reaction (possibly with carbon) which would affect the process of grain boundary migration. Observations conducted by Bricknell and Woodford [31] indicate that dynamic recrystallization does not occur in specimens exposed to air at 800°C prior to testing, while the vacuum exposed specimens do show signs of recrystallization. At low temperature, deformation is mainly carried by slip, whereas at intermediate temperature, grain boundary sliding is the main source of accommodation. If embrittled boundaries are not able to migrate anymore, cracks will initiate at regions of high stress concentrations, accordingly leading to a reduction in ductility. At high temperatures, the grain boundaries have enough thermal energy to overcome the source of pinning and ductility is restored. The source and mechanism of pinning is not yet clearly defined.

2.3 Creep behavior of Inconel 617

When the temperature of metals increases above 0.35 Tm, where Tm is the melting point, time-dependent deformation under stress becomes a consideration. This phenomenon commonly called creep cannot be neglected for the use of alloy 617 in high temperature applications since 0.35 Tm lies in the range 466-483°C.

2.3.1 Results of creep testing

Multiple studies have aimed at determining the creep response of alloy 617 with the main varying parameters being the temperature, the level of applied stress and prior heat treatment/processing. Figure 9 shows typical creep curves for alloy 617 under a set of various conditions in air [32]. Theses curves show a near typical shape with a primary, secondary and tertiary stage but the length of each regime is affected by the conditions of temperature and load. These three distinct domains have been clearly observed at 850°C under stresses between 30 and 80 MPa [33, 34]. If temperature or stress is too high, the tertiary stage is reached almost immediately [35]. Following the typical assumption that a structural material must not undergo creep deformation exceeding 1% strain after 1000 hours of loading at different stress levels, alloy 617 could be safely used at 750°C due to its prolonged and stable steady state rates beyond 1000 hours of testing. However it may not be suitable for application under sustained loading for 1000 hours both at 0.25YS and 0.35YS stress levels at 850°C and higher.

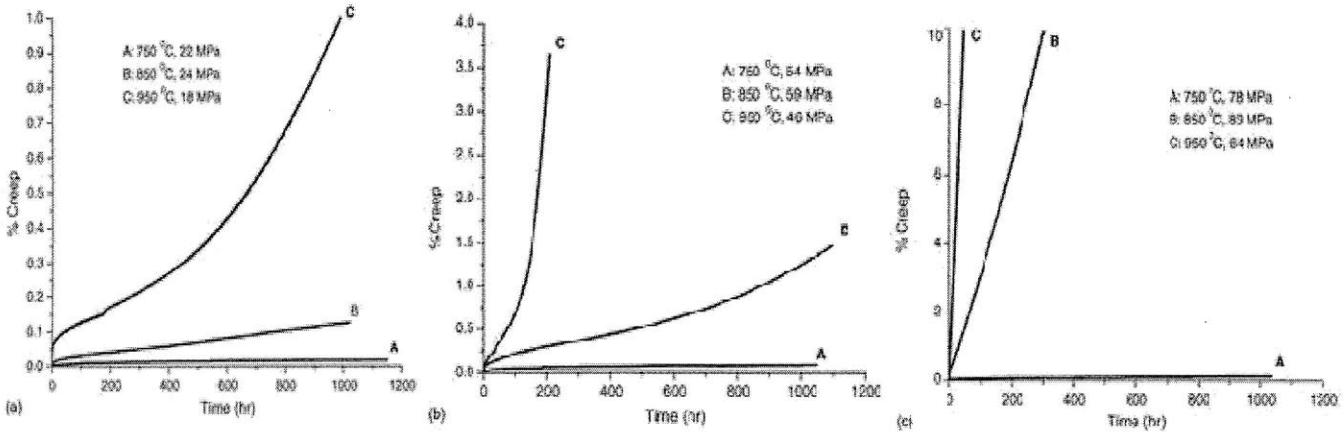

Figure 9. Creep curves of alloy 617 vs. temperature and applied stress. (a) Applied stress = 0.10YS. (b) Applied stress = 0.25YS. (c) Applied stress = 0.35YS

The influence of the environment on creep behavior has also been investigated and the effects of methane and oxygen as impurities have been underlined [36]. The presence of CH_4 at trace level induces cleavage fracture and the creep rupture strain is reduced in comparison to pure He or ($He+O_2$) environments where the failure mode is ductile. However, oxygen-containing environments have a highly detrimental impact as they lead to the shortest rupture life. Similar results are obtained by Hosoi and Abe [37] who found the minimum rupture life

to take place in atmospheres with medium O_2 concentration (500 ppm O_2 in helium) whereas identical values where displayed in pure helium, high vacuum and air. This behavior has been attributed to the presence of a decarburized zone below the surface of the specimen, which tends to reduce the high temperature strength.

The steady state creep rate of alloy 617 is modeled as a thermally activated process by fitting the experimental data with the simple Norton's law:

$$\dot{\epsilon_{ss}} = A\sigma^n \exp\left(\frac{-Q}{RT}\right)$$

where σ is he applied stress, n the stress exponent, Q the apparent activation energy for creep mechanism, A a constant, R the universal gas constant and T the absolute temperature. Some values for n and Q found in the literature are summarized in Table 1. A stress exponent around 5 suggests a dislocation climb-controlled creep behavior [38] whereas n=3 indicates a viscous glide mechanism [39].

Source	Temperature (°C)	Environment	Stress exponent	Activation energy (kJ/mol)
[17]	800	air	4.38	271 for σ=48MPa
	900	air	9.68	
	1000	air	6.26	
[18]	843	Pure helium	6.17	408 (stress independent)
	950		5.02	
	843	Helium + 675 ppm CH_4	5.22	309 (stress independent)
	950		5.05	
	843	Helium + 500 ppm O_2	4.55	No conclusive result
	950		2.38	

Table 1. Values of the creep parameters n and Q obtained with various experimental conditions.

As the Norton equation cannot accommodate strain-hardening or strain-softening, more complex models have been developed [40, 41] in order to simultaneously represent the

three stages of creep. In the early 1980s, efforts were concentrated on developing and implementing unified equations for alloy 617 in order to prepare a draft code case covering the temperature range 649 to 982°C. These models contain a structure-dependent variable to take into account the complexities introduced by the TTP (Time-Temperature-Precipitation) characteristics of the carbides and γ' phase. The use of modified Norton's law leads to the determination of stress exponent n and activation energy Q that are dependent of the level of applied stress. This variation is attributed to a change in creep-governing mechanism with stress [42]. That is why the microstrucural morphology and changes during creep are of high importance.

2.3.2 Microstructure changes during creep

The first data on aging effects for alloy 617 were produced in 1974 by Mankins, Hosier and Bassford [43] who covered the temperatures range of 649 to 1093°C. $M_{23}C_6$ carbides were found to be abundant at all temperatures; carbonitrides [CrMo(C,N)] and nitrides (TiN) were present but rare; the intermetallic phase γ' was rare but present at temperatures up to 760°C. In addition to $M_{23}C_6$, fine M_6C have also been observed after only one hour of aging at 1000°C [44]. Figure 10 provides a TTT (Time-Temperature-Transformation) diagram for alloy 617 [45] which shows that Ti(C,N), M_6C and $M_{23}C_6$ form when the solid solution material is heated to temperatures in the range of 600 to 1000°C and that small amounts of γ' precipitate at temperatures in the range of 550 to 1000°C. The nose of the TTT curve for γ' precipitation is located around 750°C and one hour. It was also observed that the M_6C carbides were dissolved or replaced by more $M_{23}C_6$ carbides at longer times and the nose for this disappearance is placed at 550°C and 1000 hours in the TTT diagram. For aging conditions above 1000°C the diagram displays the formation of $M_{12}C$ (usually known as G phase) carbides and the disappearance of $M_{23}C_6$.

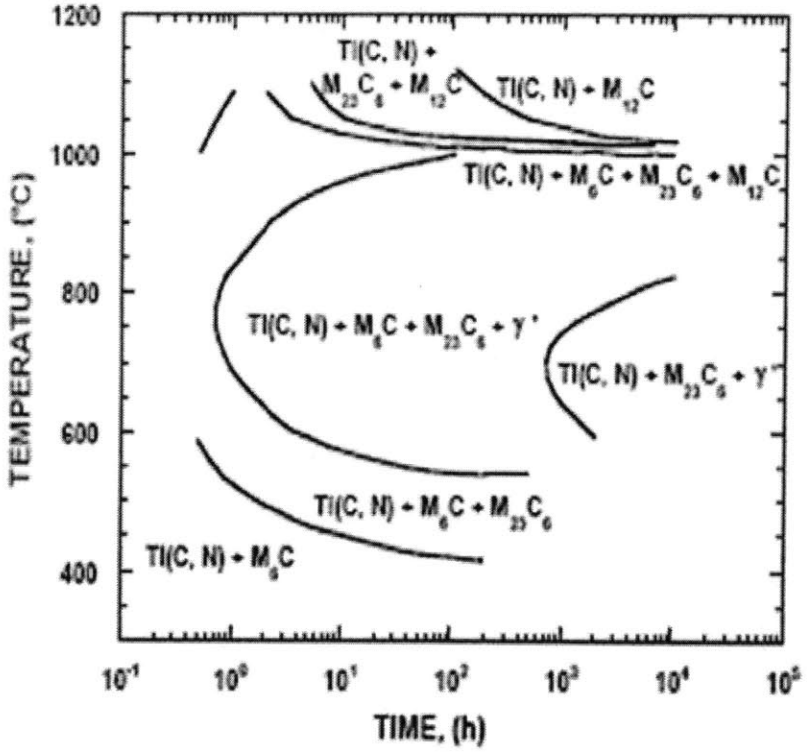

Figure 10. TTT diagram for alloy 617 [45]

The evolution of hardness with aging time and temperature has been extensively used in the examination of the aging response of VHTR alloys. Figure 11 is a plot of recent hardness measurements from Marcello Cabibbo et al. [46] accompanied by values reported in the literature at roughly corresponding test temperatures. The hardening response at temperatures below 650°C is rather slow whereas a significant hardening occurs in the range of 650 to 800°C. This response is the result of extensive intergranular γ'-$Ni_3(Al,Ti)$ precipitation between 700 and 800°C. A competitive strengthening phase Ni_3Mo, called δ, is also detected at 700°C but disappears at 800°C. Aging at 850°C also leads to a peak in the hardness curve which, in this case, is located at around 10 hours when the $M_{23}C_6$ precipitates on slip lines are the most numerous [33]. The hardness is found to fall to levels that are typical of unaged material when aging temperatures exceed 900°C and the γ' phase is no longer observed [47].

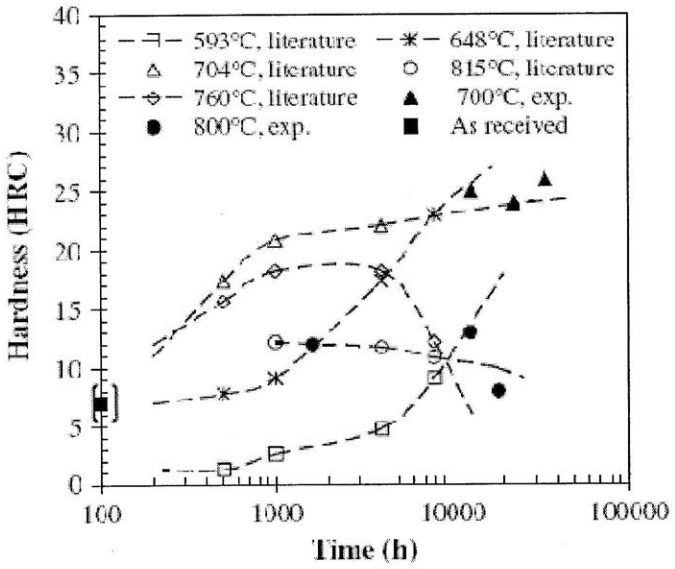

Figure 11. HRC plotted as a function of creep duration for different specimens [28]. The values indicated as literature are from the work of Mankins et al. [43].

The severe creep deformation observed at 950°C at an applied stress of 0.10YS and higher is characterized by the formation of an instantaneous tertiary region on the creep curves and is related to the dissolution of carbides and intermetallic phases. The formation of voids in the tertiary stage accompanied by grain boundary migration and recrystallization has been observed by several researchers [32, 33, 34] and leads to the degradation of the strength of the alloy. The rupture zone appears as completely reformed with recrystallized zones located at grain boundaries (where the carbides mostly were before their dissolution) and formed of multiple fine grains containing twins [33]. During high-temperature creep tests (900°C to 1000°C at creep stresses ranging from 20 to 40 MPa) [48] voids were detected mostly on grain boundaries oriented parallel or perpendicular to the tensile axis as well as 45° to the tensile axis.

In the absence of load, long term exposure of alloy 617 to high temperature usually results in coarsening of the carbides but their distribution remains unchanged [49]. In contrast, under tensile load at 1000°C, the carbides redistribute and are found to be gathered on boundaries perpendicular to the stress axis, as illustrated by Figure 12 from [49].

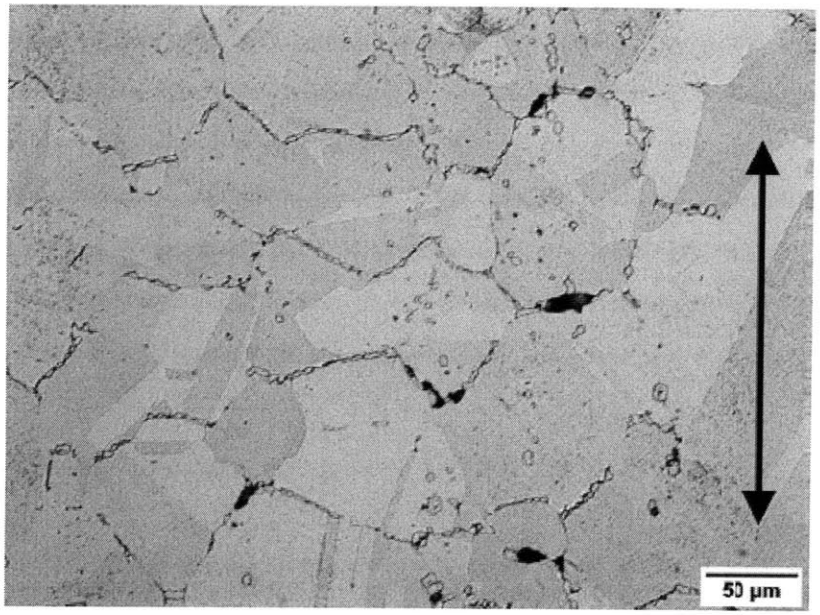

Figure 12. Redistribution of carbides and formation of voids during a creep test at 1000°C. The array indicates the direction of the applied stress

Intragranular carbides are believed to re-dissolve and re-precipitate as grain boundary carbides. Then they are found to be preferentially located on grain boundaries normal to the stress axis to those parallel to it. The driving force for this redistribution is proposed to be the difference in stability of the carbides in compression versus tension [49]. Moreover the majority of the grain boundary precipitates are shown to be Cr-rich ($M_{23}C_6$) carbides. This can be related to the higher diffusivity of chromium versus molybdenum in Ni base alloys. Mo-rich carbides (M_6C) tend to be more resistant to dissolution. The tertiary stage of creep is initiated when grain boundaries free of carbides begin to migrate. The different steps for microstructural change during creep at 1000°C are summarized in Figure 13.

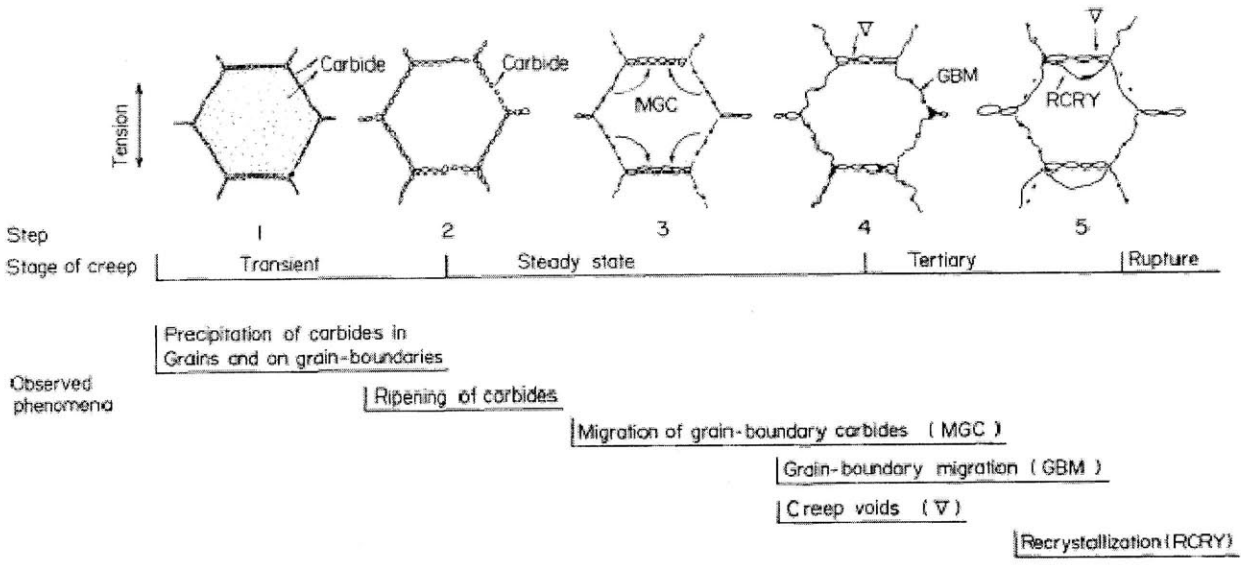

Figure 13. A schematic representation of microstructure changes observed in solution treated Inconel 617 during creep at 1000°C [31]

The present work is an investigation of the behavior of alloy Inconel 617 under static loading at 650°C in low oxygen pressure environments. The goal is to determine which ones among the phenomena described earlier (oxide formation, creep deformation, oxygen embrittlement, aging effects) are relevant in these particular conditions. The temperature of interest in this study (650°C) is the one at which hardening effects are known to become significant. Our alloy is placed in an intermediate domain where neither creep nor environmental damage may dominate but their interaction may give rise to synergistic effects which can either accelerate or delay crack growth. The real mechanism acting in this situation cannot be easily determined and it will be of practical interest to determine which parameters have to be used to correctly characterize alloy 617 in this range of conditions (temperature, pressure and load).

3. EXPERIMENTAL PROCEDURES

In this chapter, the different alloys investigated in this study are presented: not only Inconel 617 but also Haynes 230 and Incoloy alloy 908. Although they are not the main subject of this work, the latter two were used as means of comparison. Haynes 230 has also been identified as one of the primary candidate metallic materials for applications in the Generation IV nuclear reactor systems and differs from 617 only by few aspects. Incoloy 908 is quite different from the two previous ones and of course not a contestant for very high temperature applications. However, it has been chosen as a reference material as it was known to be susceptible to stress corrosion cracking (SCC) in the environment of interest.

Corrosion and mechanical testing have been conducted on these three alloys. The primary goal was to measure crack growth rate at 650°C in environments with varying oxygen potential. For this, a constant K loading was applied to pre-cracked compact tension specimens and the crack length was measured using a direct current potential drop (DCPD) technique. The tests were conducted under environmental and mechanical conditions which are comparable to the ones predicted for component service life. One corrosion experiment and one creep test were conducted later and were aimed at separately studying the different processes that might have acted together in the main testing.

Post mortem analysis included optical microscopy and SEM (Scanning Electron Microscopy) imaging to observe cracking features, fractured surfaces and determine the mode of failure. Special polishing and etching procedures followed by hardness testing have been used to investigate the microstructure and its changes after long-term exposure to the environment. EDX (Energy Dispersive X-ray) spectroscopy has allowed elemental mapping and XRD (X-Ray Diffraction) provided phase identification, especially after the corrosion experiment.

3.1 Materials

The alloy 617 used in this work was provided by Special Metals, Inc. A double melting process was first involved: vacuum induction melting and electroslag remelting. The supplied plate was formed by cold rolling down to a thickness of approximately 19 mm and then solution annealed at 1175°C. The nominal chemical composition is given in Table 2 together with the one of alloys 230 and 908 used for comparison. For both alloys 617 and 230, the high Ni and Cr contents provide high resistance to a variety of oxidizing and reducing

environments. The Al, in conjunction with Cr, offers oxidation resistance at high temperature. Concerning Haynes 230, oxidation resistance is further enhanced by the micro-addition of the rare earth element La. Compared with 617, it has a high W concentration, which, in conjunction with Mo and C, is responsible for the high strength of the material. Alloy 908 is a nickel-iron base alloy, known for its low coefficient of thermal expansion, high tensile strength and sufficient resistance to Stress Accelerated Grain Boundary Oxidation (SAGBO). Table 3 displays the three alloys' basic mechanical properties at room temperature as they are provided by the suppliers.

	Ni	Fe	Cr	Al	Ti	Mo	Co	C	Si	W	Mn	Nb	Cu	La
617	53.55	1.69	21.91	0.96	0.34	9.78	11.42	0.08	0.12	-	0.11	-	0.04	-
230	59	1.34	22.43	0.29	0.34	1.34	0.215	0.11	0.37	13.91	0.53	-	0.04	0.05
908	48.93	41.45	4.01	0.97	1.63	-	-	0.018	0.046	-	-	2.94	-	-

Table 2. Nominal chemical composition of the alloys (in wt. %)

	YS (MPa)	UTS (MPa)	% Elongation
617	356	838	50
230	422	838	50
908	827	1172	12

Table 3. Tensile properties of the alloys at room temperature

Compact tension (CT) specimens were machined from the plate by Electro Discharge Machining (EDM) following the dimensional specifications outlined in ASTM E624-05. The samples were extracted from the plate in the L-T orientation, which means that the cracks would grow perpendicular to the longitudinal rolling direction. As displayed in Figure 14 the specimens were 5.84 ± 0.127 mm thick (dimension B) and the notch was machined to a size ratio a/W = 0.2.

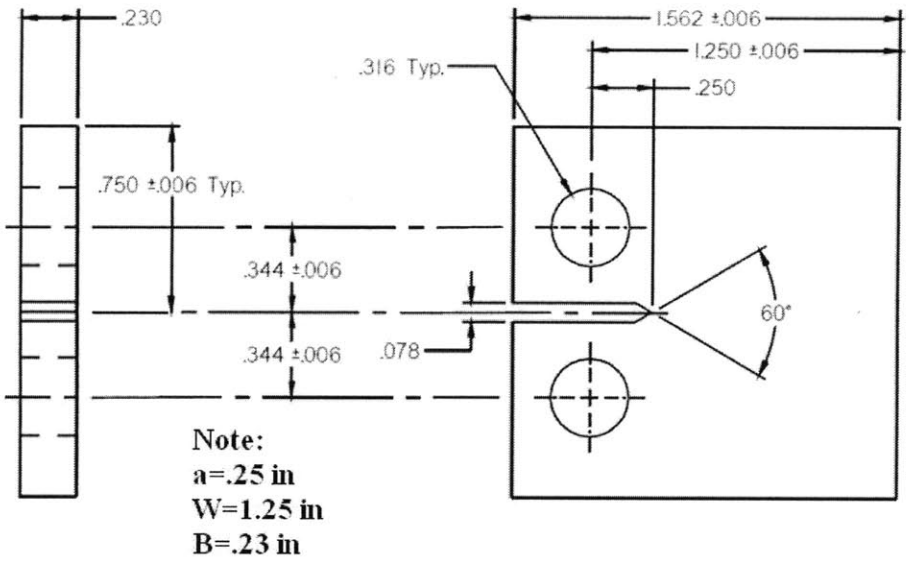

Figure 14. CT specimen geometry (All the dimensions are in inches)

3.2 Constant K crack growth tests

3.2.1 Experimental setup

The experimental setup for the constant K tests is schematically presented in Figure 15. The CT specimen and retort are heated by the furnace (Applied Testing systems series 3210 Split Tube furnace). The system allows accurate measurements of temperature and oxygen concentration of the bulk gas flowing through the retort chamber. The oxygen partial pressure was varied in the test chamber by circulating either ultra-high purity argon gas or commercially pre-analyzed gaseous mixtures of oxygen and argon from 10 to 1000 vppm oxygen in argon. For the tests run in argon, inert conditions were achieved by making the ultra-high purity argon provided by Airgas flow through a gettering furnace before entering the chamber. Oxygen potential was also measured directly adjacent to the specimen surface using a Yitria stabilized zirconia oxygen probe.

The temperature was held constant at 650°C for all tests. The oxygen probe contains its own thermocouple to allow calculation of the oxygen potential via the Nernst equation. Two supplementary thermocouples measure the temperature of the atmosphere inside the chamber: one K-type thermocouple which also feed back into the temperature controller and one R-type thermocouple attached to the ZrO_2 oxygen probe. Because of interferences with the direct current potential drop (DCPD) technique that was used to measure crack extension,

no thermocouple could be directly welded to the surface of the sample. However a third thermocouple was welded to the Alloy 718 pin/grip assembly as close as possible to the specimen. These three different temperature measurements allowed a control within ±3°C. The top and the bottom parts of the retort were cooled by coolant circulation during high temperature test.

During the tests the loads were applied by an MTS (Mechanical Testing Systems) servo-hydraulic load frame controlled by Instron 8500. The load frame controller receives the commands from the computer.

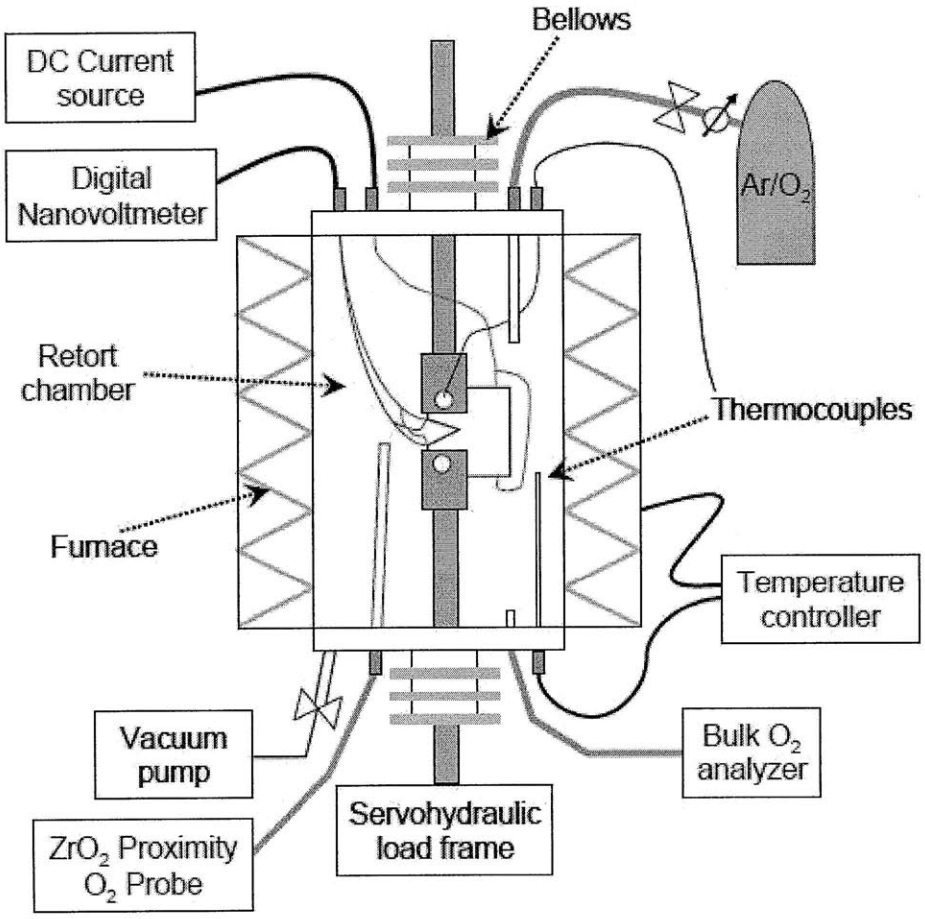

Figure 15. Schematic of the experimental setup for constant K crack growth tests

3.2.2 Direct current potential drop technique

The Direct Current Potential Drop (DCPD) technique is used for crack length measurement. It is based on the relationship between the electric resistivity and the geometry of the specimen, which is described by the Ohm's law:

$$V = \frac{I\rho l}{A}$$

where V is the electric potential drop measured between two electric nodes, I is the applied electric current, ρ is the electric resistivity of the material and A is the cross-sectional area of the conductor. As the crack grows, the value of l/A is increased due to the reduction of A and the increase in l. It results in an increase in the measured electric potential drop. To calculate crack length via a potential drop measurement, the ASTM E647-05 standard suggests using a second CT specimen as a reference. This reference has to be exposed to the same environment as the test specimen with the exception of the mechanical loading and the crack length is calculated by mean of a correlation which exists between this length and the ratio of the potentials (V_{test} /V_{ref}). Due to the small space available inside the retort, no reference specimen could be used. Instead, a closed form DC potential drop fit equation valid for an a/W range of 0.38 to 0.75 and developed by Andersen at GE (Appendix B) was used. Since all of the experiments were conducted at a single temperature it was felt that this arrangement would be sufficient.

The DCPD measurement system was run in current control mode at 2 amperes. Two separate potential measurement channels were used, each of them having contacts welded at opposite corners of the machined crack mouth opening. For each potential drop measurement, four readings were taken: two readings for each channel and the second set being recorded with the reversed current polarity. The four readings were then averaged and recorded as one potential drop measurement. When ten potential drop measurements were recorded, the values within one standard deviation of the mean were averaged and constituted one data point recorded in the data file provided by the PC. A custom suite of software written in Visual Basic controls the overall system and the PC has the following functions: setting up the instruments for the DC potential drop measurement, recording the DCPD values along with environmental (temperature, oxygen partial pressure) and mechanical (displacement) variables and communicating with the Instron load frame controller. A schematic of the control system and DC potential drop setup is shown in Figure 16.

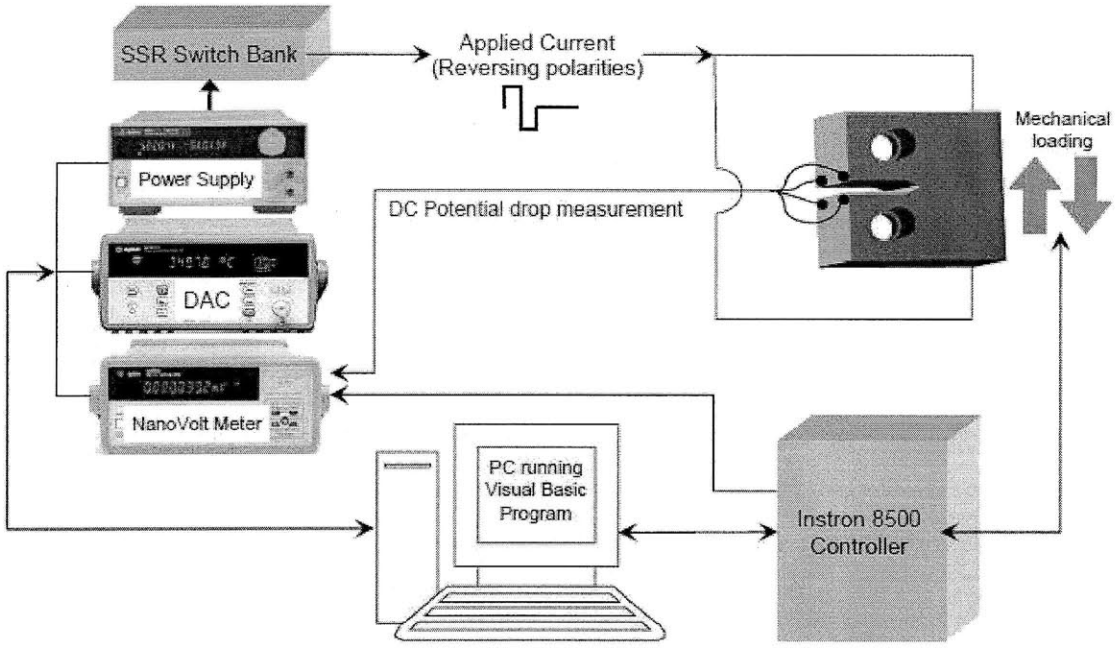

Figure 16. Schematic illustration of the control of the mechanical testing system

3.2.3 Test procedures

As the goal was to study crack propagation and not initiation, the specimens were first precracked at room temperature with a loading frequency of 25 Hz and a load ratio of 0.1 up to a minimum a/W=0.38. The goal was to obtain a straight and sharp precrack which represents a preexisting flaw in a real component. Careful consideration was given to the ΔK applied to the specimens during precracking as it must not exceed the values used in the actual testing. The final precracked length was measured under load with 0.01 mm accuracy using a dial gage mounted on an optical microscope. When the sample was set up in the retort system and the temperature and chemistry had reached the desired value, 80% of the initial load was applied. Then, the final precracked length was entered into the Visual Basic program which calculated a correlation between the length provided by the user and the measured potential drop voltage. This initial DC potential value together with the corresponding crack length served as the reference specimen and was used for all subsequent measurements.

Although the final goal of this study was to concentrate on the effects of static loading, preliminary fatigue steps were introduced to progressively reach the desired loading state and obtain a sharp crack tip by decreasing the frequency to 0, increasing the R ratio to 1 and the stress intensity factor K to the desired level. This procedure was necessary to avoid crack arrest when static loading was applied. The last step before static loading applied a trapezoidal

waveform with 500s hold time at maximum load and R=0.88. An example of a typical test plan, as it has to be provided by the user to the computer, is displayed in Table 4. All the other test plans used for this work are reported in Appendix A. Particular attention was given for the test to conform to the size requirements of the ASTM E647. The size of the uncracked ligament (= specimen width - crack length) in combination with the applied stress intensity factor must satisfy the following inequality: $(W-a) > \frac{4}{\Pi}(\frac{K_{max}}{\sigma_{FS}})^2$ where σ_{FS} is the flow stress of the material (i.e. the mean of the yield stress and the ultimate tensile strength). For a maximal K of 45 $ksi\sqrt{inch}$ (i.e. 49.45 $MPa\sqrt{m}$) and considering the mechanical properties of alloy 617 at 650°C, it leads to a maximal value of the ratio a/W of 0.7012. If this value is exceeded, the specimen will not be in the elastic regime anymore and large scale plasticity yielding may occur at the crack tip.

Steps	Frequency (Hz)	Wave Form	Hold time (s)	Kmax ($ksi\sqrt{inch}$)	R	Step end (a/W)
1	2	Sine		35	0.5	0.4126
2	0.1	Sine		35	0.5	0.4284
3	0.01	Sine		40	0.63	0.4331
4	0.005	Sine		40	0.75	0.4362
5	0.002	Trap	500	45	0.88	0.4378
6		Cnst		45	1	0.55

Table 4. An example of test plan for specimen 617-CT-35 with an initial ratio a/W = 0.4088 after precracking

3.3 Corrosion experiment

This experiment was aimed at determining the behavior of three nickel base alloys in a low-O_2 environment (Argon + 50ppm O_2) in absence of any load in order to distinguish between the mechanical and environmental influences that seemed to be entangled in the crack growth tests. A schematic of the experimental set-up is provided by Figure 17. A Linberg furnace with a programmable Eurotherm controller was used to maintain the temperature to 650 ± 3°C during 500 hours. The chamber was first put into high vacuum (up

to 10^{-6} torr) and then the commercially pre-analyzed gas mixture of 50 vppm oxygen in argon was allowed to circulate at a regulated flow rate of 0.2 cc/min. The samples used were coupons with a thickness of 5.84 mm and a surface area of about 2 cm^2.

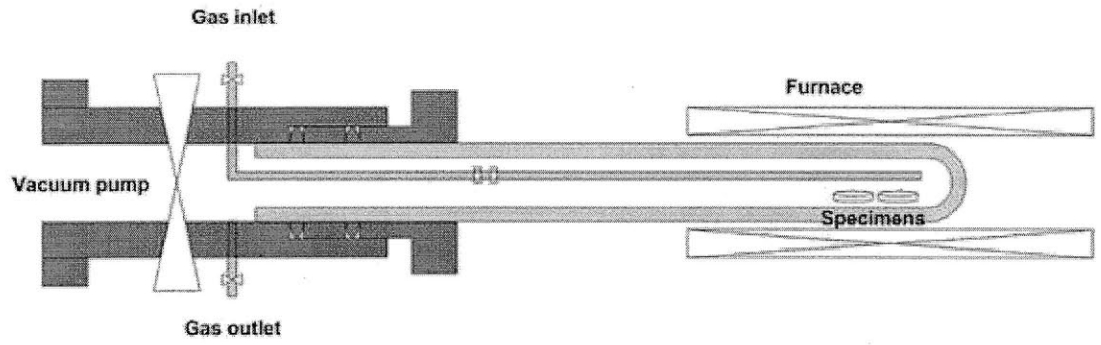

Figure 17. Schematic of the experimental set-up of the corrosion experiment

After 500 hours in the environment, the furnace was cooled down at a controlled rate (- 65°C per hour) and the specimens were kept in a dessicator for later observations and analysis.

3.4 Creep testing

With the same objective as previously discussed (i.e. separate the effects of the environment to the ones due to the mechanical conditions), one sustained load experiment has been conducted in an inert environment (high purity argon). In this case the exact same system as the one used in the constant K tests (retort + furnace with temperature and composition controls) was transposed into a dead-weight testing machine. The lever arm (Applied Test Systems Series 2410) allowed for accurately maintaining a constant load (up to 20000 pounds) over long periods of time. Figure 18 is a photograph of the experimental set-up for the creep testing system. As the goal was to investigate the deformation behavior of alloy 617 in the environment of interest, a CT specimen without any precrack was set-up into the chamber and the applied load was determined to get a stress concentration factor K of 45 ksi$\sqrt{}$inch at the notch. As the notch was quite sharp, the necessary tensile load was directly calculated by the mean of the following formula, commonly used for a crack in a CT specimen:

$$K_I = \frac{P}{B\sqrt{W}} f(\frac{a}{W})$$

with $f\left(\frac{a}{W}\right) = \frac{2+\frac{a}{W}}{(1-\frac{a}{W})^{3/2}} [0.886 + 4.64\frac{a}{W} - 13.32\left(\frac{a}{W}\right)^2 + 14.72\left(\frac{a}{W}\right)^3 - 5.6\left(\frac{a}{W}\right)^4]$

It results in a load of 1.21×10^4 N which leads to a weight of 135 pounds by using the 1:20 ratio on the lever arm. The displacement was measured by mean of a dial gage with a sensibility of 1/1,000 of an inch (= 0.0254 mm). As recommended in the standard ASTM E139-00, frequent readings were recorded, especially during the rapid first stage of creep (every one hour).

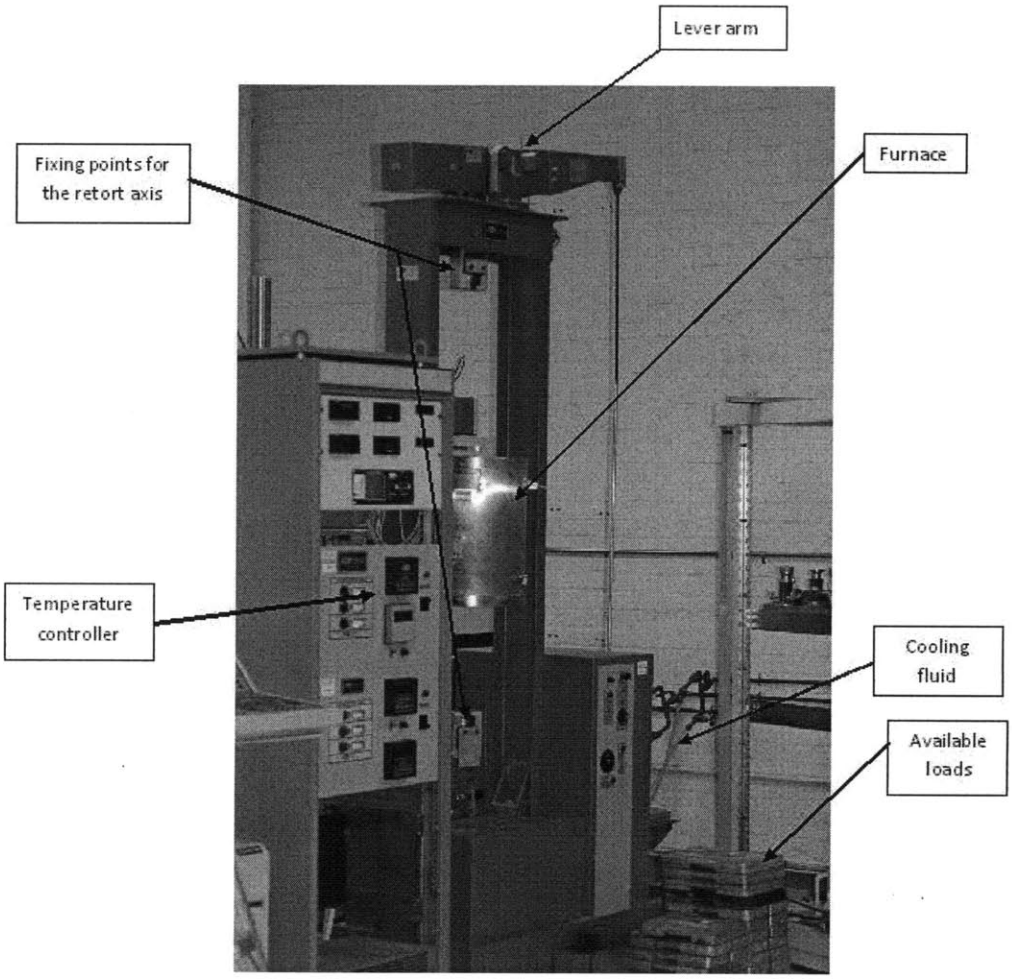

Figure 18. Experimental set-up for the creep test.

3.5 Microstructure investigation

The microstructure of several samples from the three alloys has been determined by polishing and etching. First, the samples were mechanically polished in successive steps with the grit size being smaller and smaller down to 0.05 μm obtained with an alumina suspension. During each step, a weight of 4 pounds per sample was applied for 3 minutes with the rotation speed of the plate being 150 rpm. This procedure allowed getting microscopically flat samples and eliminating all kinds of roughness.

To make the microstructural features (grain boundaries, carbides, precipitates) visible, electro-etching was performed. The Struers LectroPol-5 electro-polisher enabled to adjust the applied voltage and the time of the treatment. Table 5 summarizes the solutions and experimental conditions chosen for each of the alloys.

Alloy	Solution	Composition	Conditions
617	A2	10% distilled water, 73% ethanol, 10% butoxyethanol, 7% perchloric acid 70%	8 V for 25s
230	Nital	5% HNO3, 95% Ethanol	5 V for 35s
908	Nital	5% HNO3, 95% Ethanol	3 minutes immersion, no voltage

Table 5. Etching procedure

In addition to the observation of the microstructure, the hardness of each sample was measured to characterize the materials in their as-received conditions but also to detect any change in hardness due to exposure to the test environment. A Leco's LM-Series Microindentation Hardness Testing System was used for that purpose. It involves a diamond indenter in the form of a square-based pyramid with an included angle of 136°. In this configuration, the Vickers hardness number is given by: $= \frac{F}{A} \simeq 1854.4 \frac{L}{d^2}$, where L is the applied load in grams and d is the average length of the diagonal left by the indenter in mm. Before a set of measurements, a sample of known hardness was used to make sure the calibration of the instrument was correct. During each measurement, a load of 500 grams was applied and the system provided both the Vickers (HV) and Rockwell (HR) hardnesses.

3.6 Fracture analysis

After constant-K testing, two different types of investigation were performed on the specimens using a TOPCON ABT-150 scanning electron microscope with either a tungsten or LaB_6 filament: first surface inspection and then, fracture surface observation after the specimen was entirely pulled apart to create two halves. The first step aims at observing the crack path and morphology, the second one at determining the mode of fracture. Images of the sample surface topography were obtained by collection of accelerated secondary electrons resulting from the inelastic interactions between the atoms at the sample's surface and the high-energy electrons beam emitted by the filament. The tungsten filament allowed for a magnification up to 10.000x, whereas the LaB_6 one can reach 50.000x. SEM imaging was also used to observe cross-sections of the corrosion samples and determine the morphology (thickness, porosity) of their oxide layer.

3.7 Compositional analysis

Two different techniques were used to get compositional information: Energy Dispersive X-ray Spectroscopy (EDX) for elemental analysis and X-Ray Diffraction (XRD) for phase's identification. The SEM, previously described, is equipped with a Noran Vantage X-ray detector whose characteristics are a 7µm Be window, a 31° take-off angle and a working distance of about 25 mm. It collects the X-rays emitted when the electronic orbitals of atoms in the sample are disturbed by the high-energy electron beam. The energy of the collected radiations is characteristic of the element interacting with the beam and the resulting spectrum allows for quantitative information about the composition of the surface. Point analyses, line scans and compositional maps can be obtained.

As EDX is limited to the elements, XRD analysis had to be performed for compounds identification. The diffractometer used was a PANalytical X'PertPro with a copper anode (K_α= 1.54060 $\dot{A}$, K_β = 1.54443 $\dot{A}$). The settings of the generator were 40mA and 45kV and the surface of each corrosion sample was scanned for 30 minutes. From their interaction with a particular crystallographic phase, the incident X-rays are diffracted at certain angles and give rise to a diffraction pattern whose peaks intensities and positions are characteristic of the compound. The latter can be identified by comparison with the library of known crystalline materials from ICDD (International Center Diffraction Data).

Alloy	Vickers hardness HV	Rockwell hardness HR
617-surface	200	92.9 (HRB)
617-thickness	216	95.9 (HRB)
617-(exposed 500 hrs at 650°C)	293	28.9 (HRC)
230	221	96.8 (HRB)
908	306	30.5 (HRC)

Table 7. Hardness measurements

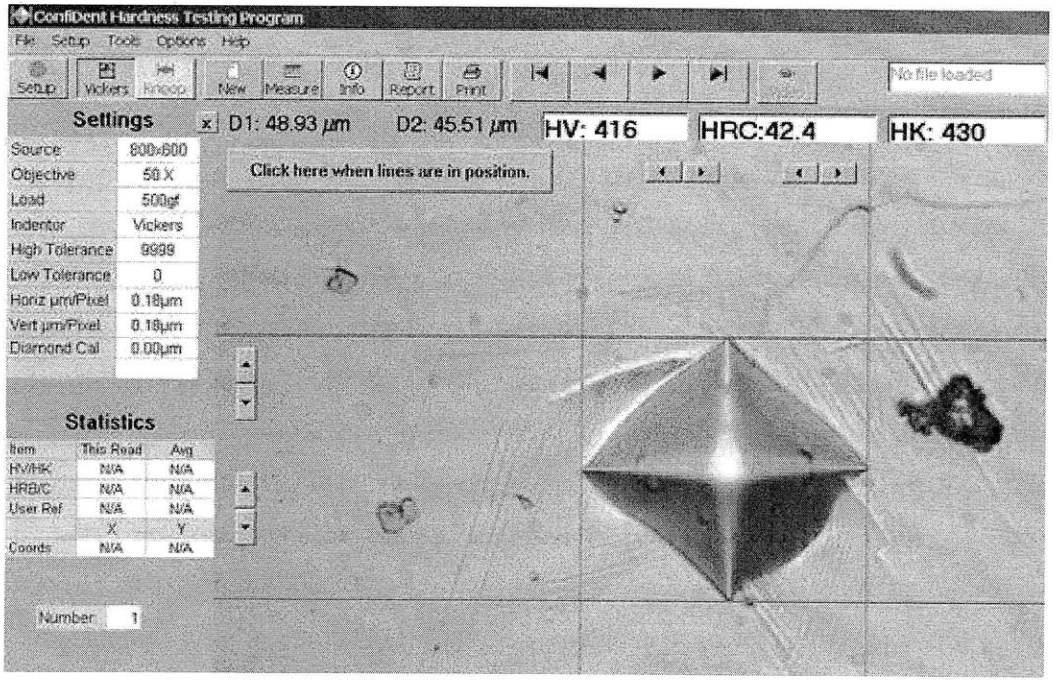

Figure 23. Screen shot during hardness measurement

4.2 Crack growth tests

In this section we extend the work of Benz to more fully explore the behavior of alloy 617 at 650°C under static loading. His main results were particularly surprising and needed further investigation. In fatigue testing at low frequency, a pronounced effect of the environment had been found, in the sense that increasing the oxygen partial pressure led to a significant increase in crack growth rate. However when testing in static loading, this trend seems not to

be observed anymore: at a K of 30 ksi√inch, no effect of the environment was observed and the crack growth rate was the same at all oxygen pressures; at a K of 45 ksi√inch, the crack growth rate increased when the oxygen partial pressure was decreased. The experiments described in the following sections will try to shed light on this strange behavior and understand what really happens.

4.2.1 Alloy 617 in pure argon environment (sample 617-CT-36)

The first test was conducted in an inert environment (ultra-high purity argon with an oxygen partial pressure of 10^{-22} atm) at 650°C and a constant stress intensity factor of 45 ksi√inch (= 49.45 MPa√m). This value was chosen to be sure to observe enough crack growth and to establish a reference crack growth rate in an inert environment, allowing for further comparison when the environment or the load will be changed later. Moreover this value is realistic and is of the order of magnitude that could be obtained at a preexisting and undetected flaw in a component. During the test, as the stress intensity factor was hold constant at the crack tip, the load was decreased as the crack grows to maintain a constant value of K. Figure 24 is a plot of the crack length a in centimeter versus time in hours.

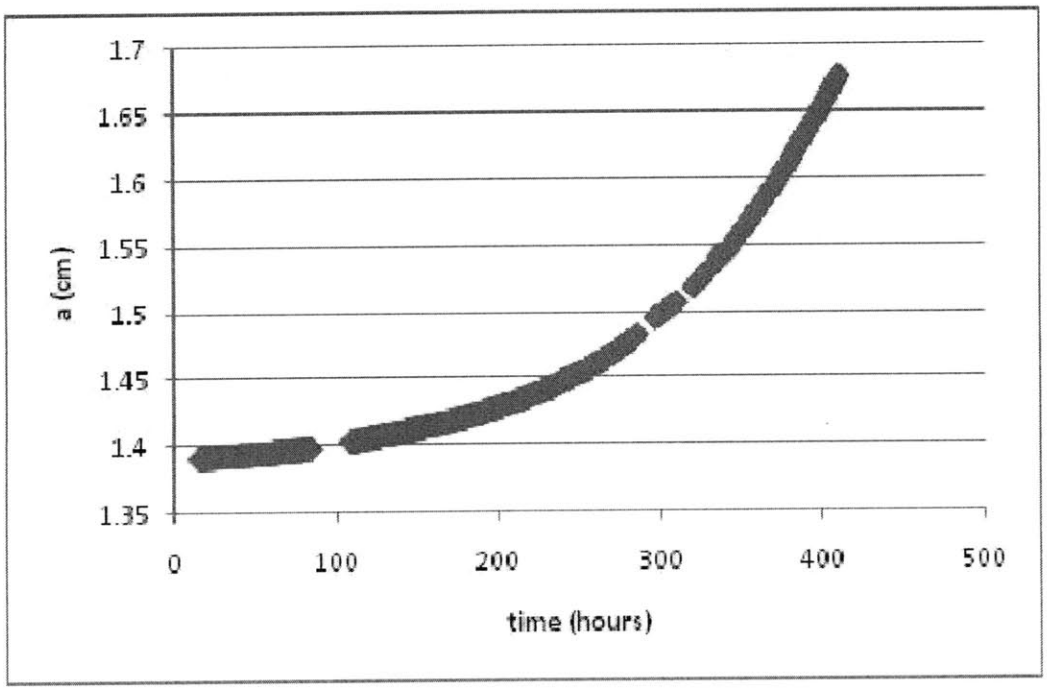

Figure 24. Crack length versus time (K=49.5 MPa√m; P(O2)= 【10 】^(-22) atm).

The obtained curve is particularly surprising as it reveals a time-dependent behavior. Although the environmental composition and the loading conditions are unchanged during the whole period of time, the growth is not linear at all, as it would be expected for a constant K with the assumptions of linear fracture mechanics. The behavior is parabolic and contrary to the case of fatigue testing, no unique crack growth rate can be defined to characterize these conditions of load and environment and it seems that the crack grows at an increasing rate with time. An estimation of the crack growth rate has been obtained on successive intervals of 328 data points by calculating the difference quotient on each interval and has been plotted versus time in Figure 25. The general trend is an increase of the crack growth rate with time during the first 350 hours at an accelerated rate to finally reach a plateau. In fact, it seems that a steady state is reached after 350 hours after which the crack grows at a constant rate. To accurately calculate this constant growth rate a linear regression has been performed using all the data points from 340 hours to the end of the test. It provides a slope of 0.0006 in term of a/W versus time, which corresponds to 0.0019 cm per hour (= 19 µm/h). Figure 26 displays the result of this regression which gives a good coefficient of correlation (R^2=0.9977). The general non-linear behavior indicates that time-dependent phenomena occur at the crack tip and the stress intensity factor K does not seem to be well-suited to describe them.

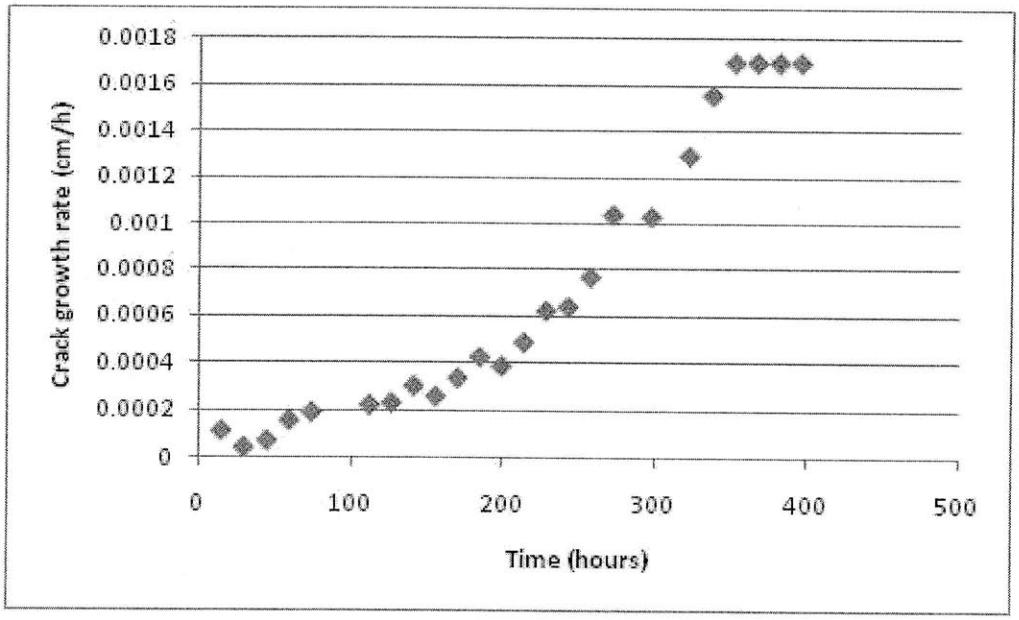

Figure 25. Crack growth rate versus time (K=49.5 MPa√m;P(O2)= ⟦10 ⟧ ^(-22) atm)

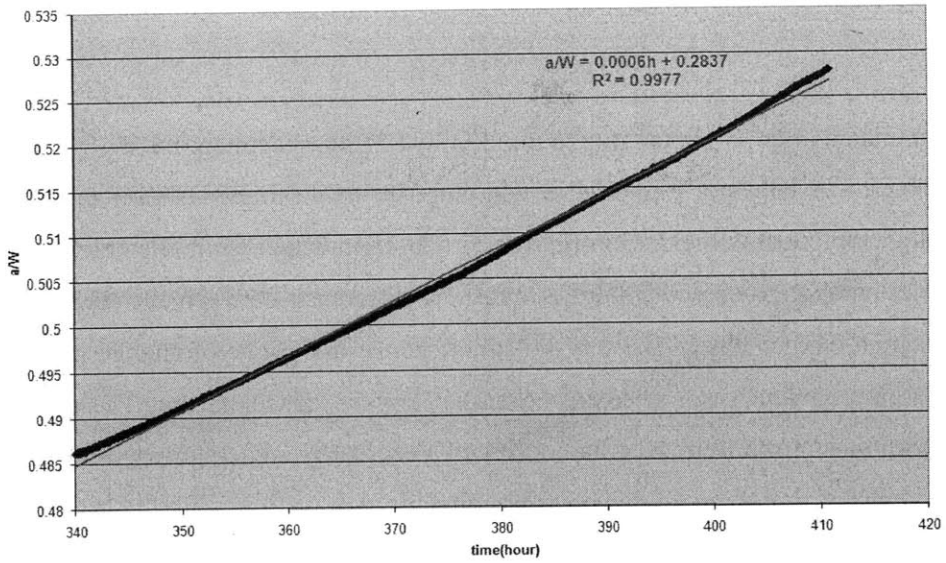

Figure 26. Linear regression to obtain the steady state crack growth rate (K=49.5 MPa√m; P(O2)= 〖10〗 ^(-22) atm)

4.2.2 Influence of the environment (samples 617-CT-22 and 617-CT-35)

The goal of this section is to investigate the effect of an increase in oxygen partial pressure on the non-linear behavior previously described. For sample 617-CT-22, the environment was changed from ultra-high purity argon to 10 vppm oxygen in argon ($P(O_2)$ measured to be around 8. 10^{-6}atm) after 170 hours, while maintaining a K of 49.45 MPa√m at the crack tip and a temperature of 650°C. The results plotted in Figure 27 show a curve with a parabolic shape, generally similar to the one obtained in pure argon and, while there appears to be two separate parabolic shapes, one for each environmental condition, the change of environment does not seem to affect this general trend.

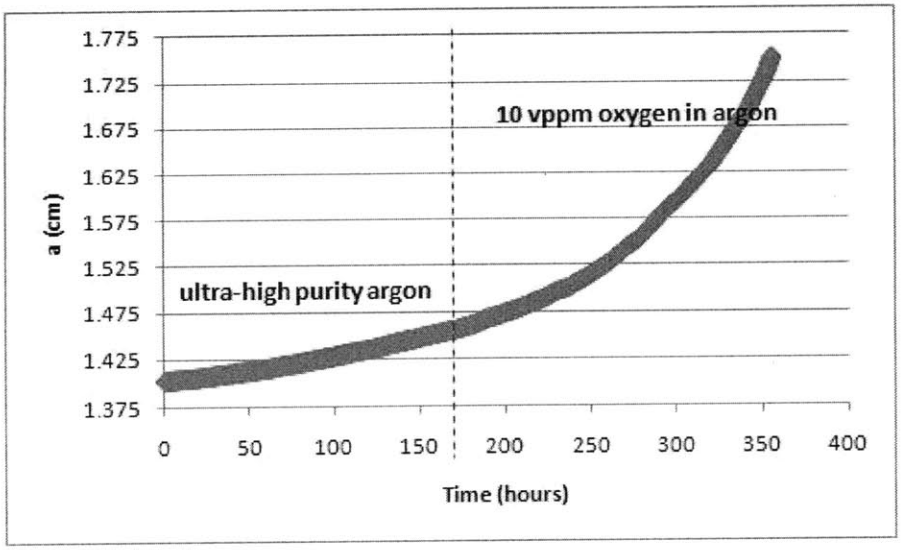

Figure 27. Crack length versus time with a change of environment (sample 617-CT-22)

The test was terminated after 356 hours due to rapid failure of the specimen. As shown in Figure 28, the crack growth behavior exhibited a continuously increasing rate until the specimen fails (vertical asymptote). As the data in figures 27 and 28 indicate, while the crack growth behavior exhibits parabolic behavior, there is indeed a difference between the high purity argon and the 10 ppm oxygen case. There is a distinct change in the rate of change in crack growth when the environment is changed to the higher oxygen concentration. These results are at variance with those from Benz who had observed a decrease in crack growth rate with increasing the oxygen partial pressure in this pressure range.

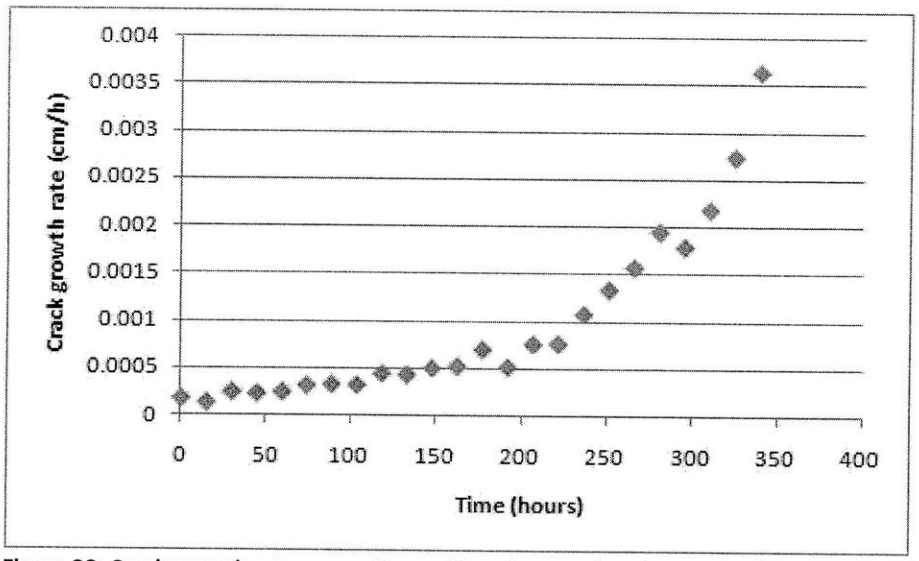

Figure 28. Crack growth rate versus time with a change of environment after 170 hours (sample 617-CT-22)

The experiment conducted by Benz was performed in a decreasing oxygen partial pressure environment with time. He observed an increase in crack growth rate with a decreasing oxygen partial pressure. Figure 29 shows his results for static crack growth.

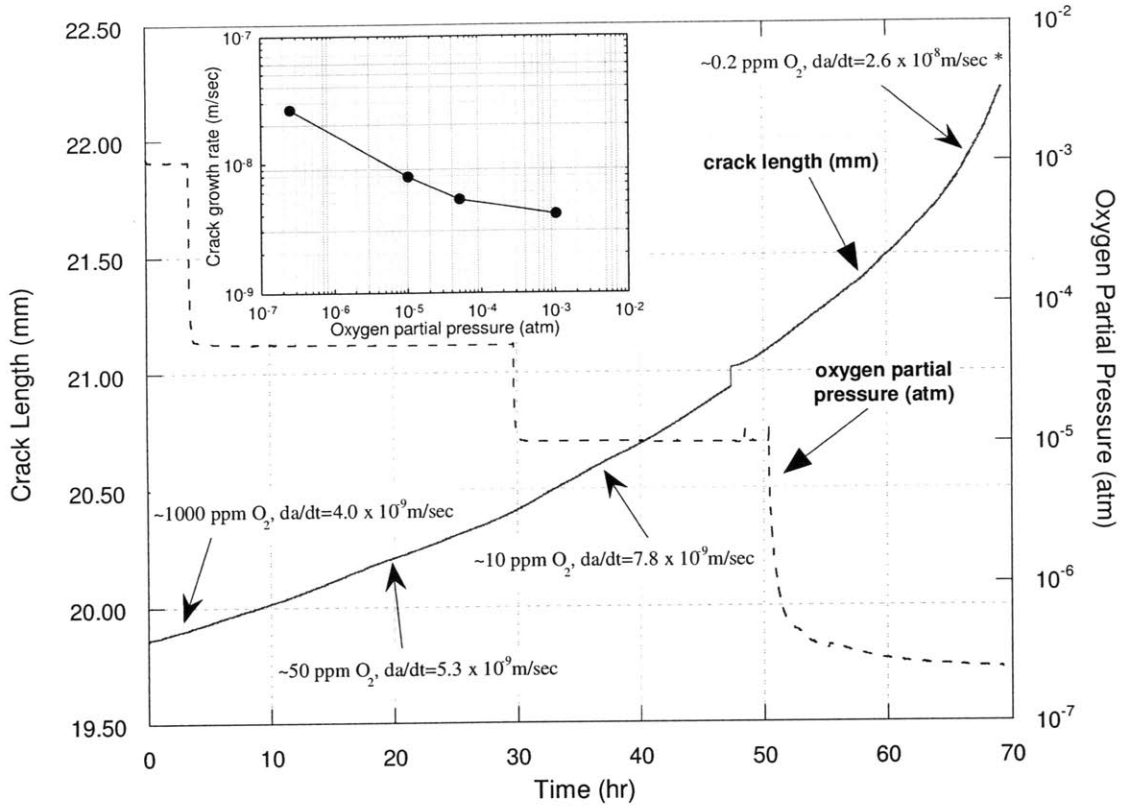

Figure 29. Static crack growth behavior for alloy 617 as a function of oxygen partial pressure at 650°C and K=49.5 MPa√m from Benz [21].

The results from this work appear to show the opposite behavior. Thus, confusion exists and it appears that the situation is more complicated than a simple effect of the environment. To further explore this, a test was carried out by following the same experimental order of oxygen concentration change as Benz. This test (sample 617-CT-35) began in a 10 vppm environment and switched to argon later. The results of this test are shown in Figure 30. As shown in Figure 30, two changes of environment were imposed: from 10 vppm oxygen in argon ($P(O_2) = 4x10^{-5}$ atm) to ultra-high purity argon ($P(O_2) = 2x10^{-21}$ atm) at around 330 hours and then to 50 vppm oxygen in argon ($P(O_2) = 8x10^{-4}$ atm) at around 570 hours. Despite the changes in environment, the individual curves are still parabolic with an increase of crack growth rate with time. However, there is an apparent effect of oxygen partial pressure. The crack growth rate first increases with decreasing oxygen concentration from 10 vppm O_2 to high purity argon and then increases again with the change from high purity argon to 50 vppm O_2. However, the crack growth rate at 50 vppm O_2 is higher than both the 10 vppm O_2 and the high purity argon case. Nonetheless, the crack

growth rate is also changing with time during each time increment. From these results, we can infer that a time-dependent process is involved in combination with an environmental effect for alloy 617 under these particular conditions (T=650°C, K=49.45 MPa$\sqrt{m}$). The thermal and mechanical effects appear to interact with the environmental effect to yield the observed behavior.

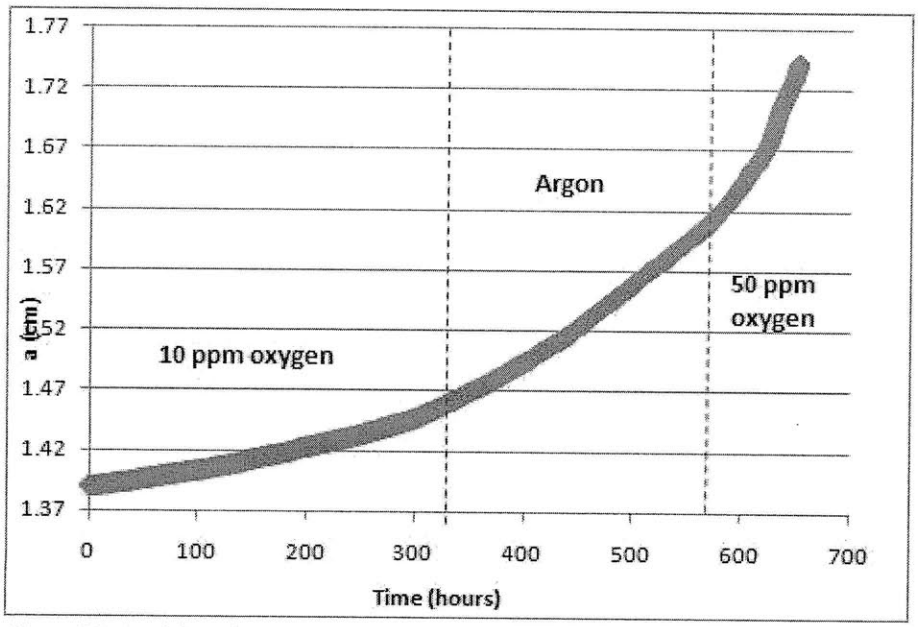

Figure 30. Crack length versus time (sample 617-CT-35)

4.2.3 Influence of the stress intensity factor level (sample 617-CT-29)

The suspicion that time dependent behavior was acting in combination with the environment to yield the complex behavior observed suggested that further exploration of the effect of stress intensity factor on the observed behavior was needed. While 650°C was expected to be low enough to exclude creep from being a significant factor, this may not have been the case when very high crack tip stresses may exist. In this test the crack growth behavior was explored at a significantly reduced value of stress intensity factor. The goal of the following experiment was to understand the role that the high stress intensity factor may have had on the previously observed behavior for alloy 617. For this, the stress intensity factor was reduced to 38.5 MPa$\sqrt{m}$ during the static loading step. The exact test plan applied to sample 617-CT-29 is included in appendix A. The first observation was that the crack growth rate was very significantly reduced: 2.1 x 10^{-4} cm/h in average for the complete test

versus 10^{-3} for sample 617-CT-22 tested at a K of 49.5 MPa$\sqrt{m}$. Figure 31 shows a plot of the crack length versus time. After 450 hours of static loading, the crack length still measures less than 1.47 cm, which was considerably less in comparison to the tests conducted at a higher K. However, as previously, the plot is curving with time, which corresponds to an increasing crack growth rate with time. Although the curvature is less pronounced, we cannot, as it was the case at the higher stress intensity factor, define a unique set of crack growth rate behavior for each environment. The change from 1000 ppm to argon does not lead to any change in the general shape of the curve: neither a jump in crack length nor a slowing down of the crack growth rate is observed.

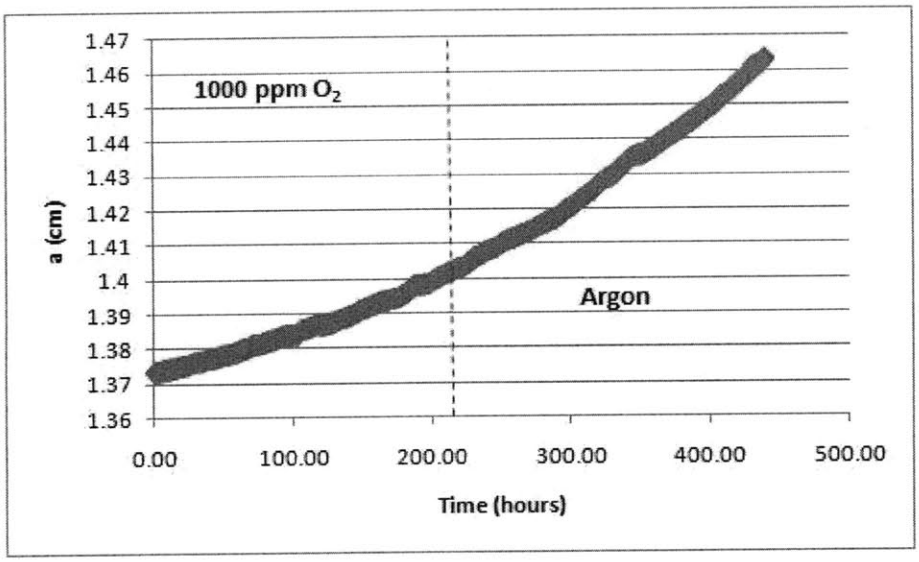

Figure 31. Plot of the crack length versus time for sample 617-CT-29 (K = 35 ksi$\sqrt{inch}$)

These results show the influence of the applied load on the crack propagation. At lower values of stress intensity factor we can make no statement as to the presence of an environmental effect for the time period of the tests. It appears that time-dependent processes are dominant and result in a crack growth rate slowly increasing with time.

4.2.4 Comparison with other alloys

The complicated behavior of alloy 617 suggested that a comparison with other alloys in the same conditions would be valuable. First, it was important to make sure the parabolic behavior previously obtained was not due to an error in the experimental set-up. For this, a similar test (T=650°C, K=49.45 MPa$\sqrt{m}$, varying oxygen partial pressures) was conducted

with alloy 908 which is known to be sensitive to stress corrosion cracking with significant crack growth rates during fatigue testing [50,51]. The results are displayed in Figure 32 and one immediately notices quite different behavior that of alloy 617. At constant K, constant temperature and constant environmental composition, the crack length versus time can be correctly described as independent of time, which means that the crack growth rate is constant.

Each environment is characterized by a typical crack growth rate and so the effect of the oxygen potential is displayed without any time-dependency. In the case of alloy 908, constant K tests seem well-suited to reveal the environmental effects on crack growth rate. During the second change, from argon to 50 vppm oxygen, the crack length encounters a big jump of about 1 millimeter in five hours. The steady state crack growth rate sets in after about 25 hours. Linear regression was used to determine the crack growth rates in each test step. The results are displayed in Table 8 for each environment. Although the crack grows slower in argon, the calculated crack growth rates are similar in both the 10 and 50 vppm environments. There might exist a threshold oxygen pressure below which the crack growth rate is limited by the diffusion of oxygen at the crack tip and not by the supply of it in the surrounding environment.

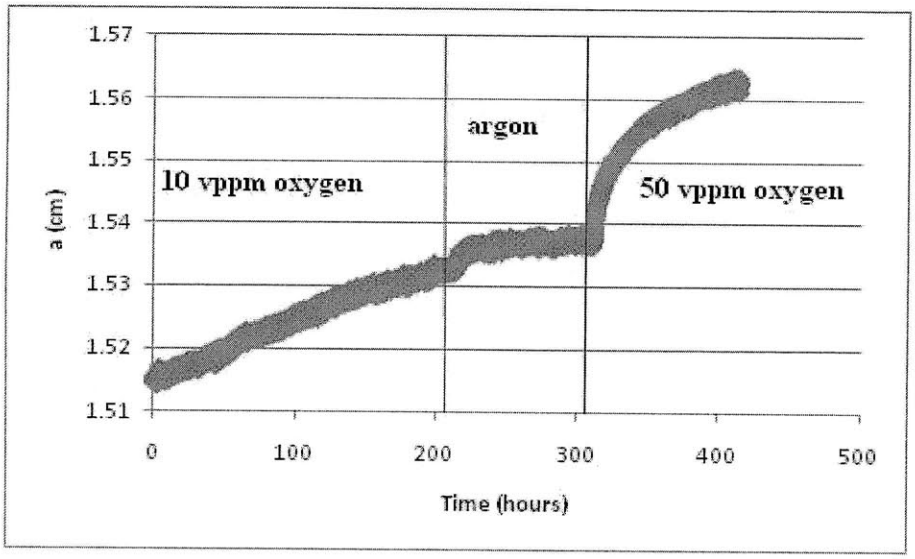

Figure 32. Crack length versus time (sample 908)

Environment	Oxygen Partial Pressure (atm)	Crack growth rate (m/s)	Crack growth rate (µm/hour)
10 vppm oxygen in argon	$4\ 10^{-5}$	$2.65\ 10^{-10}$	0.954
argon	$3\ 10^{-21}$	$4.41\ 10^{-11}$	0.159
50 vppm oxygen in argon	$8.7\ 10^{-4}$	$2.65\ 10^{-10}$	0.954

Table 8. Crack growth rates for alloy 908 in various environments

The crack growth values for the crack growth rates in alloy 908 are lower than the ones obtained for alloy 617. As an example, the steady state reached in argon (sample 617-CT-36) corresponds to a rate of 19 µm per hour which has to be compared with 0.159 µm per hour for alloy 908. That is a difference of more than two orders of magnitude for the same environment and temperature.

Another test (T = 650°C, K = 49.5 MPa$\sqrt{m}$) was conducted on alloy 230 (sample 230-CT-01) as it is Inconel 617's main contestant for high temperature applications. Haynes 230 has a yield strength similar to the one of 617 (cf. Table 3). However the results shown by the plot in Figure 33 are completely different from the one obtained for 617. Like 908, the plot for the crack length versus time is a straight line whose slope depends on the oxygen partial pressure. Two different pressures were tested ($4x10^{-5}$ atm and 10^{-7} atm) and the change from the first one to the other after 125 hours leads to a change of slope for the crack length versus time. No time-dependent effects are found. The crack growth rates in each environment have been determined by linear regression and displayed together with the correlation coefficient on the curve for each domain. By comparison with the values obtained for the other alloys, Haynes 230 (6 µm/h in 50 ppm environment) showed less resistance to crack propagation than Incoloy 908 (0.954 µm/h in 50 ppm environment). However the crack propagation rates in 230 (4-6 µm/h) are lower than the one obtained in alloy 617 when a steady state was reached in argon (19 µm/h). It will be very important to understand why these two alloys (617 and 230), which have similar strength properties, behave so differently in terms of crack propagation and environmental sensitivity. However Haynes 230 has the disadvantage to decrease in strength in carburizing environments because of tungsten carbides precipitation.

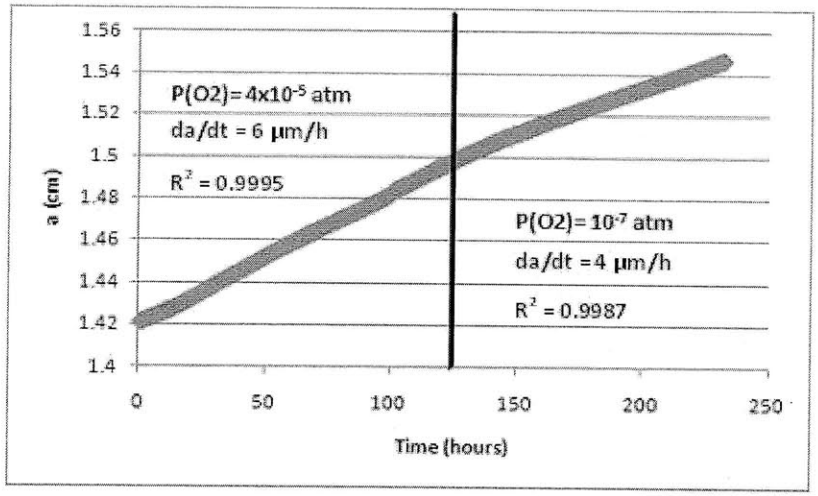

Figure 33. Crack length versus time for alloy 230. The oxygen partial pressure, the crack growth rate da/dt and the correlation coefficient R^2 for the linearization are displayed on the curve for each domain.

4.3 Fractography

After testing in the different environments, the samples were characterized by optical and scanning electron microscopy to determine the features associated with the observed behavior. Both the surface (plane LT-RD) and the fracture lips (plane ST-RD) have been investigated.

4.3.1 Mode of failure

The sample 617-CT-22 that failed after exposure to both argon and 10 vppm oxygen environments was analyzed by SEM in the plane ST-RD to determine the mode of crack propagation (transgranular, intergranular or mixed). The orientations are identified in Figure 19. Figures 34-36 show the results of the SEM analysis. The transition between the fatigue steps and the static loading period is clearly visible in Figure 34 where the mode of crack propagation shifts from transgranular to intergranular in argon environment. However no clear demarcation is seen for the change of environment, from argon to 10 ppm oxygen. This behavior argues that the role of the environment is minor and the crack propagation is essentially governed by mechanical processes. Figure 35 is a higher magnification fractograph inside the intergranular zone which shows wedge cracks distributed around the grains and propagating in directions different from the one of the main crack.

The transition from the transgranular mode to the intergranular one is also visible by surface observation in the plane LT-RD, shown in Figure 36. During the fatigue steps, the crack propagation is essentially straight whereas it becomes intergranular and somewhat

branched as soon as the load is maintained static. In the static mode, the crack path is intergranular regardless of the environment surrounding the sample.

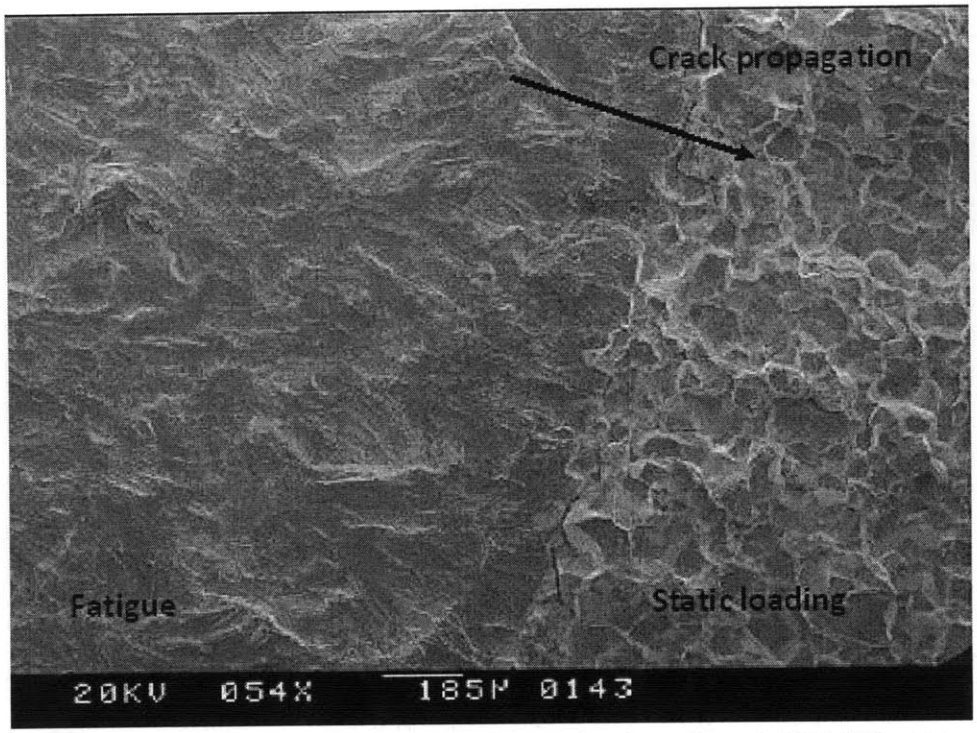

Figure 34. Scanning electron micrograph of the fractured surface of sample 617-CT-22 which demonstrates a clear interface between transgranular and intergranular failure

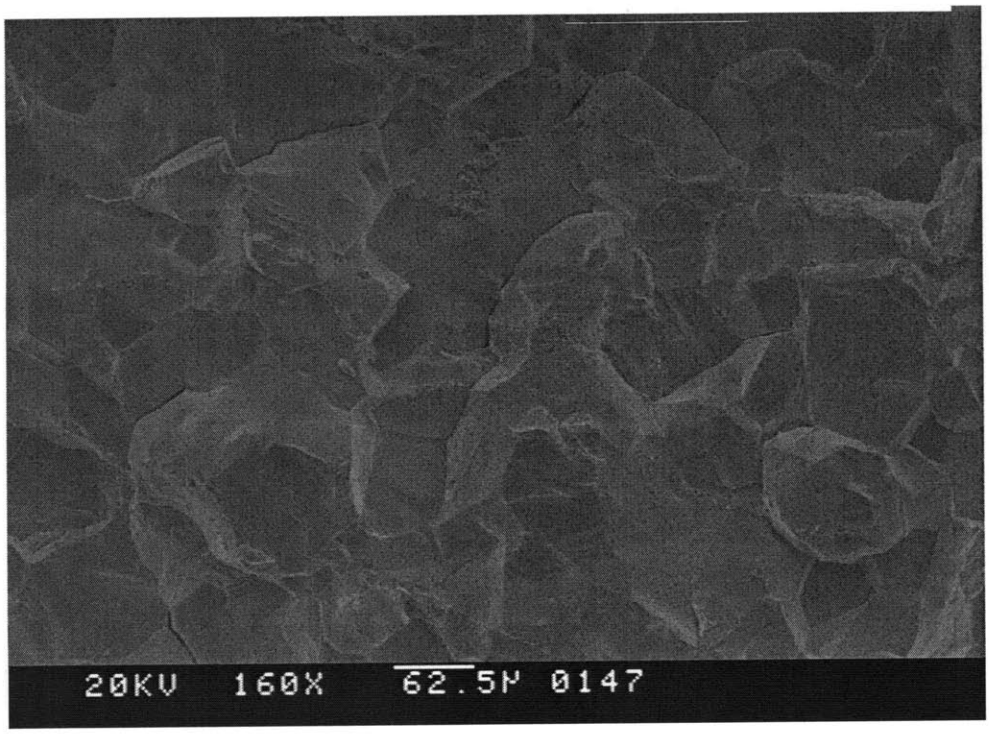

Figure 35. View of the intergranular fracture surface at higher magnification (160x)

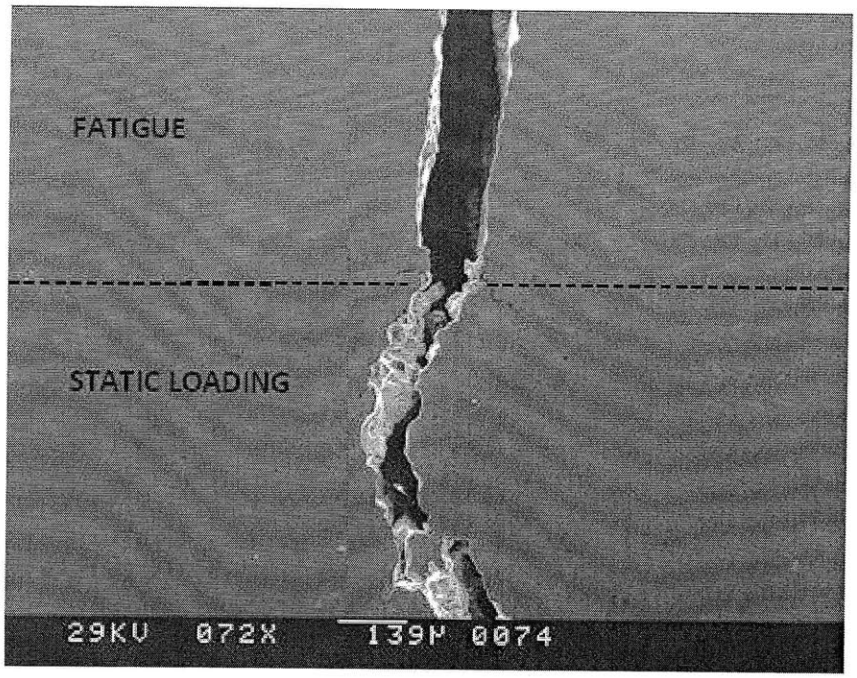

Figure 36. Scanning electron micrograph showing the shift from a straight fracture to a winding crack (The sample has been polished before observation with the SEM).

4.3.2 Crack morphology

Of particular interest is the fact that the damage is not limited to a unique main crack. Instead, a large area, both along the crack and ahead of the crack tip, is affected. A large number of short secondary cracks and isolated grain boundary cracking is observed. Figure 37 shows the region ahead and adjacent to the crack tip of sample 617-CT-36, with a large zone including a multitude of different cracking features. This crack tip has only been exposed to ultra-high purity argon which demonstrates that these features do not result from the interaction with the oxygen from the environment. Figure 38 displays the secondary cracks that are found to be aligned with the main crack (perpendicular to the applied load axis) in sample 617-CT-35. This one has been exposed to different environments, the final environment being 50 vppm O_2. However, once again, no significant change in crack morphology, including the secondary cracking features, is observed.

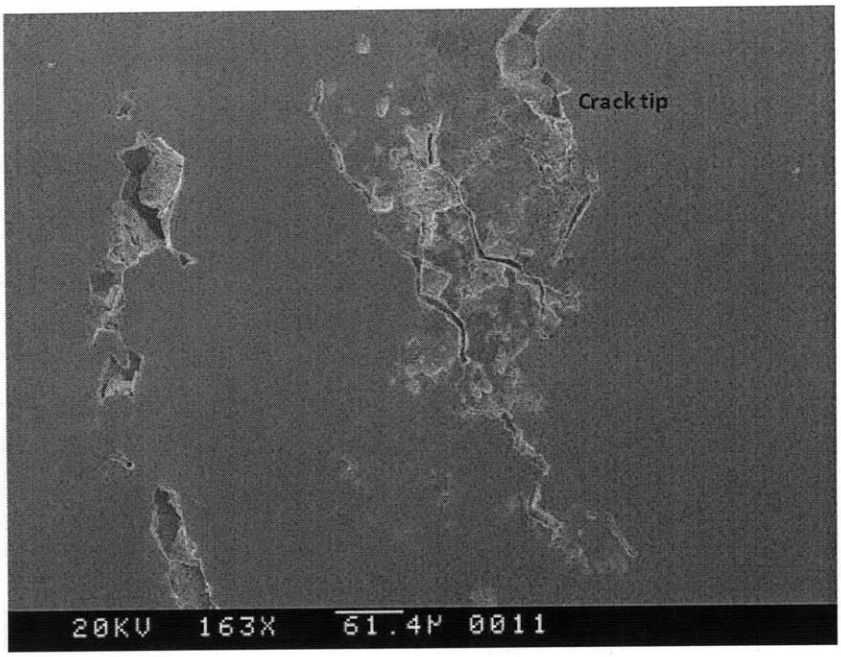

Figure 37. SEM micrograph showing the extent of the cracking affected zone ahead of the crack tip (sample 617-CT-36)

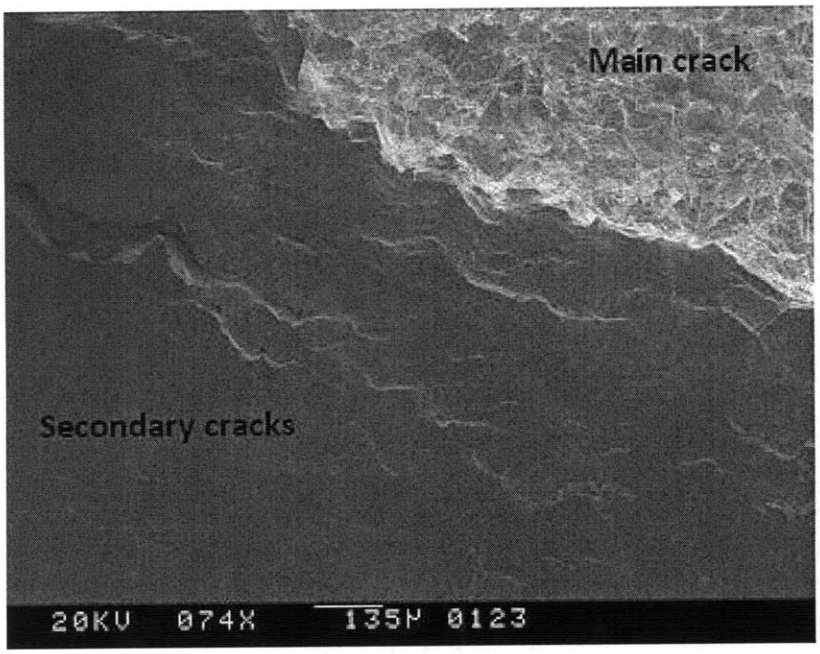

Figure 38. SEM micrograph showing secondary cracks aligned with the main crack (sample 617-CT-35)

To further facilitate crack observation, the sample surfaces were polished to 0.05 µm. Figure 39 shows a before and after surface polishing series for sample 617-CT-36. The

polishing process removed no more than 0.05 mm of material. In spite of this small material removal, the process resulted in an almost complete elimination of most of the surface cracks that are present on all of the sample surfaces. The side cracks do not extend through the thickness of the specimen but are limited to the surface. As shown in Figure 40, intergranular surface cracking ahead of the crack tip is also visible in sample 617-CT-29 which has been subjected to a lower K of 35 ksi$\sqrt{inch}$.

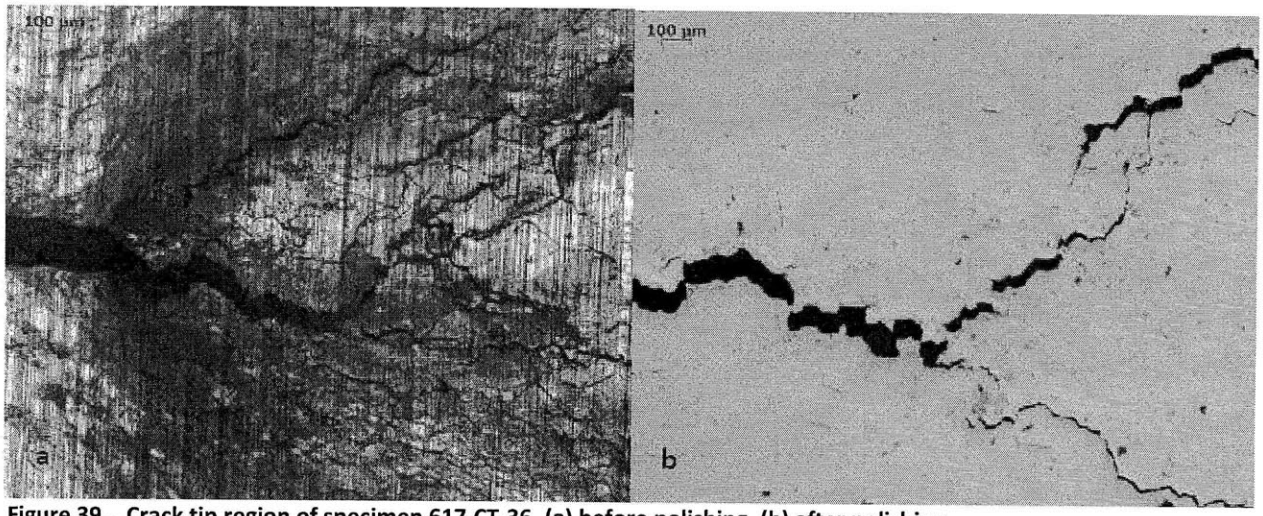

Figure 39. . Crack tip region of specimen 617-CT-36. (a) before polishing. (b) after polishing


Figure 40. Crack tip region of specimen 617-CT-29 showing secondary cracks ahead of the main one

These features are characteristic of the behavior of alloy 617 in the conditions of interest and do not appear on the alloy 908 sample. Concerning 908, the crack path is also found to be intergranular during the static loading phase but no secondary cracking around the main crack is observed. Figures 41-42 show the crack tip of sample 908. The crack path is intergranular but with no surface cracking evident. Figure 41 shows an SEM micrograph of the surface and further illustrates the intergranular crack path.

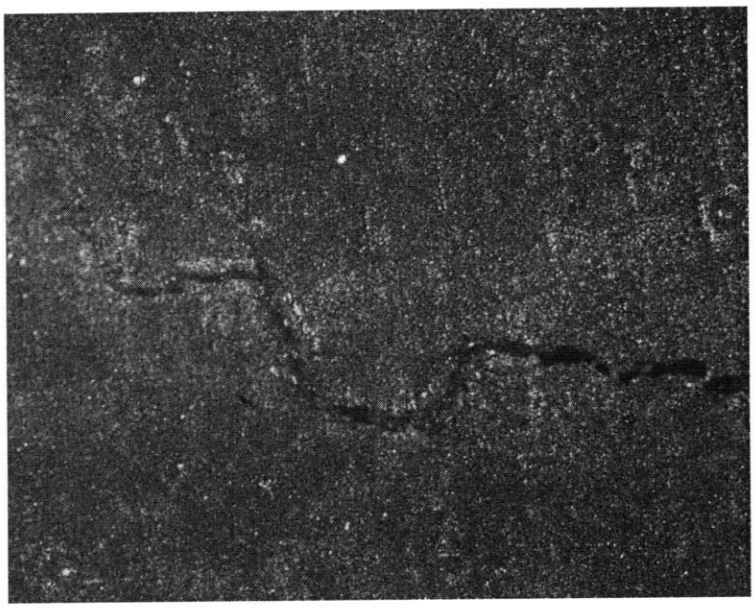

Figure 41. Optical micrograph showing the crack path on sample 908 surface

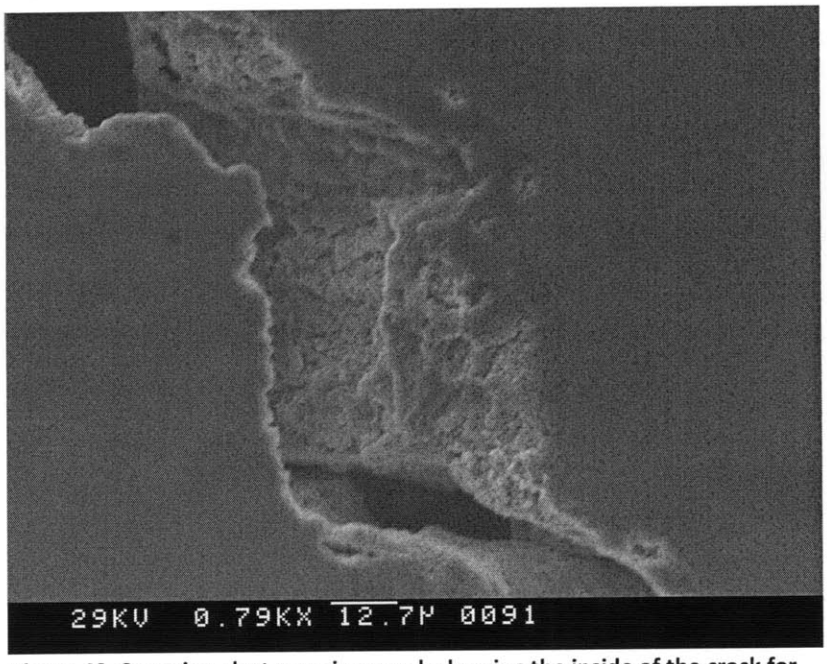

Figure 42. Scanning electron micrograph showing the inside of the crack for the 908 sample exposed to 10 vppm oxygen environment.

4.3.3 Wedge cracks and cavities

A scrupulous inspection of the crack's morphology in alloy 617 reveals that the crack is not uniform along its length. It is formed by a network of large cavities linked together by narrow cracks. The crack growth seems to be associated with cracking ahead of the tip, probably at a point of high stress concentration, such as grain boundary or second-phase particle. It seems that the crack has grown by linking those cavities together to form a continuous path, as shown in Figure 43 at two different magnifications. If we consider the crack morphology visible on Figure 43 a, two different phenomena are noticeable: in some places along the crack's path, the two surfaces on both sides of the crack perfectly match, in some others, they do not match. The matched areas correspond to simple crack propagation whereas the mis-matched ones probably result from the wedge cracking process.

All the features observed on the micrographs (sinuous path, surface cracking, cavities) associated with the non-linear plots for the crack length versus time suggest that creep is involved for crack growth in alloy 617 at 650°C and may overcome the environmental effects. To verify this hypothesis, it is necessary to conduct a creep test in which instead of the stress intensity factor K, the applied load P will be maintained constant. These results will be presented in Section 4.5.

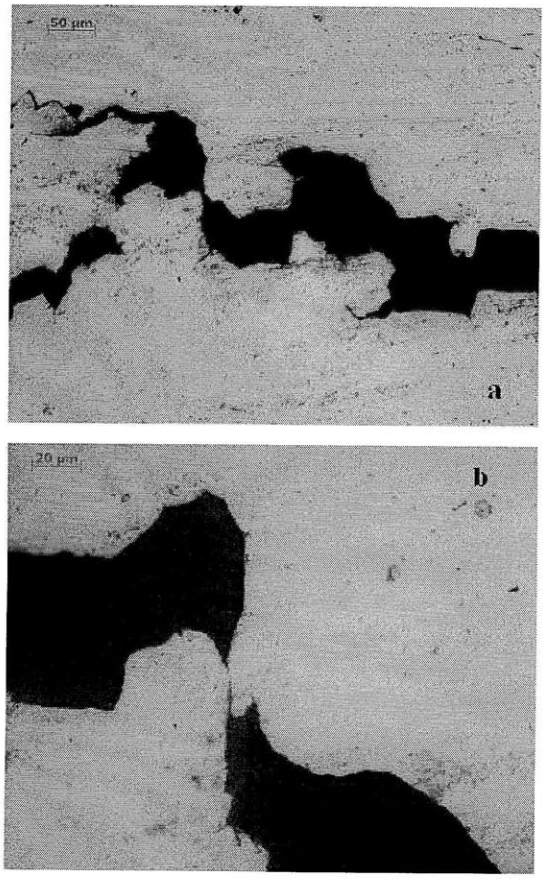

Figure 43. Optical micrographs showing the crack formed by linked voids in alloy 617 (a) at a magnification of 100x (b) at 200x

4.3.4 Precipitation

As was mentioned above, the all of the alloy 617 samples developed during testing surface features (cracks) that penetrated only several microns. To further explore the phenomena, one of the halves of fracture surface of sample 617-CT-22 was mounted and polished in the crack plane (the ST-RD plane in Figure 19) after polishing off (removing) the fracture surface from the intergranular crack propagation. Only enough material was taken away to remove the fracture surface and smooth the sample. The resulting micrograph can be seen in Figure 44. Of particular interest is the fact that a layer at the surface of the sample, approximately 40-50 μm in thickness, is visible and contains what appear to be precipitates. The precipitate layer might be related with the microcracks observed at the surface of the specimen and previously discussed.

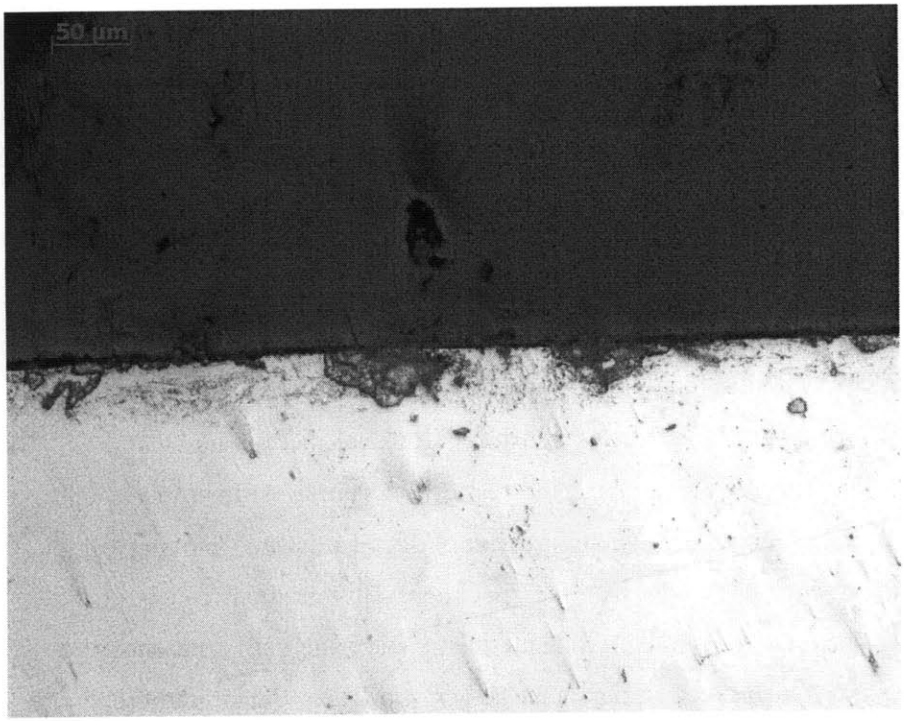

Figure 44. Optical micrograph showing the precipitation of particles under the surface in the lips of the crack (sample 617-CT-22)

Figure 45 shows an unetched micrograph of the side of a different specimen (plane LT-RD in Figure 19). The fracture surface is visible. The precipitates are visible, although the polishing process resulted in the removal of some of them. The concentration of precipitates

extends over a zone which corresponds to the fracture surface and the approximate width of the plastic zone on the surface.

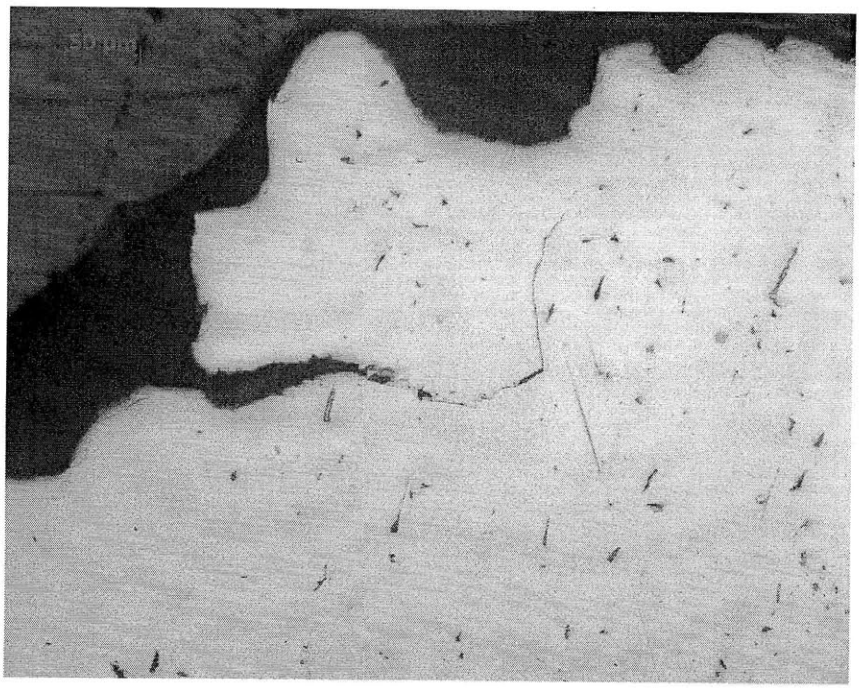

Figure 45. Optical micrograph of the sample's surface on one side of the crack, showing a high concentration of precipitates

By considering the whole sample, it is noticeable that the concentration of these precipitates is not uniform and that they concentrate along the fractured surface. However there is no clear demarcation between a zone with many precipitates and the rest of the sample without any. Figure 46 shows that the precipitates' concentration progressively decreases when moving away from the fractured surface towards the edges of the specimen. This gradient can be related to the fact that plasticity does not end suddenly outside the plastic zone but is present in the whole sample, especially concentrated around the crack tip. This precipitation phenomenon, limited to a small part of the specimen, might result from the interaction between plastic deformation and the environment.

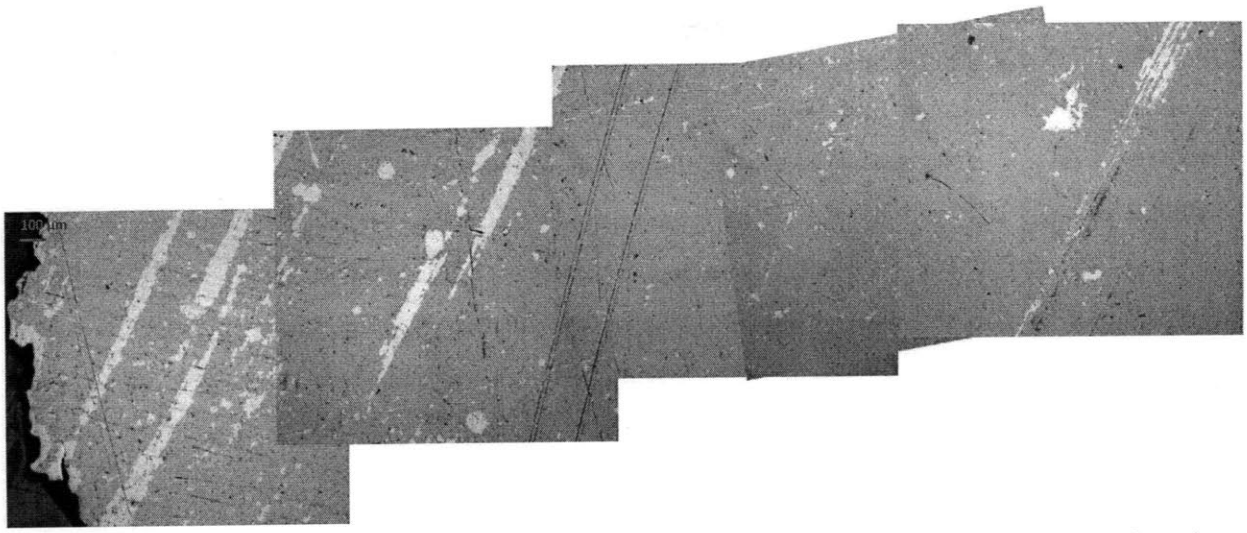

Figure 46. Optical micrograph showing the surface of a sample (plane LT-RD) with a gradient of precipitates from the left (fractured surface) to the right (edge of the sample).

Further characterization of these precipitates has been performed by EDX mapping and the results are displayed in Figure 47. A grain boundary has been made visible in the middle of the micrograph by polishing. The surface element map shows that the precipitates correspond to an enrichment in chromium and a depletion in nickel. No change in molybdenum and cobalt concentration was observed. The precipitates are thus chromium-rich and might be $M_{23}C_6$ that are known to precipitate along grain boundaries in the alloy 617.

.

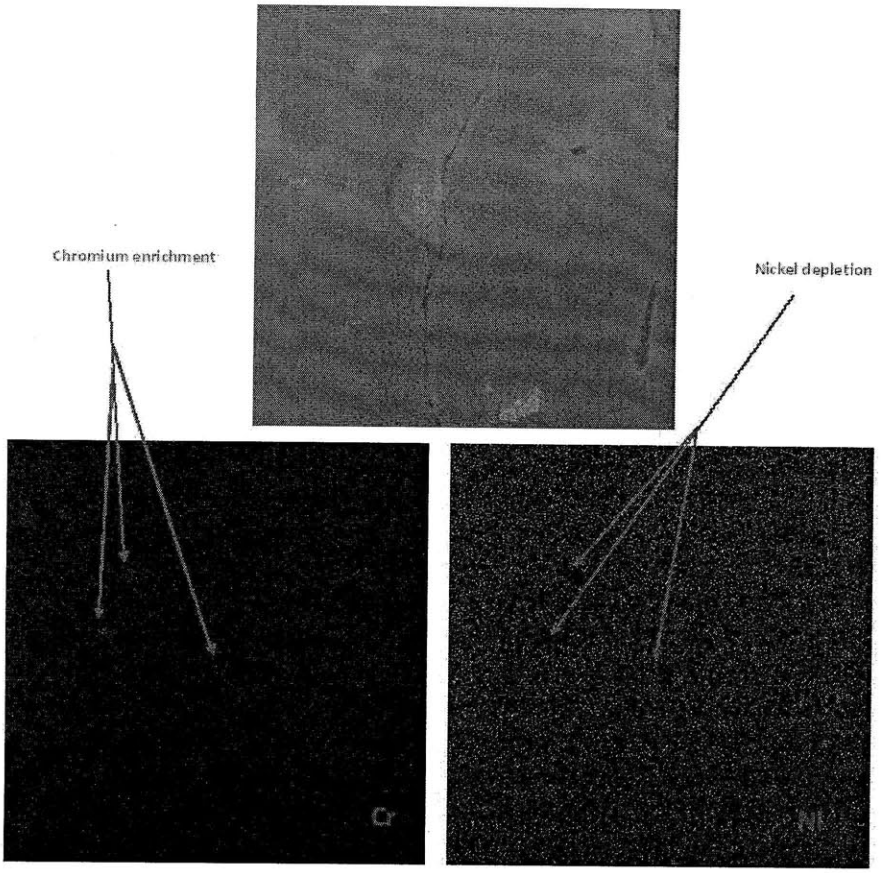

4.4 Corrosion testing

In order to investigate the effect of a low oxygen pressure environment on the oxide film formation of the superalloys of interest, independently of any applied load, a high-temperature corrosion experiment has been conducted. Three coupons, one for each alloy (617, 230, 908), were exposed to a 50 vppm O_2 environment for 500 hours in absence of any

Figure 47. EDX mapping showing identification of chromium-rich precipitates

load. Figure 48 is a photograph showing the coupons after exposure. They can easily be differentiated by their color: alloy 617 is rather drab whereas the two others were bright, red for 908 and olive green for 230. The red can easily be attributed to the iron oxide Fe_2O_3. And the olive green might be due to chromium oxide Cr_2O_3. It is also noticeable that the oxide forming on 908 is very brittle and gives rise to small shavings that detach from the sample. A cross-section of each material was analyzed by SEM to determine the extent of the damage and the morphology of the oxide layer. EDX analysis on these cross-sections allowed for an elemental mapping and so a first guess for the oxides forming. XRD analysis on the surface has been used to refine the previously obtained results by completely identifying the phases.

The results obtained by SEM, EDX and XRD will be presented separately for each alloy in the following sections.

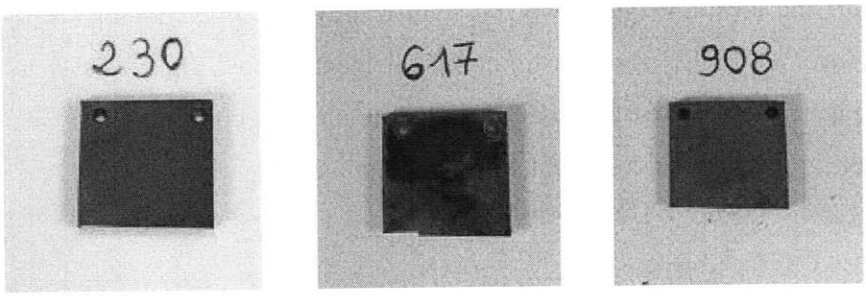

Figure 48. The three coupons at the end of the high-temperature corrosion experiment (500 h, 650°C, 50 ppm O2 in argon).

4.4.1 Alloy 617

The cross-section of the sample, shown in Figure 49, indicates that an 18 µm-thick layer at the surface is affected and structurally different from the rest of the sample. This layer can be divided into two sub-layers: first, a thin porous outer layer whose thickness is less than 3 µm and then, a dense inner layer which exhibits large grains with a diameter up to 20 µm. No precipitate is visible in the bulk material.

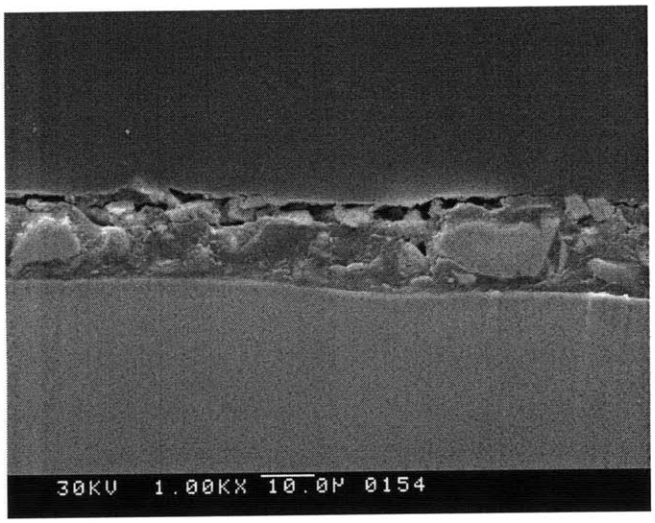

Figure 49. SEM micrograph showing a cross-section of alloy 617 after exposure to 650°C and 50 ppm oxygen environment for 500h

Elemental mapping was used to further characterize the layer chemistry. These results are shown in Figure 50. It reveals a segregation of aluminum in the affected layer as if aluminum had diffused from the bulk to the surface. A small amount of it can be seen in the

bulk, but it is essentially only detected in the outer layer, at the interface between the bulk material and the layer and around the large grains present in this layer. Nickel and chromium are the two main elements in the bulk and it seems that the large grains visible in the surface layer are also rich in chromium and nickel. Oxygen was not significantly detected, certainly due to the elemental resolution of the EDX which is limited to elements whose content is more than 0.1wt%. A zoom inside the affected layer, displayed in Figure 51, confirms that aluminum segregates around the grains and is not present within the grains.

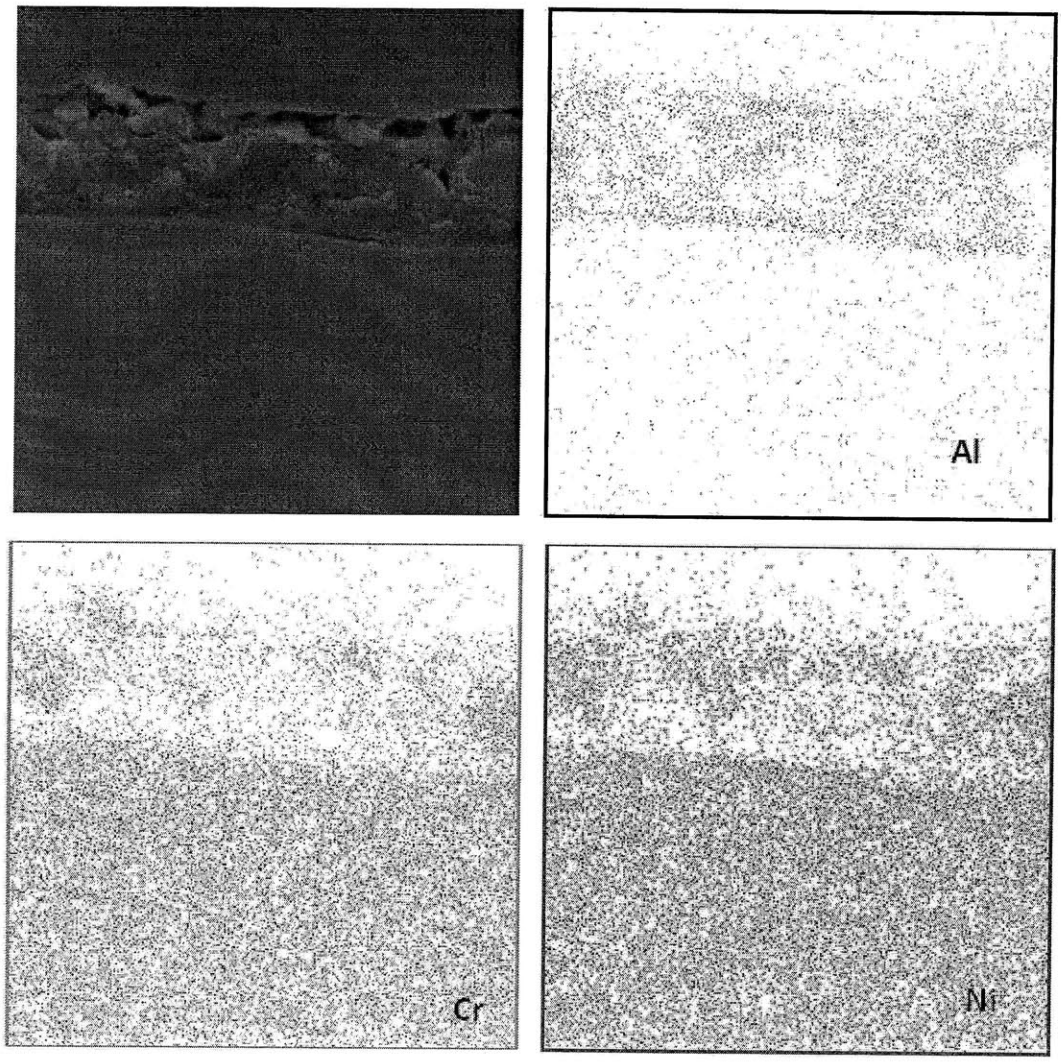

Figure 50. Compositional mapping images of the cross-section performed in the 617 alloy.

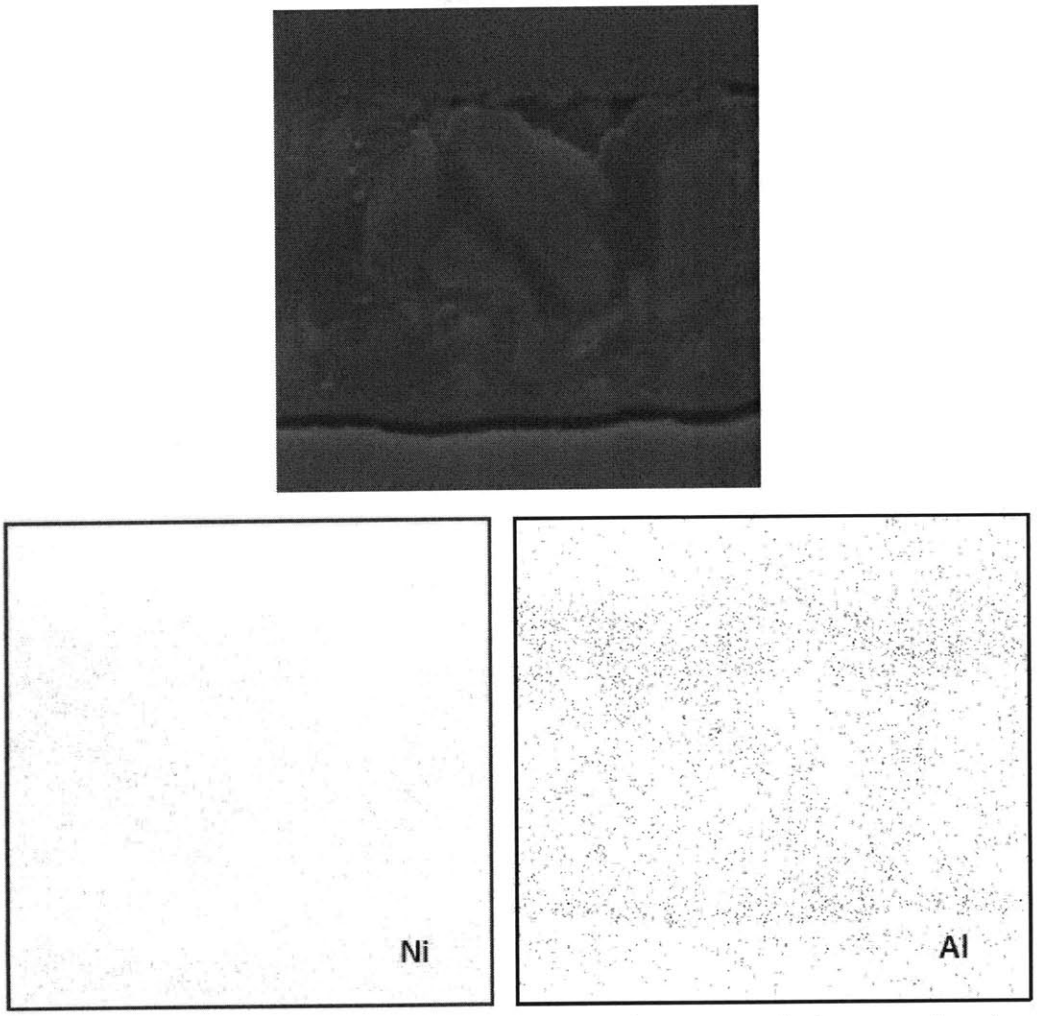

Figure 51. EDX compositional mapping taken inside the upper layer to magnify the segregation of aluminum

X-Ray Diffraction (XRD) measurements allow for detecting the main phases, in particular the ones we are interested in, which means the ones containing oxygen. Such analysis enables identification of the phases. EDX allows the identification of the elements that form oxide at the surface of the specimen. The XRD spectrum for alloy 617 is displayed in Figure 52 together with the labels identifying each peak.. Although alloy 617 has a complex chemistry involving many different elements, the spectrum obtained is quite simple. Among ten peaks detected, four could not be identified. Only two phases were found to correspond to the other ones: Mn_2TiO_4 and $Ti_{0.08}Cr_{0.17}Ni_{0.75}$. No aluminum oxide was detected.

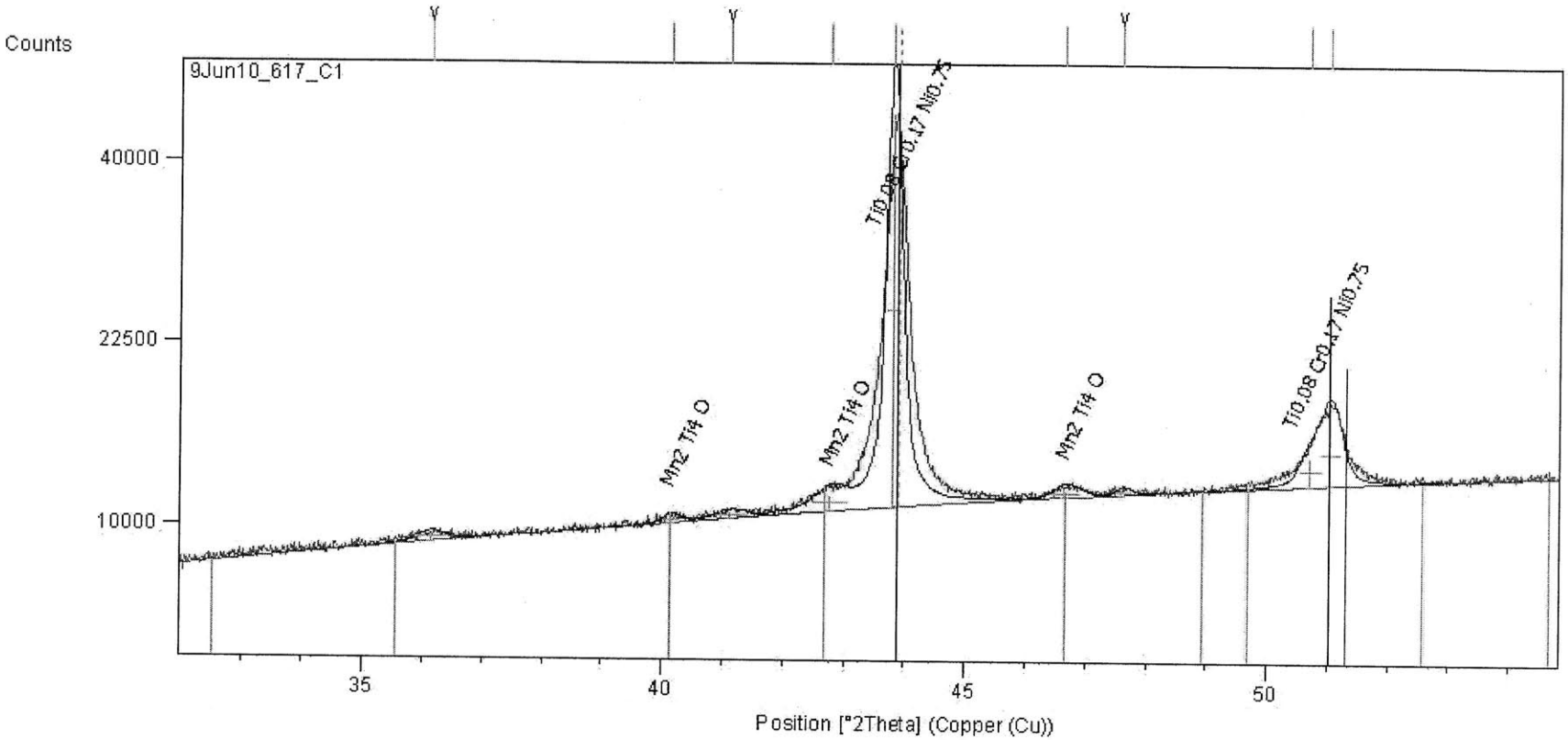

Figure 52. XRD spectrum with peak identification for alloy 617

Although obvious morphological transformations occur at the surface of alloy 617, no extended oxide formation takes place. It leads to a bare spectrum with a small amount of peaks. The characteristics of each peak (position, height, matched species, relative intensity, d-spacing) are given in appendix B.

4.4.2 Alloy 230

For alloy 230, the morphology of the oxide layer is completely different from that of alloy 617. On the cross-section shown in Figure 53, a large amount of porosity is visible in the top layer which corresponds to the first 30 μm of the film. The latter is constituted by elongated grains (around 20 μm in length) with void between them. The bulk material is not uniform as it contains precipitates with a mean diameter of 8 μm.

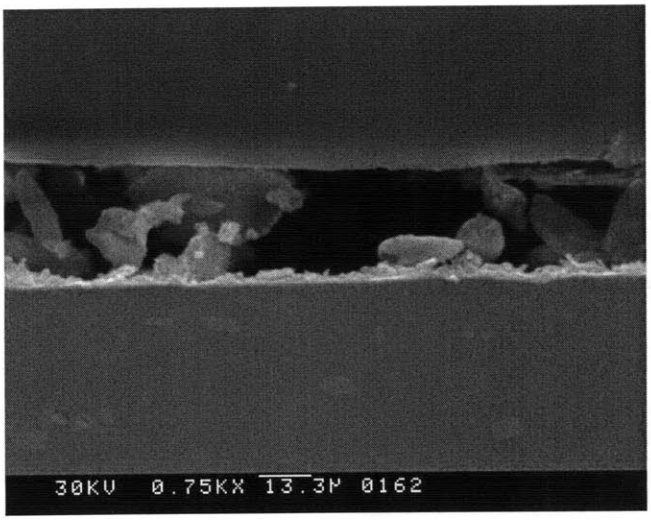

Figure 53. SEM micrograph showing a cross-section of alloy 230 after exposure to 650°C and 50 ppm oxygen environment for 500h

By EDX analysis, the results of which are shown in figure 54, the only element found in a significant proportion in the upper layer is chromium. That could be due to the formation of chromium oxide at the surface of the specimen. As expected, chromium and nickel are detected in the bulk material. No partitioning of aluminum is detected. Instead, its distribution is weak and uniform. An EDX analysis at higher magnification inside the bulk has been performed in order to identify the composition of the precipitates. The results presented by the mapping in Figure 54 clearly reveal tungsten carbides.

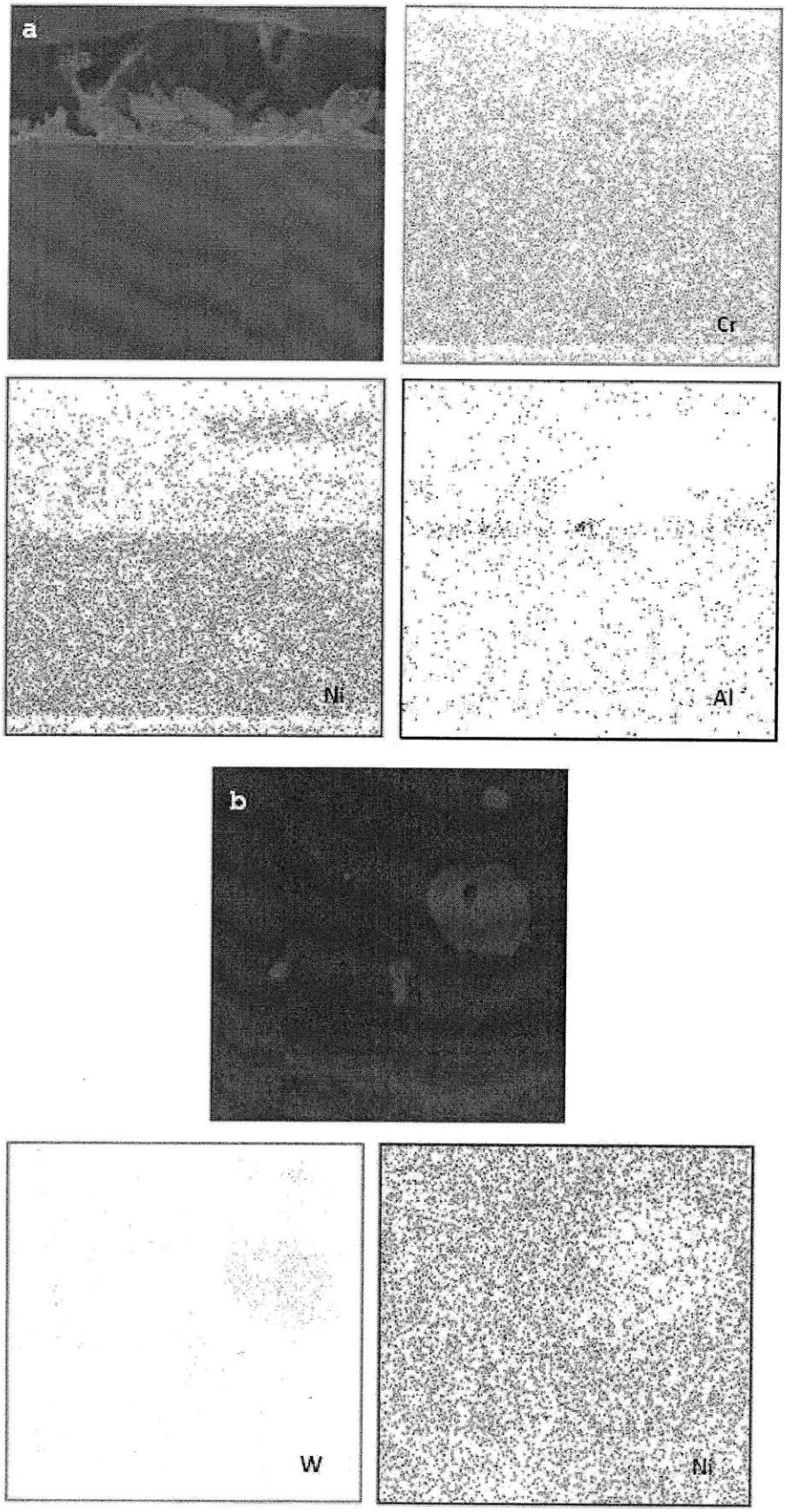

Figure 54. EDX compositional mapping (a) entire cross-section (b) zoom around carbide

At first sight, the XRD spectrum for alloy 230, shown in Figure 55, is much more complex than the one for alloy 617. Although three peaks have not been identified, seven different phases are found. Among them are nickel and tungsten, which means that the X-rays have penetrated inside the bulk. This is certainly due to the fact that the top layer is quite porous. Three different oxides are found to exist in this zone: Cr_2O_3, Cr_2MnO_4 and $Mn_{0.33}Fe_{0.67}O$. Between the porous outer layer and the bulk, a thin dense layer with small crystals is also present and could correspond to one of the three previously identified oxides. Appendix B displays all the details concerning alloy 230 spectrum, especially the peaks' position and height.

4.4.3 Alloy 908

The SEM cross-section for alloy 908 is shown in Figure 56. The oxidation zone extends over 35 μm but can be divided into three sub-layers each with a different character. The top five microns form a continuous compact layer. The following twenty microns are made of discontinuous elongated blocks separated by voids. This layer shows a tendency to detach from the bulk material which lies under it. The bulk suffers from internal oxidation with long inclusions of oxide covering its first fifteen microns. Strings of small particles are observed in the bulk under the internally oxidized zone. Among the three alloys, 908 seems to be the most affected by the environment. This is not a surprise since alloy 908 contains the lowest chromium concentration.

The results of EDX mapping are shown in Figure 57. Iron oxide is clearly identified to form at the surface. No difference in composition is found between the top dense layer and the following blocky grains. Iron is the main element for both of them. As expected by considering the nominal composition of the alloy, nickel, iron and chromium are the main elements in the bulk. With the internal oxidation zone, the situation is not so clear. For sure, it appears as an iron-depleted zone. Both nickel and chromium are present which suggests that an oxide based on these two elements could form. However the spatial resolution is not enough to see a gradient in composition between the inclusions and the surrounding material. XRD analysis is necessary to confirm these assumptions. Figure 58 shows the XRD spectrum. This time, all the peaks have been clearly identified.

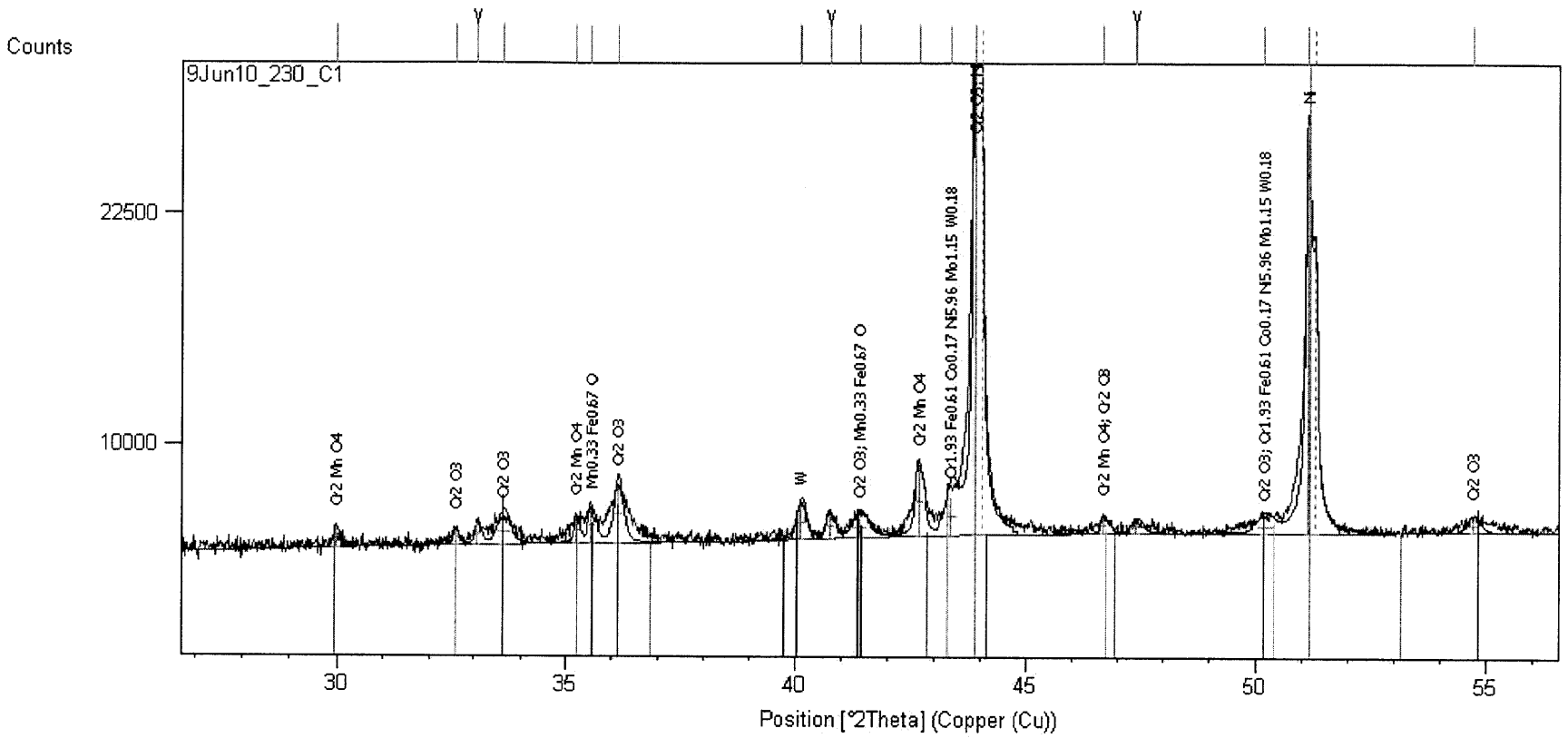

Figure 55. XRD spectrum with peak identification for alloy 230

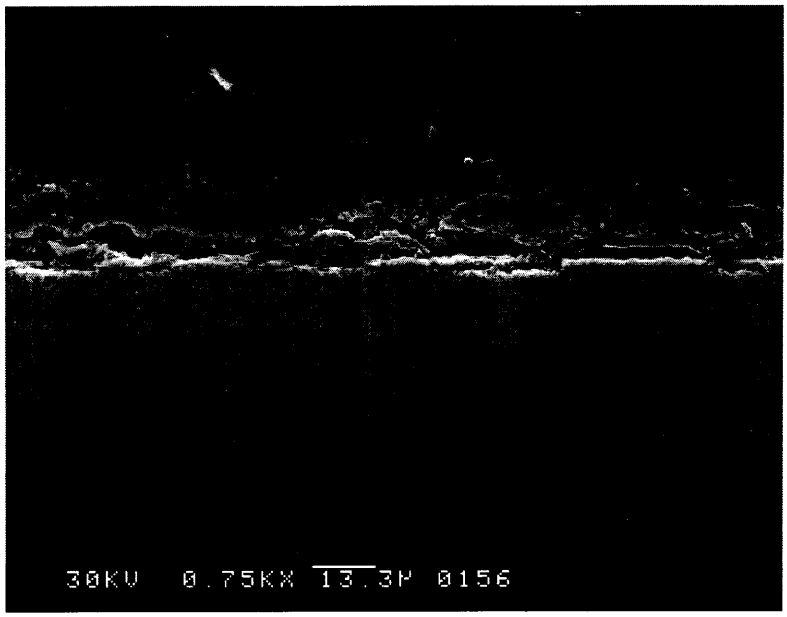

Figure 56. SEM micrograph showing a cross-section of alloy 908 after exposure to 650°C and 50 ppm oxygen environment for 500h

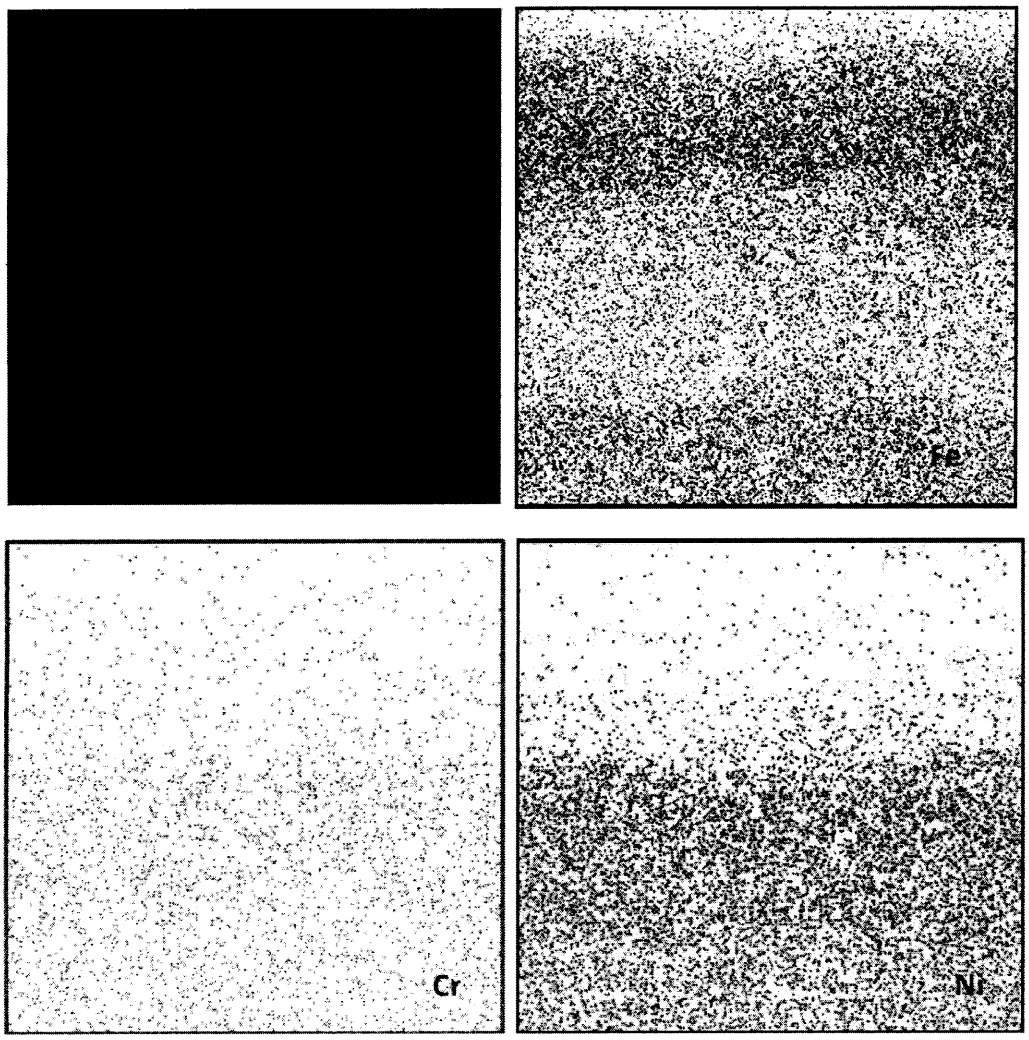

Figure 57. EDX compositional mapping for alloy 908 cross-section

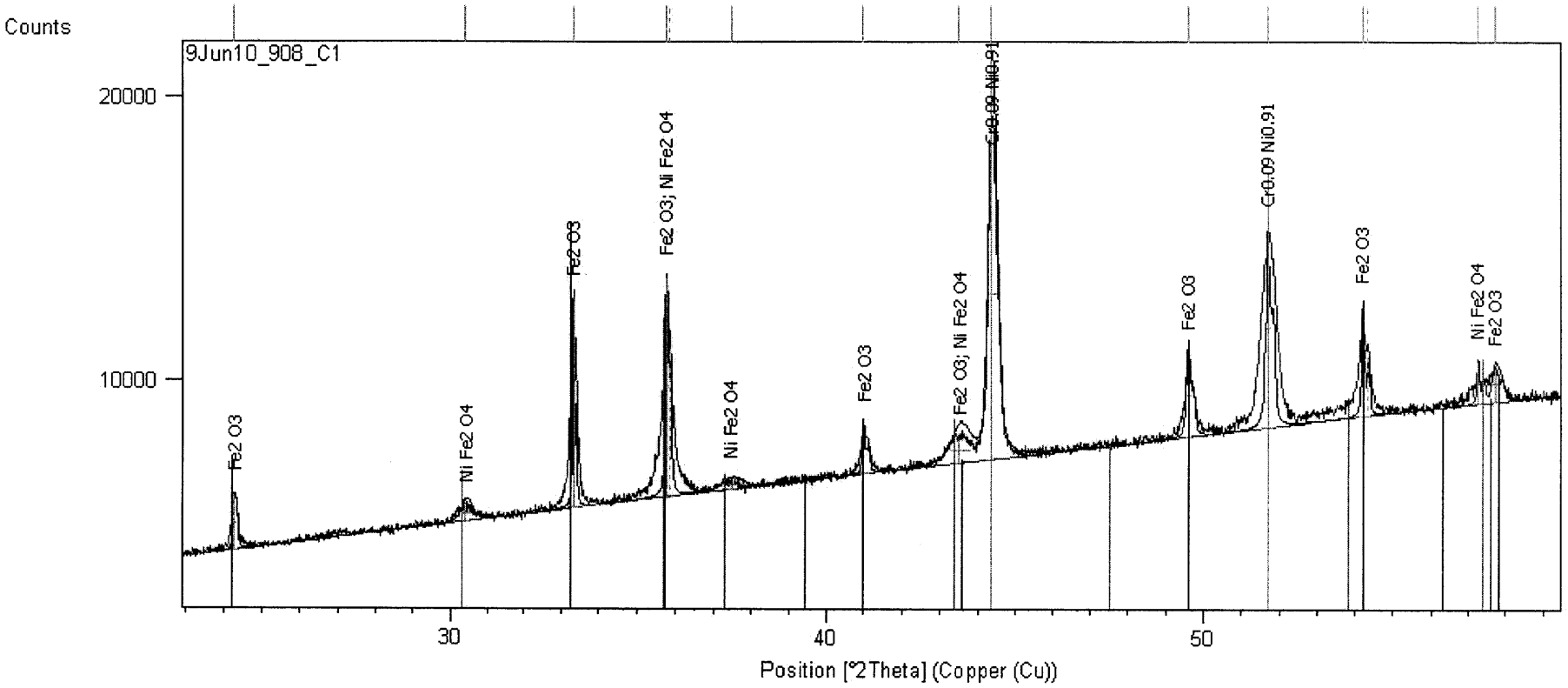

Figure 58. XRD spectrum with peak identification for alloy 908

The 908 spectrum is quite crowded and exhibits a large number of peaks, 19 in total. However all these peaks correspond to only three phases which are consequently clearly identified. Among them, $Cr_{0.09}Ni_{0.91}$ does not contain any oxygen and can be attributed to the bulk material, probably in the zone of internal oxidation where iron is absent. The two other phases contain iron and are oxides: as expected, Fe_2O_3 which is responsible for the red color of the surface, and the spinel $NiFe_2O_4$. We do not have enough information to assert whether or not one of these phases forms the inclusions visible in the matrix. Both of them may be part of the oxidized layer over the bulk. Neither $NiCr_2O_4$ nor Cr_2O_3 are found as it is the case when the alloy is exposed to fatigue loading in the same environment (650°C, 50 PPM oxygen in argon) [52]. In this reference, stress-corrosion-cracking has been attributed to inclusions of $NiCr_2O_4$ and Cr_2O_3 along the grain boundaries.

To conclude this section, it is important to recall the main results. Although alloys 908 and 230 exhibit extensive oxide formation, it seems not to be the case for alloy 617, as shown by the poor spectrum obtained by XRD-analysis. Usually Cr_2O_3 is known to produce a hermetic layer at the surface, which prevents further oxidation. It may be that it is present but that it is so thin that we cannot see it with the resolution of our instruments. As it is not extensively present in our conditions, we can deduce that the exchanges between the material and the surrounding environment are still possible. Oxygen penetration is not prevented, as well as diffusion of elements from the sample to the outside. The difference in chromium content between 617 and 230 is very small: 21.91 wt. % and 22.43 wt. % respectively. The difference in behavior may rather be explained by the presence of different other alloying elements, especially manganese. Its content is almost five times higher in alloy 230 than in alloy 617 (0.53wt. % versus 0.11 wt. %) and the formation of Cr_2MnO_4 and $Mn_{0.33}Fe_{0.67}O$ is found in alloy 230.

4.5 Creep investigation

4.5.1 Creep curve

A constant load creep test was conducted using a CT sample that was not precracked. The constant applied load, i.e. $P = 1.21\ 10^4$ N, had been calculated to correspond to a stress concentration factor of 45 ksi$\sqrt{}$inch at the notch. The environment was ultra-high purity argon ($P(O_2) = 10^{-22}$ atm).

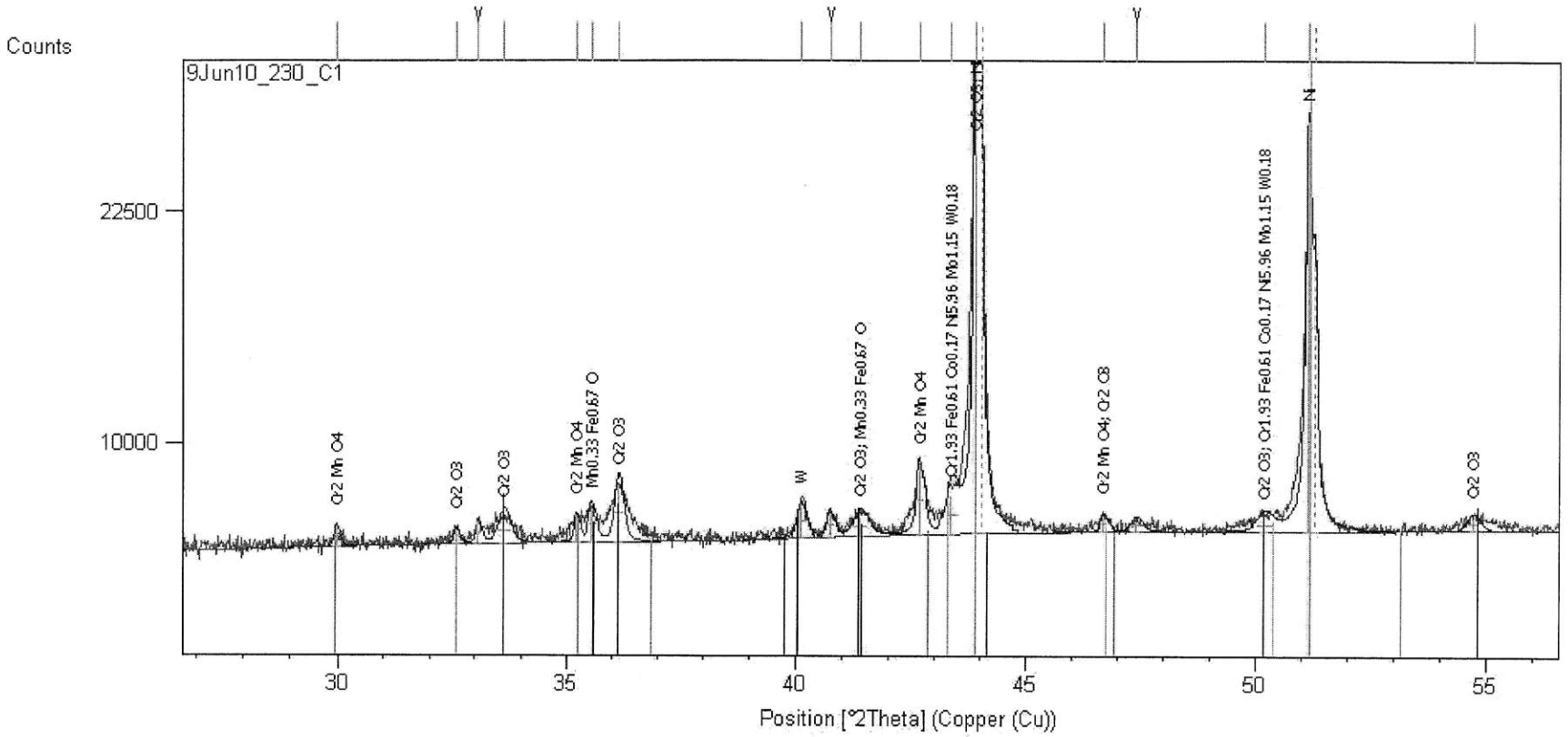

Figure 55. XRD spectrum with peak identification for alloy 230

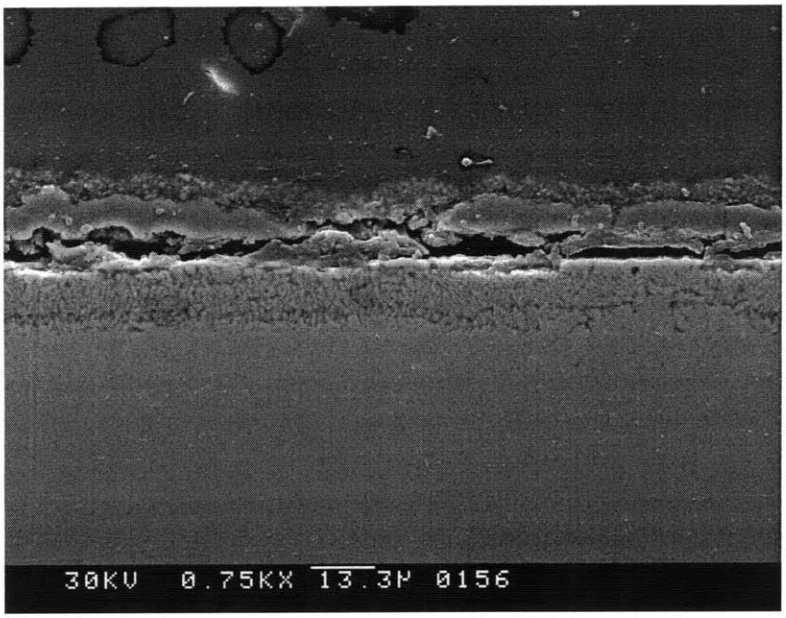

Figure 56. SEM micrograph showing a cross-section of alloy 908 after exposure to 650°C and 50 ppm oxygen environment for 500h

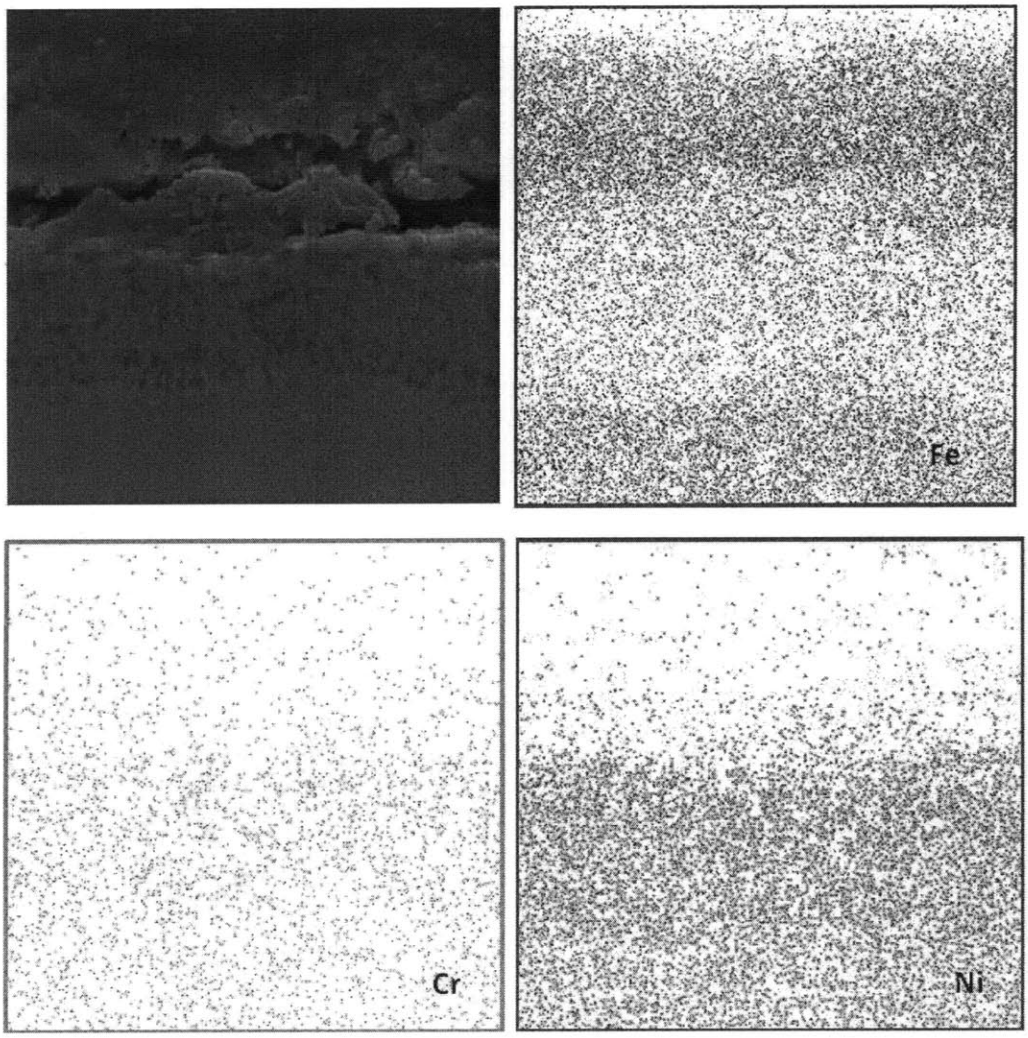

Figure 57. EDX compositional mapping for alloy 908 cross-section

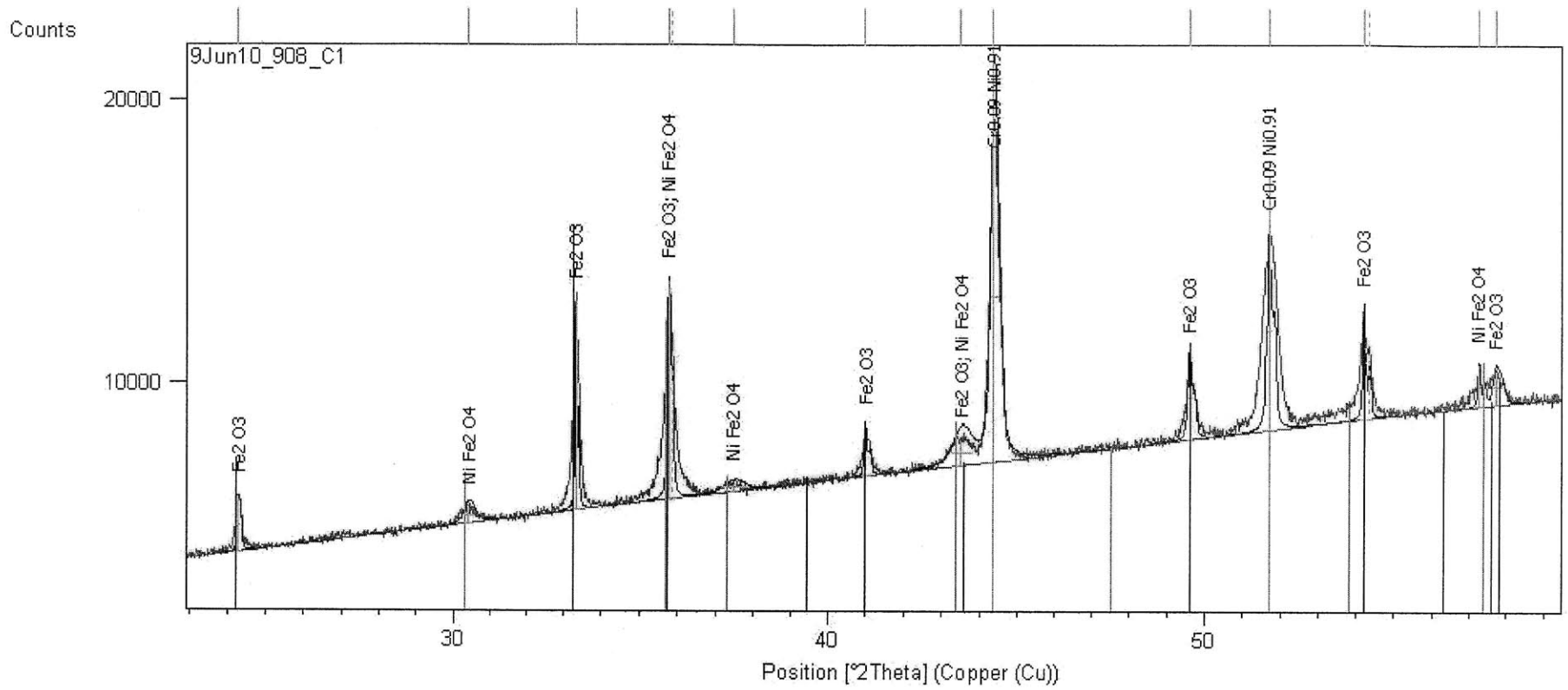

Figure 58. XRD spectrum with peak identification for alloy 908

The 908 spectrum is quite crowded and exhibits a large number of peaks, 19 in total. However all these peaks correspond to only three phases which are consequently clearly identified. Among them, $Cr_{0.09}Ni_{0.91}$ does not contain any oxygen and can be attributed to the bulk material, probably in the zone of internal oxidation where iron is absent. The two other phases contain iron and are oxides: as expected, Fe_2O_3 which is responsible for the red color of the surface, and the spinel $NiFe_2O_4$. We do not have enough information to assert whether or not one of these phases forms the inclusions visible in the matrix. Both of them may be part of the oxidized layer over the bulk. Neither $NiCr_2O_4$ nor Cr_2O_3 are found as it is the case when the alloy is exposed to fatigue loading in the same environment (650°C, 50 PPM oxygen in argon) [52]. In this reference, stress-corrosion-cracking has been attributed to inclusions of $NiCr_2O_4$ and Cr_2O_3 along the grain boundaries.

To conclude this section, it is important to recall the main results. Although alloys 908 and 230 exhibit extensive oxide formation, it seems not to be the case for alloy 617, as shown by the poor spectrum obtained by XRD-analysis. Usually Cr_2O_3 is known to produce a hermetic layer at the surface, which prevents further oxidation. It may be that it is present but that it is so thin that we cannot see it with the resolution of our instruments. As it is not extensively present in our conditions, we can deduce that the exchanges between the material and the surrounding environment are still possible. Oxygen penetration is not prevented, as well as diffusion of elements from the sample to the outside. The difference in chromium content between 617 and 230 is very small: 21.91 wt. % and 22.43 wt. % respectively. The difference in behavior may rather be explained by the presence of different other alloying elements, especially manganese. Its content is almost five times higher in alloy 230 than in alloy 617 (0.53wt. % versus 0.11 wt. %) and the formation of Cr_2MnO_4 and $Mn_{0.33}Fe_{0.67}O$ is found in alloy 230.

4.5 Creep investigation

4.5.1 Creep curve

A constant load creep test was conducted using a CT sample that was not precracked. The constant applied load, i.e. P = 1.21 10^4 N, had been calculated to correspond to a stress concentration factor of 45 ksi$\sqrt{}$inch at the notch. The environment was ultra-high purity argon ($P(O_2) = 10^{-22}$ atm).

As creep deformation rather than crack propagation is the concern here, the sample used had not been precracked. The applied stress was equal to $\sigma = P/S = P/B(W-a)$. With the values given in Figure 14 for W, a and B, this corresponds to a stress of 207.1 MPa. In the technical data provided by Special Metals for alloy 617, the yield strength is specified to be approximately 357 MPa after 100 hours at 650°C and 459MPa after 1000 hours at 650°C. The present experiment, which lasted 180 hours, approximately corresponds to a load of 0.58YS, where YS stands for the yield strength of alloy 617 and has been taken equal to its value after 100 hours at 650°C. The displacement was measured by mean of a dial gage with a sensibility of 1/1000 inch and has been recorded in Figure 59.

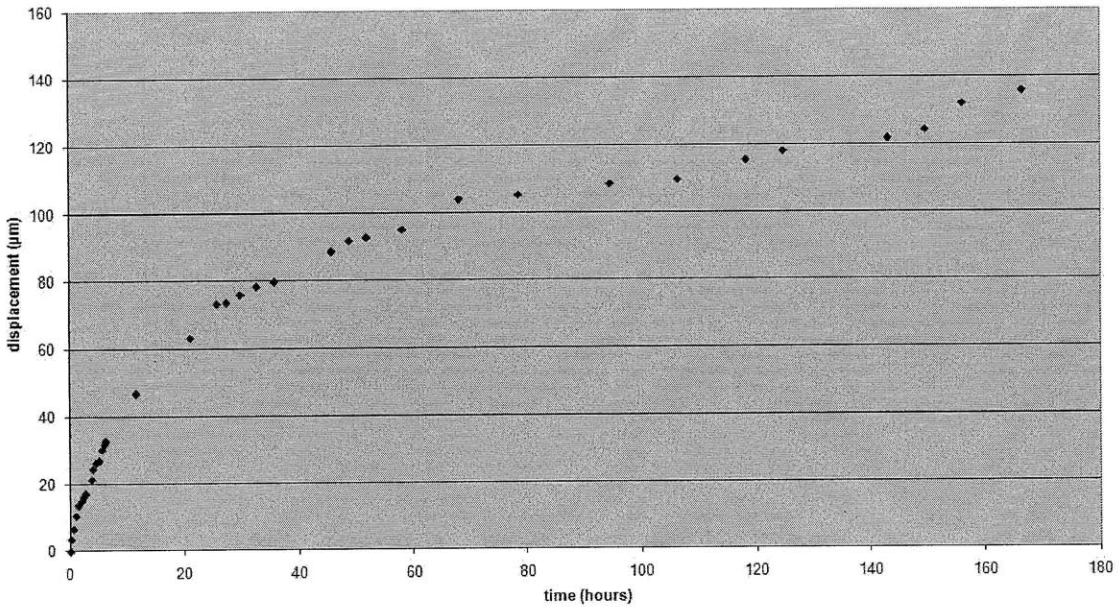

Figure 59. Plot of the displacement versus time in the creep experiment conducted at 650°C and an applied load of 1.21 10^4 N

The curve exhibits a near typical shape for a metal subjected to creep. A primary stage during which the displacement rate decreases with time is observed up to 46 hours. After, the curve can be considered as a quasi straight line, which corresponds to a constant deformation rate during the second stage of creep. A linear regression has been performed on the data from 46 hours to the end of the test. A deformation rate of 0.345 µm per hour is found, with a correlation coefficient of 0.973. If no creep at all would have occurred in the specimen, the curve should display a flat plateau after the first stage. These results are the proof that

deformation occurs due to the level of applied load. However this deformation is limited as the 140 μm obtained after 170 hours approximately correspond to the size of one grain.

4.5.2 Sample observation

After testing, the sample was observed by optical microscopy to determine which of the features previously identified during constant K testing are due to creep. Figure 60 shows the two places that are found to be affected by the applied load: the tip of the notch and the holes where the pins are inserted to maintain the sample in position inside the retort. The holes and the notch are both sites of high stress concentration. The features observed are thin and short cracks similar to the ones seen along the main crack and at the tip after constant K testing. At the notch these cracks are quasi perpendicular to the applied load whereas at the holes, they are inclined at 45° to the axis of the load. The aspect of the notch after polishing the sample to the 0.05 μm grit is displayed in Figure 61. All the deformation features have completely disappeared, which means that they don't extend through the thickness of the specimen but are instead limited to its surface.

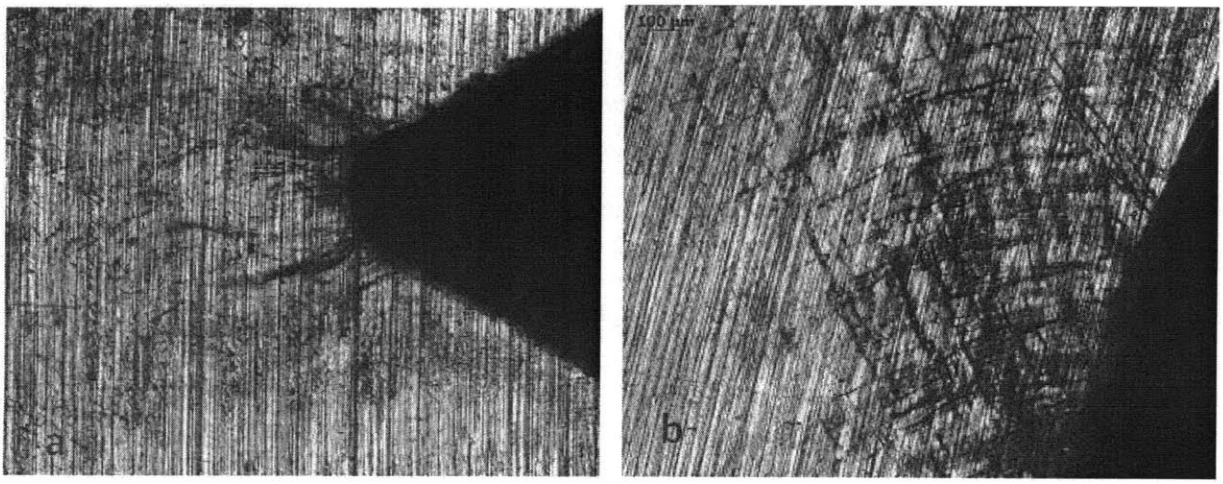

Figure 60. Deformation features observed after a creep test (a) at the tip of the notch (b) at the round holes

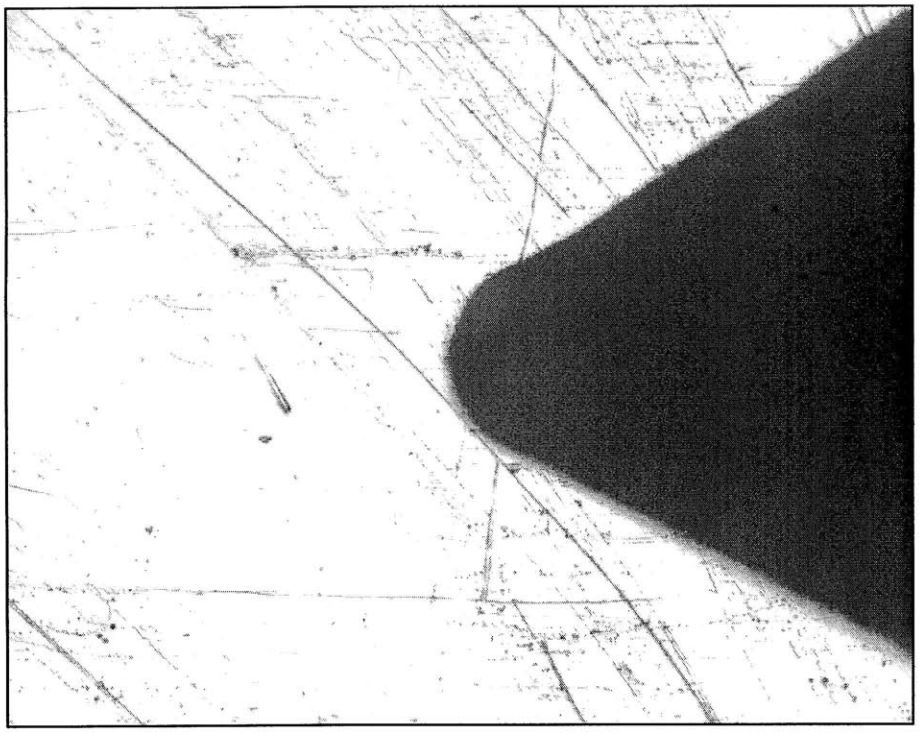

Figure 61. Aspect of the notch after creep experiment followed by polishing of the specimen to the 0.05 μm grit

After 170 hours testing at a sustained load at 650°C in argon environment, it is clear that alloy 617 is subjected to creep. However, the visible deformation does not extend to the whole specimen and is limited to the surface in regions of particularly high stress concentration. It is particularly surprising because there will be a plastic zone ahead of the notch completely through the sample. Plane stress conditions will apply to the surface and more plain strain-like in the interior. This means that there will be plastic deformation all along the notch front. Therefore, we are seeing here the same effect that we saw on the surface after the crack growth tests. These surface cracks are associated with the interaction between the environment and the plasticity associated due to stress and creep. However, only an experiment with a longer time exposure could reveal whether or not the damage zone observed here intensifies with time and leads to catastrophic deformation. We don't know how long it would take for the curve to reach the tertiary stage of creep and what amount of deformation would be accumulated before.

5. DISCUSSION

5.1 Crack growth rates

The main result of this study is characterized by the recurrent shape found for the curve representing the crack length versus time for alloy 617 at 650°C and subjected to an applied K of 49.45 MPa$\sqrt{m}$. Three different samples have been tested with varying environmental sequences: only argon for 617-CT-36, first argon and then 10 ppm oxygen for 617-CT-22, 10 ppm oxygen followed by argon and 50 ppm oxygen finally for 617-CT-35. However, the observed general behavior is always the same: it has a parabolic shape and displays an increasing crack growth rate with time. The precise shape of the curve does, however, depend on the environmental conditions. When the specimen was only exposed to argon, a steady state was reached after 350 hours. In 10 ppm oxygen environment, steady state could not be reached. It is also noticeable that while the character (shape) of the crack length vs. time may change with a change in environment, the degree of this change, if any, is a strong function of the stress intensity factor. This further demonstrates the complexity of the interaction between the stress, strain, strain rate and the environment, at least for alloy 617.

In light of these observations, constant K tests are not adequate to capture the effects of the environment on the crack growth rate in alloy 617 at 650°C. For this, we would ideally need a parameter for which each value would correspond to a unique crack growth rate. This crack growth rate would be a characteristic of the environment and would allow comparisons between environments. However, it is common to provide curves for the crack growth rate as a function of the stress intensity factor and it assumes the crack growth rate being constant at a constant stress intensity factor. It means that a steady state crack growth is observed and its value is taken to be characteristic of the conditions in which the test has been conducted (magnitude of the stress intensity factor, temperature and environmental composition). However, we should note that it may be that the test period may simply have been too short for a dynamic "steady state" to have been achieved at the high value of stress intensity factor. Recall that for some environments an approximate steady state was achieved and that at lower values of K the curvature of the crack length vs. time curve was much less pronounced. Given the results of this work, the approach chosen by Benz in his study [21] which led him to the conclusion that the crack growth rate decreases as the partial pressure of oxygen is increased needs to be reconsidered. As the data were not recorded for a long enough time in

each environment, he could not really realize that a divergence from the straight line behavior could occur and so, he neglected the influence of time. In fact, if the tests in this work had been terminated after 100 hours, the time dependency may also have been missed. In our case, it is because the tests correspond to long exposure periods that no unique value of the crack growth rate could be deduced.

The behavior of alloy 617 is strongly influenced by time-dependent processes at the temperature studied in this and the work of Benz. This makes the analysis more complicated than that for alloy 908 for example. For the latter, the crack length vs. time behavior is a constant. Even after long time exposure in the environment the crack growth rate is a constant which is only influenced by the environment's composition. The main difference in the mechanical properties of 908 and 617 can be seen by comparison of their yield strength and percentage elongation at room temperature. The ductility of alloy 908 is expressed in its low percentage of elongation: 12% vs. 50% for alloy 617. Moreover, the elastic behavior occurs up to a higher load for alloy 908 than 617 since it has a yield strength of 827 MPa at room temperature vs. 356 MPa for alloy 617. This comparison can be extended to the large number of nickel base alloys whose fracture mechanisms have been studied by Sadananda and Shahinian [25,26]. Table 9 brings together the mechanical data for the different nickel base alloys studied along with the mode of failure found by the authors during sustained load testing in air at various temperatures. Alloys 617 and 908 mechanical data at room temperature are added for comparison. The table clearly reflects the fact that there exists a competition between crack propagation and continuous deformation and that each alloy reacts differently for a given temperature. If the rate of deformation becomes too high (generally at high temperature), crack tip blunting and stress relaxation can occur more rapidly than accumulation and growth of damage such that any initial crack growth that occurs may be arrested completely.

Considering the value of the yield strength and the percentage elongation for alloy 617, one expects a behavior similar to Haynes 25, which means a temperature-dependent behavior and a permanent competition between the two effects (mechanical and chemical environments) described above. This indicates that the effects of creep deformation may be expected to interfere with crack growth leading to a non-constant rate. On the contrary, the high value for the yield strength of Incoloy 908 makes it closer to Inconel X-750 which displays a high crack growth rate at all temperatures and a significant susceptibility to the environment. In its case, there is a main crack growing continuously without being influenced

by extensive plastic flow. Although this comparison is based on very simple criteria such as yield strength and percentage elongation and does not take into account the compositional and microstructural (grain size, formation of precipitates) properties of the alloys, it gives a first explanation for the huge difference in behavior between 908 and 617.

Alloy	Yield strength (MPa)	% Elongation	Crack growth
Inconel 600	248	55	No crack propagation, blunting of the crack tip
Inconel 625	448	41	No crack growth at 870°C
Inconel X-750	650	14	Highest crack growth rate, significant effect of air environment
Hastelloy X	344	41	No crack propagation, blunting of the crack tip
Incoloy 800	186	53	Continuous deformation above 760°C
Haynes 25	468	55	Crack growth at 650 and 769°C, continuous deformation at 870°C
Nimonic PE-16	510	22	Lowest crack growth rate, no effect of air environment

Inconel 617	356	50	
Incoloy 908	827	12	

Table 9. Mechanical properties and crack growth behavior of some Ni base alloys. The results are from a study by Sadananda and Shahinian. Alloys 617 and 908 are added for comparison.

To go deeper into the understanding, one can recall that during a constant K test, the applied load is decreased to maintain the stress intensity factor at the desired level as the crack grows. The decrease in load during the test for sample 617-CT-22 has been plotted in Figure 62, where it goes from 1433 kips (= 6.37 10^6N) to 1012 kips (= 4.5 10^6N) in 354 hours. The temperature being held constant at 650°C, the governing parameter in term of creep is the decrease in load. It might lead to a progressive shift in the dominant process between rupture and deformation. At high load, the sample may experience continuous deformation that limits the effect of environment on crack propagation whereas, when the load is decreased, damage accumulation with very limited plastic flow may lead to a higher environmental effect on crack growth. Such a competition between the two previous phenomena could be responsible for the time-dependence in alloy 617.

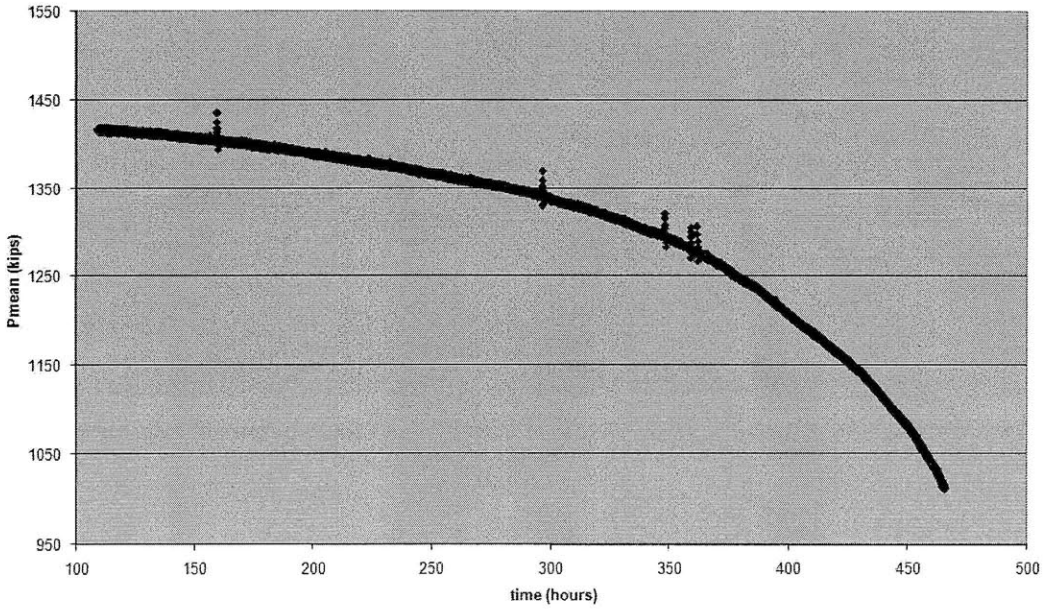

Figure 62. Decrease in applied load during a constant K testing (sample 617-CT-36)

The linear fracture mechanics theory is clearly insufficient for a description of the behavior of alloy 617, and a parameter which includes time effects seems to be necessary. Concerning nickel base superalloys, several studies [53-56] have been conducted to determine which parameter best correlates the crack growth rate. For this, sustained load tests have been used, the crack length recorded, the crack growth rate calculated on adequate time intervals and a value of the parameter of interest also calculated using the formula provided for the compact specimen. Thanks to this procedure, a plot for the crack growth rate da/dt versus the chosen parameter is obtained. For a parameter to be considered as valid, the scatter of the data points must be in a limited range around a straight line. No universal parameter is found to work for any alloy and the results are different from one alloy to the others. For example, the results obtained for Udimet 700 [54] are displayed in Figure 63 and clearly show a better correlation of the crack growth rate with the stress intensity factor K than with the C* integral parameter. The latter is related with the change of strain energy at the crack tip by the following formula:

$$C^* = -\frac{1}{B}\left(\frac{\dot{dU}}{da}\right)_{\dot{\delta}}$$

where U is the strain energy, a the crack length, B the thickness of the sample and δ the crack tip opening displacement.

An expression for the compact tension specimen is also available [57] and allows calculating the values during a test:

$$C^* = \frac{n-1}{n+1}\frac{P\dot{V}_{ss}}{2BW(1-a/W)}$$

where $\dot{V_{ss}}$ is the steady state deflexion rate, P the applied load, B, a and W geometric parameters defined in Figure 14 and n the creep exponent of the material which has to be determined by previous creep experiments or found in the literature.

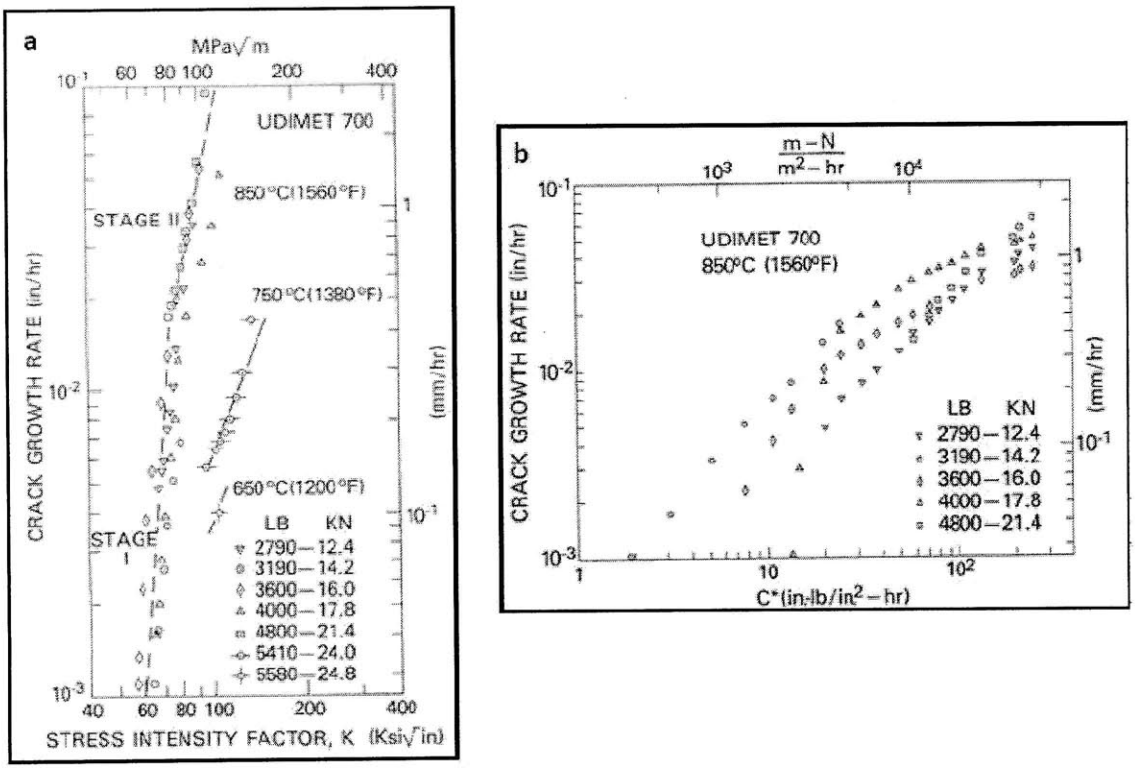

Figure 63. Crack growth rate (a) as a function of stress intensity factor K for various loads and temperatures (b) as a function of the C* integral for various loads at 850°C

However, for the parameter K to be valid, the authors are constrained to separate the values into two regimes, the low K one (stage I) and the high K one (stage II), each of them corresponding to a different slope for the correlation line. On the contrary, C* is found to better match the data obtained for alloy 718 [58].

Concerning alloy 617, the models based on the Paris law ($\frac{da}{dt} = CK^n$) are not satisfactory as they fail at taking into account the time dependent processes that play a major role in the present case. The nonlinear fracture mechanics parameter C* seems also not to be appropriate to describe the situation in our tests as its use is restricted to conditions of extensive secondary creep [59]. In our case, as shown in Figure 64, a zone affected by plastic deformation is clearly visible ahead of the crack tip. The size of this zone is about 8 mm for a crack length of about 10 mm and a remaining uncracked ligament of 18.5 mm. A cracked

body is said to be under extensive creep if the creep zone covers the entire ligament, which does not apply in our situation. However small-scale creep is also a non valid hypothesis as the deformed zone cannot be considered as small in comparison to the crack size and the remaining ligament size. We might be in an intermediate regime where both primary and secondary creep occurs simultaneously and no steady state is reached. This regime is described as transition creep in the literature [59]. Moreover, as the applied load is decreased with time, a final steady state can never settle.

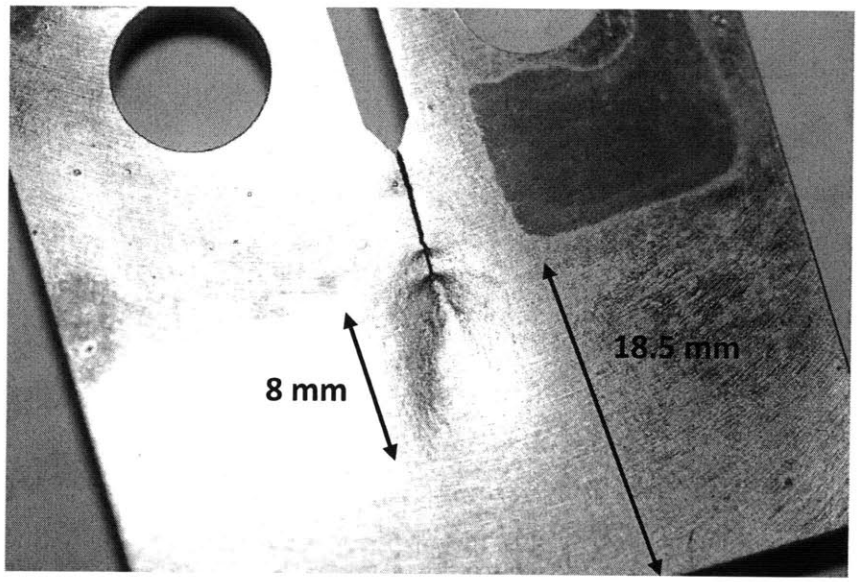

Figure 64. Photograph of the 617-CT-36 specimen after testing showing the sizes of the creep zone and the uncracked ligament

In order to detect the effects of the environment on the crack growth rate, and this, without the influence of the time-dependent deformation, a parameter varying with time has to be used. In the present case, the environmental effects are largely overcome by time-dependent processes at higher values of K. The test conducted on sample 617-CT-36 in ultra-high purity argon can be used as a reference state as the environment was free of any impurities ($P(O_2) = 10^{-22}$ atm). As shown in Figure 65, in absence of any environmental effects, the curve still exhibits this parabolic shape. Considering, the data points up to 350 hours, which means before the establishment of any steady state, the curve can be approached by an exponential function with the following equation:

$$\frac{da}{dt} = 6.10^{-5}\exp(0.0095t)$$

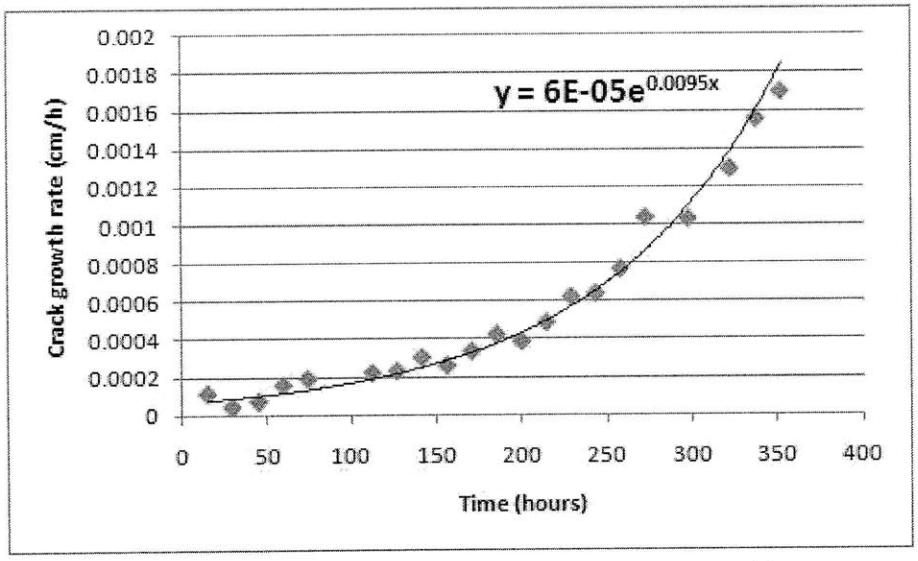

Figure 65. Regression for da/dt versus time for sample 617-CT-36 tested in argon environment

Considering this trend as a starting point, the first idea would be to change the parameter being maintained constant during a test. Instead of K, we could create a time dependent parameter proportional to $Kexp(0.0095t)$ where t is the time in hour. Such a parameter would correspond to a decrease in K when the crack grows. Getting rid of the time dependency by substracting the above equation to any other curve obtained by constant-K testing, is another possibility. It would allow underlining the environmental effects that were completely flatten by time-dependent processes. This idea is based on the assumption that the crack growth rate is made of two independent parts and can be expressed as the sum of them: $(da/dt)_t$ which varies with the time and which is related to the creep deformation, and $(da/dt)_e$ which is time-independent and is only affected by the oxygen potential in the environment. However, things are not so easy and as shown in Figure 66, creep and environmental effects are entangled and interact with each other. As a result, after having substracted the reference trend (figure 65) to the data points for sample 617-CT-22 tested first in argon and then in 10 ppm oxygen, the curved shape is still present in Figure 66. If creep and environment were completely independent, we would have obtained for the resulting da/dt versus time, an Heavyside function with two plateaux, one for each environment.

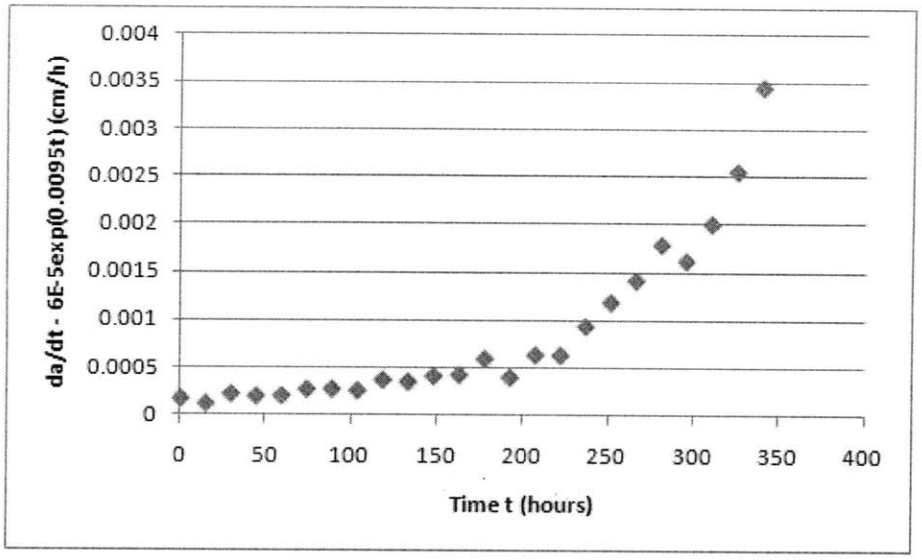

Figure 66. Corrected da/dt versus time to try to suppress the effects of the time dependency (sample 617-CT-22)

In fact, the effects of creep and environment cannot be separated. A more probable hypothesis would be to model the recorded behavior by an exponential law: $\frac{da}{dt} = Cexp(\alpha t)$ where C and α are two constants depending on both the applied K and the oxygen partial pressure. At constant K and temperature, it is also possible that the history of environment, which means the sequence of the different oxygen partial pressures, could influence these constants. Table 10 displays the values of C and α found for the three experiments conducted at a K of 49.45 MPa√m during this study. It would have been interesting but also time-consuming to limit each sample at a unique environment in order to really get the effect of the environment on these constants.

Sample	Environmental sequence	C (µm/h)	α (/hour)
617-CT-36	350 h in argon	0.6	0.0095
617-CT-22	170 h in argon + 185 h in 10 ppm O_2	1	0.0088
617-CT-35	340 h in 10 ppm oxygen + 247 h in argon + 175 h in 50 ppm oxygen	0.3	0.004

Table 10. Values of the constants C and α for the different tests conducted

5.2 Cracking features and potential mechanisms for crack growth

All the features that have been observed by optical and scanning electron microscopy reveal the complexity of the process responsible for crack growth in alloy 617 at 650°C and an applied K of 49.45MPa$\sqrt{m}$. On the contrary, crack propagation in alloy 908 is simple and follows the principles of stress corrosion cracking: intergranular propagation along embrittled boundaries due to oxygen penetration or oxide formation. As the main crack is accompanied by many other features (branching of secondary cracks, surface cracks along the main one, formation and linkage of cavities ahead of the crack tip) for alloy 617, the value provided by the DCPD is the sum of all these phenomena and so is inaccurate for the exact measure of the crack length. This is clearly the case for the sample 617-CT-36 exposed to argon. The final value calculated by DCPD is 10.41 mm whereas the length of the main crack measured by a dial gage mounted on an optical microscope is only 9.25 mm. In this case, it leads the DCPD to be off by 12%. Such a discrepancy could also be partially responsible for the curved shape of the crack length versus time plot. In fact, the growth of the main crack could be continuous and linear with a constant crack growth rate in a specific environment but the accumulation of the side damage could increase exponentially with the time of exposure, leading to an exponential function for the global behavior.

The different features observed have to be considered separately. First, the development of surface cracks in alloy 617 has also been observed by Yun and al. [60] during creep experiments at 800°C. They found that the fracture was not the result of a single crack but was initiated by statistically distributed formation and growth of pores at the grain boundaries, leading to eventual separation of the grains. They explained the growth of surface cracks by the combined effect of high temperature corrosion and creep strain. The surface cracks were found to appear after a certain incubation strain and to grow at a rate independent from the environment. This is in complete agreement with the shape of our curve which diverges from the straight line after long time exposure and seems not to be clearly affected by the oxygen concentration. They also reported the formation of internal pores whose linkage with the surface cracks leads to final rupture.

In fact, the crack displayed in alloy 617 have a particular aspect with large elongated wedge type cracks (50 μm large) linked by very thin cracks (less than one micron large), as shown in Figure 43. Such formations have also been observed in Nimonic 80, Inconel X-750 and Incoloy 800 [61]. The cavities are formed by aggregation of vacancies that become

mobile at elevated temperature and diffuse preferentially along grain boundaries. The cavity nucleation sites are diverse and usually located in regions of high local stress concentration at obstacles: impingement of a slip band on a grain boundary, grain boundary ledges, triple grain junctions, particles on grain boundaries normal to the applied stress [62]. The coalescence of cavities on grain boundary facets leads to grain-size microcracks. Figure 67 is a SEM micrograph obtained by fine polishing of the surface of sample 617-CT-36, up to 0.05 µm grit size. It displays an affected zone of about 200 µm on both sides of the crack in which microstructural changes occur, as shown in Figure 67a where the limits have been drawn. Characteristic cavities are visible inside this zone and they are probably formed by particles (precipitates, carbides) pulled out during the polishing phase. What is particularly noticeable is the fact that the cracks seem to emerge from these particles, as shown in Figure 67b at higher magnification. In other nickel-base superalloys, coarse $M_{23}C_6$-carbides have been identified as cavity nucleation sites, often in conjunction with a slip band impinging on the particle from the grain interior. By looking at the TTT diagram for alloy 617 displayed in figure 10, the test conditions (650°C up to 500 hours) correspond to a zone where $M_{23}C_6$-carbides may precipitate. This observation on the surface of the specimen can be related to the one of the edges of the fractured surface, shown in Figure 44. A precipitation phenomenon occurs in a 30 µm thick layer under the surface and these particles are revealed at the surface by polishing.

For nickel base alloys, it is well established [64] that embrittlement can also occur by formation of carbon-dioxide or carbon-monoxide bubbles by the reaction of oxygen from the environment with carbon contained in the metal. These bubbles, which are present in a typically 0.5 mm thick surface layer, lead to rapid grain boundary cavitation and to brittle failure.

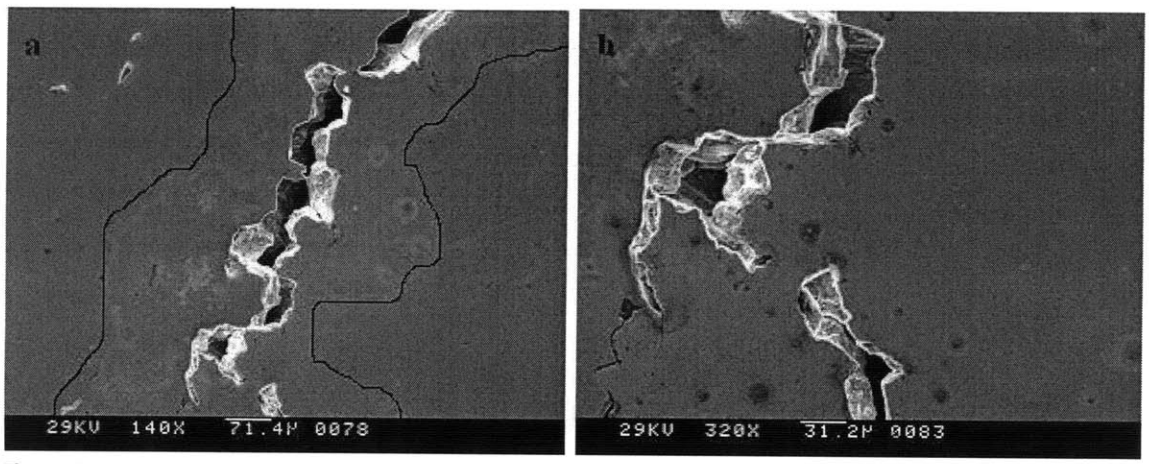

Figure 67. Scanning electron micrograph showing a) the zone around the crack where microstructural changes occur, the drawing of the limits have been added (b) the departure of cracks from second-phase particles

5.3 Corrosion results and correlation with crack propagation

Corrosion is a particularly important point to take into account in this study as it is a surface and time-dependent phenomenon and so, it might interact with both crack propagation and void formation. For alloy 617 exposed at 650°C for 500 hours, segregation of aluminum at the surface has been found by EDX analysis but no formation of oxide Al_2O_3 has been detected by XRD analysis at the resolution possible for our tests. The only oxide phase found was Mn_2Ti_4O and the small number of peaks in the XRD spectrum implied that no extensive oxide scale was formed. By referring to the literature [8, 12], the formation of a chromium oxide scale and internal inclusions of aluminum oxide could be expected. The development of chromium-rich oxide appears to protect the alloy against intensive corrosion processes. In our analysis, this is what seems to happen with alloy 230 that builds a significant chromium oxide layer at the top of the exposed specimen. However the experiments from the literature are usually conducted at a higher temperature than the one of interest in our case, usually at and above 900°C.

If we consider the thermodynamic data from an Ellingham diagram for the formation of chromium oxide at 650°C by the reaction: $\frac{4}{3}Cr + O_2 \longrightarrow \frac{2}{3}Cr_2O_3$, we obtain an equilibrium partial pressure of oxygen of 10^{-42} atm which is far below the actual pressure of 5.10^{-5} atm during the experiment. However this calculation assumes pure chromium with an activity of 1 which is certainly not the case in the alloy. A better approximation can be obtained by assuming that the initial activity of the element in the alloy equals the mole fraction of it and by using $P(O_2) = x(M)\exp\left(\frac{\Delta G^0}{RT}\right)$, where x(M) is the molar fraction of the metal in the alloy, ΔG^0 the standard free energy at 650°C, R the ideal gas constant and T the temperature in Kelvin. It leads to $1.7\ 10^{-34}$ atm, $1.28\ 10^{-56}$ atm and $3.2\ 10^{-19}$ atm for the equilibrium pressure for the formation of chromium oxide, aluminum oxide and nickel oxide respectively. By selecting a really low oxygen partial pressure, as it is the case in our argon environment (10^{-22} atm), the oxidation of nickel can be avoided. At 10^{-5} atm, the three previous oxides are susceptible to form. However this is only a thermodynamic point of view and the understanding of the real situation need to include the kinetics of the oxides formation.

The poor oxide formation that occurs on alloy 617 could be one of the causes for the other surface phenomena, especially the precipitation observed below the surface and the surface cracks growing on the top of the specimen. Exchanges between environment and metal may

be enhanced by the absence, or at least very thinness of any protective scale. Such exchanges could be responsible for a change in composition in the layer below the surface leading to precipitation and formation of surface cracks by diffusion of elements from the bulk to the surface or from the environment to the specimen. What is usually observed during oxidation of the alloy [7] is rather the depletion of grain boundary carbides, as well as matrix carbides. This decarburized zone is shown to become greater as the temperature and exposure time increase. By enhancing diffusion of the oxidizing agent and gaseous reaction products along the grain boundary, the application of tensile load enhances decarburization. Moreover, the authors associate the carbide depleted zone with various microstructural features also present in our observation, such as surface cracking along the grain boundary, voids below the surface and voids within the matrix. All these features are considered as detrimental for the creep resistance of the alloy.

6. CONCLUSION AND FUTURE WORK

This study has examined the behavior of Inconel 617 at 650°C in low oxygen pressure environments (from 10^{-22} to 10^{-3} atm for the oxygen partial pressure in argon), and especially the crack growth rate under static loading in these conditions. The high value chosen for the stress intensity factor (K=49.45 MPa$\sqrt{m}$) gave rise to complex behavior: whatever the oxygen potential, the plot for the crack length versus time displayed a recurrent shape with an increasing crack growth rate with time. Influence of the environment on the crack growth rate was observed in a given environment but this influence was greatly complicated by the presence of time dependent deformation. Because of this no unique crack growth rate could be defined as time-dependent processes took place. The only way to compare the different environments would require picking a time and measuring the instantaneous crack growth rate for that time in each environment. As the damages are cumulative, such a procedure cannot be followed with a unique sample and requires a different sample for each environment. Paris' law ($da/dt = CK^n$) is not suitable here contrarily to the case of alloy 908. The latter tested in the same conditions as 617 was sensitive to stress-corrosion-cracking and displayed a constant crack growth rate in a given environment. For alloy 617, maintaining the stress intensity factor K constant does not allow revealing the influence of the environment. In fact, choice of a characteristic parameter must include the time. An exponential law has been found to fit with the data for K equal to 45 ksi$\sqrt{inch}$ in the different environments: $da/dt = C\exp(\alpha t)$ where C and α are constants that might depend on the temperature, the environment and the magnitude of K. To really get the influence of these factors on the values for C and α, each sample has to be tested in a unique environment instead of a sequence of different successive environments, as it was the case in this investigation.

The curved shape of the plot for the crack length versus time has been attributed to the competition between crack propagation and continuous deformation in an environment which also has an influence. The conditions chosen for the temperature and the load led to an intermediate domain where creep and environmental damage coexist. Moreover these two phenomena could not be separated. The environmental effects were strongly influenced by mechanical and thermal effects. To really determine how creep is influenced by the environment, sustained load tests in varying oxygen partial pressures could be conducted and differences in the shape of the curve, if any, could be unequivocally attributed to the oxygen potential. Cracking features such as secondary cracks along the main one, intergranular

cracking ahead of the crack tip and cavities forming at grain boundaries were pieces of evidence supporting the existence of an extended zone of deformation around the crack. However, as found by a creep test conducted in argon, creep deformation is limited to a finite region of high stress concentration and does not extend in the whole sample. In fact, when a load is applied, creep deformation and fracture are two different ways to accommodate the stress that seemed to be simultaneously involved in the case of alloy 617. In order to accurately estimate the size of this affected zone, nano-indentation at the crack tip should be used. Trials to do so with micro-indentation have failed since the indents have to be well separated to each other in order for the deformation created by the first one not to influence the hardness determined by the next one. As the affected zone has a size in the micrometer range, the indents have to be in the nanometer range to capture a potential evolution in hardness.

Of particular interest was the fact that most of the features observed on the tested samples were limited to the surface and disappeared after a certain amount of polishing. This was the case of some cracks and precipitates only visible at the surface. The precipitates were identified as chromium rich $M_{23}C_6$ carbides and might be related to the surface cracks. Moreover the corrosion experiment exposing the samples for 500 hours in a 50 ppm oxygen environment revealed the absence of any extensive protective oxide scale on the surface of the sample. It could facilitate the exchanges between the alloy and its surroundings and so lead to precipitation and cracking at the surface by species entering or exiting the sample. Such phenomena could not occur in alloy 230 that was found to build up a consequent layer of chromium oxide, preventing further exchanges with the outside.

The results found in this study are particularly alarming for the use of 617 at 650°C and low-oxygen partial pressure under high applied stress. The fact that time-dependent processes occur without reaching any steady state is particularly worrying since this will greatly complicate the development of appropriate constitutive relationships that will allow proper design.

APPENDIX A: TEST PLANS

Sample 617-CT-36: Initial a/W = 0.389 ; Thickness B = 0.23 inch

Steps	Frequency (Hz)	Wave form	Hold time (s)	Kmax (ksi$\sqrt{inch}$)	R ratio	Environment	Step end (a/W)
1	2	Sine	-	35	0.5	Ultra-high purity argon (P(O2) = 10^{-22} atm)	0.4126
2	0.1	Sine	-	35	0.5		0.4284
3	0.01	Sine	-	40	0.63		0.4331
4	0.005	Sine	-	40	0.75		0.4362
5	0.002	Trap	500	45	0.88		0.4378
6	-	Cnst	-	45	1		0.5280

Sample 617-CT-22: Initial a/W = 0.3877; Thickness B = 0.23 inch

Steps	Frequency (Hz)	Wave form	Hold time (s)	Kmax (ksi$\sqrt{inch}$)	R ratio	Environment	Step end (a/W)
1	2	Sine	-	35	0.5	Ultra-high purity argon (P(O2) = 10^{-22} atm)	0.4126
2	0.1	Sine	-	35	0.5		0.4284
3	0.01	Sine	-	40	0.63		0.4331
4	0.005	Sine	-	40	0.75		0.4362
5	0.002	Trap	500	45	0.88		0.4378
6	-	Cnst	-	45	1		0.45
7	-	Cnst	-	45	1	10 ppm oxygen (P(O2) = 9 10^{-6} atm)	0.55

Sample 617-CT-35: Initial a/W = 0.4088 ; Thickness B = 0.23 inch

Steps	Frequency (Hz)	Wave form	Hold time (s)	Kmax (ksi$\sqrt{inch}$)	R ratio	Environment	Step end (a/W)
1	2	Sine	-	35	0.5	10 ppm oxygen ($P(O_2) = 9\ 10^{-6}$ atm)	0.4126
2	0.1	Sine	-	35	0.5		0.4284
3	0.01	Sine	-	40	0.63		0.4331
4	0.005	Sine	-	40	0.75		0.4362
5	0.002	Trap	500	45	0.88		0.4378
6	-	Cnst	-	45	1		0.4617
7	-	Cnst	-	45	1	Argon ($P(O_2) = 10^{-22}$ atm)	0.5105
8	-	Cnst	-	45	1	50 ppm oxygen ($P(O_2) = 4\ 10^{-5}$ atm)	0.5502

Sample 908: Initial a/W = 0.4249 ; Thickness B = 0.23 inch

Steps	Frequency (Hz)	Wave form	Hold time (s)	Kmax (ksi$\sqrt{inch}$)	R ratio	Environment	Step end (a/W)
1	2	Sine	-	35	0.5	10 ppm oxygen ($P(O_2) = 4\ 10^{-5}$ atm)	0.4485
2	0.1	Sine	-	35	0.5		0.4643
3	0.01	Sine	-	40	0.63		0.4690
4	0.005	Sine	-	40	0.75		0.4721
5	0.002	Trap	500	45	0.88		0.4737
6	-	Cnst	-	45	1		0.4832

7	-	Cnst	-	45	1	Argon (P(O2) = 2 10^{-21} atm)	0.4842
8	-	Cnst	-	45	1	50 ppm oxygen (P(O2) = 8 10^{-4} atm)	0.4922

Sample 617-CT-29: Initial a/W = 0.3871 ; Thickness B = 0.23 inch

Steps	Frequency (Hz)	Wave form	Hold time (s)	Kmax (ksi$\sqrt{inch}$)	R ratio	Environment	Step end (a/W)
1	2	Sine	-	25	0.5	1000 ppm oxygen (P(O2) = 9 10^{-4}atm)	0.4107
2	0.1	Sine	-	25	0.5		0.4265
3	0.01	Sine	-	30	0.63		0.4312
4	0.005	Sine	-	30	0.75		0.4343
5	0.002	Trap	500	35	0.88		0.4359
6	-	Cnst	-	35	1		0.4420
7	-	Cnst	-	35	1	Ultra-high purity argon (P(O2) = 2 10^{-21} atm)	0.4594

Sample 230-CT-01: Initial a/W = 0.3909 ; Thickness B = 0.225 inch

Steps	Frequency (Hz)	Wave form	Hold time (s)	Kmax (ksi$\sqrt{inch}$)	R ratio	Environment	Step end (a/W)
1	2	Sine	-	35	0.5	50 ppm oxygen (P(O2) = atm)	0.4224
2	0.1	Sine	-	35	0.5		0.4381
3	0.01	Sine	-	40	0.63		0.4429
4	0.005	Sine	-	40	0.75		0.4460
5	0.002	Trap	500	45	0.88		0.4476
6	-	Cnst	-	45	1		0.4718
7	-	Cnst	-	45	1	Ultra-high purity argon (P(O2) = 10^{-22} atm)	0.49

APENDIX B: DCPD CRACK GROWTH MEASUREMENTS

The following information regarding the DCPD measurement technique utilized in this research was exchanged between Peter L. Andresen (GE Global Research Center) and Pete Stahle (MIT). The personal communication briefly describes how the closed form DCPD equations were developed and additionally specifies the procedure for specimen setup to correctly employ the closed form fit. The following table presents the finite element calculations used to calculate the curve fit equation.

GE Crack Growth DCPD Method

Pete,

Here is the closed form fit I've worked out. We're actually not using these, but it's from sloth.
They are *very, very, very* close to the polynomials we use, whose disadvantage is that you can effectively not compute a closed form reversed solution for a polynomial (there are web sites that will do this, but the resulting solution takes about 5 sq. miles of paper to print out for a 5th order poly).

This should be self-explanatory. In my software (and my head), I keep two independent "potential scales" -- one is the real data, one is the conceptual (fitted) data. So when I start a test, I use the reverse fit to calc a (conceptual) potential from a known (as-machined) crack length. In turn, at the start of the test, I equilibrate the chemistry and load (typically ~80% of test load) and measure initial dcpd values. Both are "initial potentials" and I scale them proportionately. So if the measured dcpd goes up the 1%, I calculate 1.01 * the "conceptual potential", then enter that new value into the normal fit (potential >> a/W). I suspect you know this stuff.

The fits use current probes placed at the center of the top and bottom, 9.5 mm from the back face.

PL Andresen Closed Form dcpd Equations

FE Calculations:

a/W-calculated	a/W-data	Potential-data	Potential-calculated
0.3000	0.3	0.82888	0.824109
0.3250	0.325	0.87615	0.879987
0.3500	0.35	0.93496	0.939963
0.3750	0.5	1	1.0048085
0.4000	0.4	1.0706	1.073613
0.4250	0.425	1.1467	1.148085
0.4500	0.45	1.2286	1.22826
0.4750	0.475	1.3165	1.314652
0.5000	0.5	1.4109	1.407834
0.5250	0.525	1.5124	1.508446
0.5500	0.55	1.6215	1.617204
0.5750	0.575	1.739	1.734911
0.6000	0.6	1.8658	1.862475
0.6250	0.625	2.0029	2.00092
0.6500	0.65	2.1515	2.15141
0.6750	0.675	2.3133	2.315272
0.7000	0.7	2.4899	2.494025
0.7250	0.725	2.6839	2.689417
0.7500	0.75	2.8982	2.903407
0.7750	0.775	3.1368	3.138535
0.8000	0.8	3.4051	3.397362

Effort to find curve fit equation with closed form:

Logistic model: $y = a/[1 + b \times \exp(-cx)]$ where x is a/W and y is the potential

Coefficient data: a = -10.7615 ; b = -29.15836 ; c = 2.43175

Standard error: 0.0041727

Correlation coefficient: 0.9999872

Reverse fit: $x = -\frac{1}{c} \times \ln\left[\frac{\frac{a}{y}-1}{b}\right]$

APPENDIX C: XRD DATA

1- Peak list for alloy 617

Position [°2Th.]	d-spacing [Å]	Height [cts]	Rel. Intensity [%]	Matched by
36.132470	2.48596	249.8521	0.68	-
40.136970	2.24669	274.3099	0.74	Mn_2Ti_4O
41.118210	2.19532	229.5106	0.62	-
42.762440	2.11464	643.2450	1.74	Mn_2Ti_4O
43.783450	2.06595	36901.1300	100	$Ti_{0.08}Cr_{0.17}Ni_{0.75}$
43.897890	2.06595	24377.6100	66	-
46.660860	1.94504	444.2623	1.20	Mn_2Ti_4O
47.602320	1.90874	282.8228	0.77	-
50.714950	1.79865	1447.4600	3.92	$Ti_{0.08}Cr_{0.17}Ni_{0.75}$
51.037190	1.78805	3494.8660	9.47	$Ti_{0.08}Cr_{0.17}Ni_{0.75}$

2- Peak list for alloy 230

Position [°2Th.]	d-spacing [Å]	Height [cts]	Rel. Intensity [%]	Matched by
14.077540	6.29126	149.3684	0.21	-
18.283500	4.85240	186.0437	0.26	Cr_2MnO_4
24.503050	3.63300	1230.4940	1.74	Cr_2O_3
29.971190	2.97900	427.3757	0.60	-
32.588200	2.74777	306.1337	0.43	Cr_2O_3
33.071700	2.70646	494.6908	0.70	-
33.625110	2.66537	563.4802	0.79	Cr_2O_3
35.232120	2.54529	603.1721	0.85	Cr_2MnO_4
35.579030	2.52335	778.4558	1.10	$Mn_{0.33}Fe_{0.67}O$
36.143970	2.48520	1388.2410	1.96	Cr_2O_3
40.120820	2.24756	797.7073	1.13	W
40.734500	2.21511	549.5380	0.78	-
41.394400	2.18131	448.6881	0.63	Cr_2O_3
42.661320	2.11942	1864.2260	2.63	Ni
43.374790	2.08619	903.1073	1.27	-
43.908040	2.06038	70903.7200	100.00	Cr_2MnO_4
44.033110	2.05992	36499.8600	51.48	Cr_2O_3
46.683940	1.94413	388.7277	0.55	-
47.386280	1.91694	273.4897	0.39	Cr_2O_3
50.177160	1.81666	296.6086	0.42	$Fe_{0.61}Co_{0.17}Ni_{5.96}Mo_{1.15}W_{0.18}$

51.128710	1.78506	23234.3000	32.77	Ni
51.279400	1.78460	12112.5300	17.08	-
54.690760	1.67692	326.1775	0.46	Cr_2O_3
60.005280	1.54048	123.9178	0.17	$Mn_{0.33}Fe_{0.67}O$
60.849670	1.52110	259.0886	0.37	-
63.429450	1.46531	210.3739	0.30	Cr_2O_3
65.021960	1.43322	375.3079	0.53	Cr_2O_3

3-Peak list for alloy 908

Position [°2Th.]	d-spacing [Å]	Height [cts]	Rel. Intensity [%]	Matched by
24.293710	3.66383	1959.6190	16.81	Fe_2O_3
30.425160	2.93801	548.0762	4.70	$NiFe_2O_4$
33.302270	2.69047	7356.0310	63.09	Fe_2O_3
35.773060	2.50803	7687.3820	65.93	Fe_2O_3
35.869850	2.50770	5282.2820	45.30	$NiFe_2O_4$
37.485290	2.39731	273.3169	2.34	$NiFe_2O_4$
40.998570	2.19962	1746.5500	14.98	Fe_2O_3
43.527580	2.07750	895.0703	7.68	Fe_2O_3
44.393960	2.03895	11659.8800	100.00	$Cr_{0.09}Ni_{0.91}$
49.597770	1.83652	3023.0290	25.93	Fe_2O_3
51.694450	1.76685	6992.5190	59.97	$Cr_{0.09}Ni_{0.91}$
54.204700	1.69080	3972.9920	34.07	Fe_2O_3
54.345960	1.69093	2306.5290	19.78	-
57.264080	1.60753	1501.5230	12.88	$NiFe_2O_4$
57.732060	1.59560	1224.3530	10.50	Fe_2O_3
62.558950	1.48359	2934.6920	25.17	Fe_2O_3
63.103470	1.47209	1546.0450	13.26	$NiFe_2O_4$
64.143540	1.45071	2289.2250	19.63	Fe_2O_3
64.342320	1.45030	1392.679000	11.94	-

REFERENCES

1. G.S Giggins and F.S Pettit, 1969, Trans. Metall. Soc. AIME 245, pp.2495

2. Wayne Z. Friend, 1980, "Corrosion of nickel and nickel-base alloys", John Wiley & Sons, chapter 11

3. D.V Ignatov and R.D Shamgunova, 1961, "Mechanisms of the Oxidation of Nickel and Chromium Alloys", NASA Translation TT F-59

4. H. Ackermann, G. Teneva-Kosseva, H. Kohne, K. Lucka, S. Richter and J. Mayer, 2008, "Oxide scale formation on Al containing Ni-Cr-based high temperature alloys during application as flame tube material in recirculation oil burners", Materials and Corrosion, 59, No.5

5. G.S Giggins and F.S Pettit, 1971, Journal of the Electrochemical Society 118, pp. 1782

6. H.J Christ, L. Berchtold and H.G Sockel, 1986, "Oxidation of Ni-Base Alloys in Atmospheres with Widely Varying Oxygen Partial Pressures", Oxidation of Metals, Vol. 26

7. Changheui Jang, Daejin Lee and Daejong Kim, 2008, "Oxidation behavior of an alloy 617 in very high-temperature air and helium environments", International Journal of Pressure Vessels and Piping 85, pp 368-377

8. Daejong Kim, Changheui Jang and Woo Seog Ryu, 2009, "Oxidation Characteristics and Oxide Layer Evolution of Alloy 617 and Haynes 230 at 900°C and 1100°C", Oxidation of Metals

9. N. Birks, G.H Meier and F.S Pettit, "Introduction to the High-Temperature Oxidation of Metals". 2nd edition, chapter 5

10. F. Rouillard, C. Cabet, K. Wolski and M. Pijolat, 2007, "Oxide Layer Formation and Stability on a Nickel-Base Alloy in Impure Helium at High Temperature", Oxidation of Metals, Vol. 68, pp 133-148

11. H.J Christ, U. Kunecke, K. Meyer and H.G Sockel, 1987, "High Temperature Corrosion of the Nickel-based Alloy Inconel 617 in Helium Containing Small Amounts of Impurities", Vol. 87, pp 161-168

12. C. Cabet, J. Chapovaloff, F. Rouillard, G. Girardin, D. Kaczorowski, K. Wolski, M. Pijolat, 2008, "High Temperature Reactivity of two chromium-containing alloys in impure helium", Journal of Nuclear Materials 375, pp. 173-184

13. J. Chapovaloff, D. Kaczorowski and G. Girardin, 2008, "Parameters governing the reduction of oxide layers on Inconel 617 in impure VHTR He atmosphere", Materials and Corrosion 59, No. 7

14. L.F Coffin, 1972, Proceedings of the International Conference on "Fatigue: chemistry, mechanics and microstructure", pp. 590-600, Houston TX, NACE

15. D.A. Woodford, H.D. Solomon, L.F. Coffin, 1976, "The Effect of Temperature and Environment on Low Cycle Fatigue of Two Superalloys", Proceedings of the Second International Conference on Mechanical Behavior of Materials, pp.89

16. R. Molins, G. Hochstetter, J.C. Chassaigne, 1997, "Oxidation Effects on the Fatigue Crack Growth Behavior of Alloy 718 at High Temperature", Acta Materiala 45, pp. 663-674

17. E. Andrieu, G. Hochstetter, R. Molins and A. Pineau, 1994, in "Superalloys 718, 625 and 706 and various derivatives", Edition E. A. Loria, pp. 619-631

18. R. Molins, 1995, Thesis Ecole des Mines de Paris

19. D.A. Woodford, 2006, "Review on gas phase embrittlement and time dependent cracking of nickel based superalloys", Materials Performance Analysis Inc.

20. K. Sadananda, 1987, "Environmental effects on high temperature crack growth", 10th International Congress on Metallic Corrosion, Madras India, pp. 2301-2317

21. J. Benz, 2009, "Effect of oxygen potential on high temperature crack growth in alloy 617", Master's thesis, MIT

22. S-S Hsu, 1993, "Time-Dependent Crack Growth in a Heat-Resistant Alloy Inconel 617", Journal of Nuclear Science and Technology 30, pp. 302-313

23. S. Floreen and R. Raj, 1983, "Flow and Fracture at Elevated Temperature", pp. 383-404, Warrendale, PA, ASM

24. J.A. Pfaendtner, C.J. McMahon, 2001, "Oxygen-Induced Intergranular Cracking of a Ni-Base Alloy at Elevated Temperatures – an Example of Dynamic Embrittlement", Acta Materiala 49, pp. 3369-3377

25. K. Sadananda and P. Shahinian, 1980, "The effect of Environment on the Creep Crack Growth Behavior of several Structural Alloys", Materials Science and Engineering 43, pp. 159-168

26. K. Sadananda and P. Shahinian, 1983, "Creep Crack Growth Behavior of Several Structural Alloys", Metallurgical and Materials Transactions A 14, pp. 1467-1480

27. C.J. McMahon and L.F. Coffin, 1970, "Mechanisms of Damage and Fracture in High Temperature, Low-Cycle Fatigue of Cast Nickel-Based Superalloys", Metallurgical Transactions 1, pp. 3443-3450

28. R.H. Bricknell and D.A. Woodford, 1981, "Grain Boundary Embrittlement of the Iron Base Superalloy IN903A", Metallurgical Transactions A 12, pp. 1673-1680

29. E. Andrieu, R. Molins, H. Ghonem, 1992, "Intergranular Crack Tip Oxidation Mechanism in a Nickel-Based Superalloy", Materials Science and Engineering A: Structural Materials: Properties, Microstructure and Processing A 154, pp. 21-28

30. R.P. Wei, C. Miller, Z. Huang, G.W. Simmons, D.G. Harlow, 2009, "Oxygen enhanced crack growth in nickel-based superalloys and materials damage prognosis", Engineering Fracture Mechanics 76, pp.715-727

31. R.H. Bricknell and D.A. Woodford, 1981, "The Embrittlement of Nickel following High Temperature Air Exposure", Metallurgical Transactions 12A, pp. 425-433

32. Ajit K. Roy, Muhammad H. Hasan, Joydeep Pal, 2009, "Creep deformation of alloys 617 and 276 at 750-950°C", Materials Science and Engineering A 520, pp. 184-188

33. S. Chomette, J-M. Gentzbittel, and B. Viguier, 2010, "Creep behavior of as received, aged and cold worked INCONEL 617 at 850°C and 950°C", Journal of Nuclear Materials 399, pp. 266-274

34. Schubert et al., 1984, "Creep behavior of candidate materials for nuclear process heat applications", Nuclear Technology, Vol. 66, pp. 227-240

35. S.K Sharma, G.D Ko, F.X Li, K.J Kang, 2008, "Oxidation and creep failure of alloy 617 foils at high temperature", 2008, Journal of Nuclear Materials 378, pp. 144-152

36. P.S Shankar and K. Natesan, 2007, "Effect of trace impurities in helium on the creep behavior of alloy 617 for very high temperature reactor applications", Journal of Nuclear Materials 366, pp. 28-36

37. Y. Hosoi and S. Abe, 1975, "The Effect of Helium Environment on the Creep Rupture Properties of Inconel 617 at 1000°C", Metall. Trans. 6A, pp. 1171

38. M.E Kassner and M-T. Perez-Prado, 2000, "Five-Power-Law Creep in Single Phase Metals and Alloys", Progress in Material Science 45, pp.1-102

39. B. Wildshire and R.W Evans, 1985, "Creep behavior of Crystalline Solids", Pineridge UK

40. K. Schneider et al., 1984, "Creep behavior of Materials for High Temperature", Nuclear Technology 66, pp. 289-295.

41. W. Osthoff et al., 1984, "Creep and Relaxation Behavior of Inconel 617", Nuclear Technology 66, pp. 296-307.

42. R.W. Swindeman and M.J. Swindeman, 2005, "A comparison of Creep Models for Nickel Base Alloys for Advanced Energy Systems, ECCC Creep Conference London.

43. W.L. Mankins, J.C. Hosier and T.H. Bassford, 1974, "Microstructure and phase stability of Inconel Alloy 617", Metallurgical Transactions, Vol. 5, pp. 2579-2590

44. S. Kihara, J.B. Newkirk, A. Ohtomo and Y. Saiga, 1980, "Morphological Changes of Carbides During Creep and their Effects on the Creep properties of Inconel 617 at 1000°C", Metallurgical Transactions, Vol. 11A, pp. 1019-1031

45. H. Kirchhofer, F. Schubert and H. Nickel, 1984, "Precipitation Behavior of Ni-Cr-22Fe-18Mo (HASTELLOY X) and Ni-Cr-2Co-12Mo (INCONEL 617) after Isothermal Aging", Nuclear Technology 66, pp. 139-148

46. M. Cabibbo et al., 2008, "Creep behavior of INCOLOY alloy 617", Journal of Materials Science 43, pp. 2912-2921

47. T. Lillo, J. Cole, M. Frary and S. Schlegel, 2009, "Influence of Grain Boundary Character on Creep Void Formation in Alloy 617", Metallurgical and Materials Transactions A, Vol. 40A, pp. 2803-2811

48. R.W Swindeman and W. Ren, 2005, "A review of Aging Effects in Alloy 617", ORNL, TN 37831

49. S. Kiharo, A. Ohtomo, Y. Saiga, J.B. Newkirk, 1980, "Morphological changes of carbides during creep and their effects on the creep properties of Inconel 617 at 1000°C", Metallurgical and Materials Transactions A, Vol. 11, pp. 1019-1031

50. R.J. Hugues, 1999, "Fatigue crack growth of Incoloy 908 at high temperature", Master's thesis, MIT

51. S.K. Min, 1995, "Effect of chemistry modifications on the oxygen-induced embrittlement of Incoloy alloy 908", PHD thesis, MIT

52. Martin M. Morra, 1995, "Stress accelerated Grain Boundary Oxidation of Incoloy alloy 908 in high temperature oxygeneous atmospheres", PhD thesis, MIT

53. A. Toshimitsu Yokobori, 1988, "The crack initiation and growth under high temperature creep, fatigue and creep multiplication", Engineering Fracture Mechanics, Vol.31, No.6, pp. 931-945

54. K. Sadamanda and P.Shahinian, 1978, "Creep crack growth in Udimet 700", Metallurgical Transacions A, volume 9A.

55. N.Y. Nazmy and C. Wüthrich, 1983, "Creep crack growth in IN738 and IN939 nickel-base superalloys", Materials Science and Engineering, Vol. 61, Issue 2, pp. 119-125

56. V.V. Pokrovskii, V.N. Ezhov and V.G. Sidyachenko, 2001, "Special features of creep crack propagation in refractory nickel alloys under static loading", Strength of Materials, Vol. 33, No. 5

57. A. Saxena, 1997, "Nonlinear Fracture Mechanics for Engineers", CRR Press

58. A. Lo Conte, 2003, "Creep fracture and creep crack growth in Inconel 718 Nickel based Superalloy", Transactions of the 17th International Conference on Structural Mechanics in Reactor Technology.

59. A. Saxena, 1991, "Creep crack growth in high temperature ductile materials", Engineering Fracture Mechanics, Vol. 40, No.4/5, pp. 721-736

60. H.M. Yun, P.J. Ennis, H.Nickel and H. Schuster, 1984, "The effect of high temperature reactor primary circuit helium on the formation and propagation of surface cracks in alloy 800H and Inconel 617", Journal of nuclear Materials 125, pp. 258-272.

61. A.J. Perry, 1974, "Review – Cavitation in Creep", Journal of Materials Science 9, pp. 1016-1039

62. H. Riedel, 1986, "Fracture at High Temperatures", Materials research and Engineering, Edited by B. Ilschner and N.J. Grant

63. C.C. Law and M.J. Blackburn, 1979, "Creep-Rupture in Powder Metallurgical Nickel-base Superalloys at Intermediate Temperatures", Metallurgical and Materials Transactions A, pp. 495-507.

64. B.F. Dyson, 1982, "An analysis of carbon/oxygen gas bubble formation in some nickel alloys", Acta Metallurgica 30, Issue 8, pp. 1639-1646